UNIVERSITÀ
DEGLI STUDI
DI BRESCIA

DOTTORATO DI RICERCA IN INGEGNERIA DELL'INFORMAZIONE

settore scientifico disciplinare scienze fisiche per l'ingegneria

CICLO XXXV

PROPERTIES and GAS SENSING PERFORMANCES of LOW DIMENSIONAL METAL OXIDES NANOSTRUCTURES

NOME DEL DOTTORANDO

Wadumesthree Gayan Chathuranga Kumarage

NOME DEL SUPERVISORE

Prof.ssa. Elisabetta Comini

ANNO ACCADEMICO 2022/2023

PROPERTIES and GAS SENSING PERFORMANCES of LOW DIMENSIONAL METAL OXIDES NANOSTRUCTURES

W. G. C. KUMARAGE

Sensor Laboratory, Department of Information Engineering, Via Branze 38, 25123, University of Brescia, Brescia, Italy, 2023

Abstract - English

In the development of chemical sensors, sensitivity, selectivity, and stability (S_3) are the most crucial factors. Additionally, factors such as fast response time and low operating temperature are crucial for practical gas sensor design. In this context, cobalt oxide (Co_3O_4) nanostructures were fabricated on alumina (Al_2O_3) substrates to study the potential of improving the above mention gas sensing functionality of Co_3O_4.

The fabrication process of Co_3O_4/ZnO composite nanowires involves the in-situ thermal evaporation and oxidation at 800 °C in a vacuum environment with a pressure of 0.17 mbar and an airflow of 100 sccm Argon and 0.5 sccm oxygen. The Co_3O_4/ZnO composite nanowires produced feature a Pt tip, a Co_3O_4 layer, and a Co_3O_4/ZnO base with a Co_3O_4 root. These nanowires exhibit n-type semiconducting behavior, displaying a high response of 5530 ($\Delta G/G$) at 40% relative humidity (RH) when operating at 250 °C, to 50 ppm of acetone. This n-type behavior is attributed to the high concentration of ZnO in the composite. The sensors exhibit good repeatability, stability, and can detect acetone at sub-ppb levels, making them ideal for breath analysis with a detection limit of 500 ppb.

The prepared pristine Co_3O_4 nanowires (1-5 μm with 6-50 nm diameter) through thermal oxidation at 300 °C show excellent selectivity towards hydrogen when operating at 450 °C. The sensors exhibit abnormal n-type semiconducting behavior, due to the participation of lattice oxygen in the chemical sensing mechanism, as a result of the high operating temperature. The record low detection limit was 360 ppb. Furthermore, the sensors demonstrate excellent repeatability, stability, and resistance to humidity (90 RH%) gas sensing functionality due to their catalytic activity and high operating temperature.

Additionally, the study aims to explore the feasibility of reducing the preparation cost through the use of green synthesis to produce Co_3O_4 nanowalls. To accomplish this, Co_3O_4 nanowalls were prepared through thermal annealing at 280 °C on a hot plate. The resulting nanowalls

displayed good selectivity towards acetone when operating at 500 °C and this performance was further improved by 25.2-fold to 10 ppm acetone through Pt functionalization.

This study also investigates the synthesis of monoclinic TiO_2 nanobelts and Nb_2O_5 microcolumns through hydrothermal methods. The use of acetic acid as a protonating agent was found to effectively protonate TiO_2-(B) and produce TiO_2 gas sensors with impressive performance, reaching a response of 6.5 to 10 ppm of acetone at 150 °C. Nb_2O_5 microcolumns grown at 180 °C and calcined at 700 °C formed an orthorhombic crystal structure, which showed good selectivity in detecting ethanol with a detection limit of 1.4 ppb when operated at 500 °C in dry air. The sensors also maintained good performance in conditions of 90% humidity, only experiencing a 4% degradation in response compared to dry conditions (2.51, 10 ppm).

PROPRIETÀ E PRESTAZIONI DI SENSORI DI GAS BASATI SU NANOSTRUTTURE DI OSSIDI METALLICI DI DIMENSIONALITA' RIDOTTA

W.G.C. KUMARAGE

Sensor Laboratory, Dipartimento di Ingegneria dell'Informazione, Via Branze 38, 25123, Università degli Studi di Brescia, Brescia, Italia, 2023

Riassunto - Italiano

Nello sviluppo di sensori chimici, la sensibilità, la selettività e la stabilità (S3) sono i fattori più cruciali. Inoltre, fattori come il tempo di risposta rapido e la bassa temperatura di esercizio sono fondamentali per la progettazione del sensore di gas. Nanostrutture di ossido di cobalto (Co3O4) sono state fabbricate su substrati di allumina (Al_2O_3) per studiare il potenziale di miglioramento della suddetta funzionalità di rilevamento del gas del Co_3O_4.

Il processo di fabbricazione dei nanofili compositi Co_3O_4/ZnO prevede l'evaporazione termica in situ e l'ossidazione a 800 °C in un ambiente con una pressione di 0,17 mbar e un flusso di 100 sccm di argon e 0,5 sccm di ossigeno. I nanofili Co3O4/ZnO prodotti presentano una punta di Pt, uno strato di Co_3O_4 e una base di Co_3O_4/ZnO con la parte iniziale di Co_3O_4. Questi nanofili presentano un comportamento semiconduttore di tipo n, mostrano un'elevata risposta di 5530 (ΔG/G) a 50 ppm di acetone con il 40% di umidità relativa (RH) a 250 °C. Questo comportamento di tipo n è attribuito all'elevata concentrazione di ZnO nel composito. I sensori presentano una buona ripetibilità, stabilità e sono in grado di rilevare l'acetone a livelli inferiori a ppb, questo li rende ideali per l'analisi del respiro in cui è richiesto un limite di rilevamento di 500 ppb.

I nanofili Co_3O_4 invece sono stati preparati (1-5 μm con diametro 6-50 nm) attraverso l'ossidazione termica a 300 °C. Essi mostrano un'eccellente selettività verso l'idrogeno quando operano a 450 °C. I sensori presentano un comportamento semiconduttore anomalo di tipo n, a causa della partecipazione dell'ossigeno reticolare nel meccanismo di rilevamento a causa dell'elevata temperatura operativa. Il limite di rilevamento minimo è di 360 ppb. Inoltre, i sensori dimostrano un'eccellente ripetibilità, stabilità e funzionalità di rilevamento del gas all'umidità (90 RH%) grazie alla loro attività catalitica e all'elevata temperatura di esercizio.

Inoltre, questo studio mira a esplorare la fattibilità della riduzione dei costi di preparazione attraverso l'uso della sintesi verde per produrre nanowall di Co_3O_4. Questi nanowall di Co_3O_4 sono stati preparati mediante trattamento termico a 280 °C su una piastra riscaldante. I nanowall

risultanti hanno mostrato una buona selettività nei confronti dell'acetone quando si opera a 500 °C e le prestazioni sono state ulteriormente migliorate di 25,2 volte verso 10 ppm di acetone attraverso la funzionalizzazione del Pt.

Questo studio indaga anche la sintesi di nanocinture di TiO_2 monoclino e microcolonne di Nb_2O_5 attraverso metodi idrotermali. È stato scoperto che l'uso dell'acido acetico come agente protonante protona efficacemente TiO_2-(B) e produce sensori di gas TiO_2 con una risposta di 6,5 a 10 ppm di acetone a 150 °C. Le microcolonne Nb2O5 cresciute a 180 °C e calcinate a 700 °C hanno formato una struttura cristallina ortorombica, che ha mostrato una buona selettività nel rilevare l'etanolo con un limite di rilevamento di 1,4 ppb se operata a 500 °C in aria secca. I sensori hanno anche mantenuto buone prestazioni in condizioni di umidità del 90%, registrando una riduzione del 4% in risposta rispetto alle condizioni in aria secca (2,51, 10 ppm).

Acknowledgments

This research dissertation could not have been possible without the support of many people who were supportive to me in many ways. First and foremost, I would like to express my special gratitude and appreciation to my thesis advisor, Prof. Elisabetta Comini. Without her insightful guidance and encouragement, this thesis would never have been accomplished. She has been always with me, giving me a lot of help with her cordial heart.

I appreciate Dr. Dario Zappa and Dr. Vardan Galstyan for their comments and suggestions for improving my thesis work. I am grateful to Dr. Mariana Stefan and Dr. Valentin-Adrian Maraloiu at Bucharest National Institute of Materials Physics for providing me with the HRTEM, TEM, EPR/ESR measurements and cooperating sensor research. Many individuals have provided valuable technical discussion and assistance, including Dr. Nvapreet Kaur, Dr. Mandeep Singh. Special thanks to, Nicola Poli and Matteo Borsi, the technical staff of the Sensor Lab.

I would like to thank Prof. Laura Eleonora Depero, Prof, Giovanni Legnani, Prof. Irene Fassi, and Dr. Fabiana Farro at UNIBS. Your guidance has significantly improved every tool which I have worked on (inside and outside the lab).

I also thank the other members of the Sensor Lab including Abderrahim, Giorgio, Hakimeh, Hadjer, Safia, Hicham and Marwa, for their friendship and collaboration. They made my life at Sensor lab enjoyable.

Most of all, I would like to specially thank my family for their endless support. My parents are always giving me courage with their love. Next, I am expressing my gratitude to my brother. I extend my thanks to my wife, Buddhi, and my beloved baby boy, Thenuja. Without them, this thesis would never have come to fruition.

This work was supported by MIUR “Smart Cities and Communities and social innovation” project titled "SWaRM Net/Smart Water Resource Management – Networks”, NATO Science for Peace and Security Programmer (SPS) under grant G5634 AMOXES - "Advanced Electro-Optical Chemical Sensors".

Wadumesthree Gayan Chathuranga Kumarage

Biographical Note

Education

2023 – Ph.D., Physics for Engineering, University of Brescia, Brescia, Italy

Thesis title: Properties and gas sensing performances of low dimensional metal oxides nanostructures

2018 – Ph.D., Board of Physics, University of Peradeniya, Peradeniya, Sri Lanka

Thesis title: Studies on Modified Chemical Bath Deposited CdS Thin Films as a Solar Cell Window Material

2013 – M.S., Material Physics, University of Peradeniya, Peradeniya, Sri Lanka

Thesis title: Growth of CuO Thin Films for Possible PV Applications

2009 – B.S., Physical Sciences, University of Kelaniya, Kelaniya, Sri Lanka

2007 – Dip., Information Technology, University of Colombo, Colombo, Sri Lanka

Work Experiences

2019-2020: Postdoctoral Researcher, Sri Lanka Technological Campus, Padukka, Sri Lanka

2018-2019: Lecturer (Physics),Uva Wellassa University of Sri Lanka, Badulla, Sri Lanka

2016-2018: Scientific Assistant, University of Peradeniya, Peradeniya, Sri Lanka

2011-2017: Visiting Lecturer (Physics and Electronics), University of Kelaniya, Ragama, Sri Lanka

2013-2017: Visiting Teaching Assistant (Physics), Postgraduate Institute of Sri Lanka, Peradeniya, Sri Lanka

2012-2014: Teaching Assistant (Physics), University of Peradeniya, Peradeniya, Sri Lanka

2009-2012: Teaching Assistant (Physics), University of Kelaniya, Kelaniya, Sri Lanka

Publications Related to the Dissertation Work

Journal Articles Published

1. A. Moumen, W.G.C. Kumarage and E. Comini, *P-Type Metal Oxide Semiconductor Thin Films: Synthesis and Chemical Sensor Applications*, Sensors, 22(4), 2022, 1359.

2. V. Galstyan, A. Moumen, W.G.C. Kumarage and E. Comini, *Progress towards chemical gas sensors: Nanowires and 2D semiconductors*, Sensors and Actuators B: Chemical, 357, 2022, 131466.

3. W. G. C.Kumarage and E. Comini, *Low-Dimensional Nanostructures Based on Cobalt Oxide (Co_3O_4) in Chemical-Gas Sensing*, Chemosensors, 9(8), 2021,197.

Journal Articles Submitted

1. W. G. C. Kumarage, D. Zappa, V. A. Maraloiu, M. Stefan, E. Comini, *Green Synthesis of Co_3O_4 Nano Walls for Acetone Sensing*, Submitted Journal of Sensors and actuators-B.

2. W. G. C. Kumarage, V. A. Maraloiu, M. Stefan, E. Comini, *Co_3O_4 nanowire for hydrogen sensing*, Submitted Journal of Advanced Energy and Sustainability Research

3. S. A. Panamaldeniya, D. C. Maddumage, Milinda Kalutara Koralalage, D. C. Vithanage, K. M. M. D. Kimbulapitiya, W. G. C. Kumarage, E. Comini, B. S. Dassanayake, Nanda Gunawardhana, *Enhancing the electrochemical properties of Nb_2O_5 microwires /reduced graphene oxide composite in Lithium-ion battery anode*, Electrochimica Acta

4. W. G. C. Kumarage, S. Jayawadena, D. Zappa, M. Shimomura, N. Poli, E. Comini, *Novel design of Co_3O_4/ZnO nanowires for acetone sensing*, Submitted Journal of Sensors and actuators-B.

5. W. G. C. Kumarage, S. A. Panamaldeniya, D. C. Maddumage, A. Moumen, V. A. Maraloiu, C.G. Mihalcea, R.F. Negrea, B. S. Dassanayake, N. Poli, Gunawardhana, D. Zappa, V. Galstyan, E. Comini, *Synthesis of TiO_2-(B) Nanobelts for Acetone Sensing*, Submitted Journal of Applied Surfaces Sciences.

6. W. G. C. Kumarage, S. A. Panamaldeniya, H. Pakdel, D. C. Maddumage, B. S. Dassanayake, V. Galstyan, N. Gunawardhana, E. Comini, *Nb_2O_5 microwires for ethanol sensing*, Submitted Journal of Applied Surfaces Sciences.

7. Gayan W.C. Kumarage, Hadjer Hakkoum and Elisabetta Comini, *Recent Advancement on TiO_2 nanostructures: Sustainable synthesis and gas sensing*, Submitted Journal of Nanomaterials.

Books and Book Chapters

1. Gayan W.C. Kumarage and Elisabetta Comini, *Conductometric Gas Sensors*, Reference Module in Materials Science and Materials Engineering, Elsevier, 2022. doi.org/10.1016/B978-0-12-819728-8.00060-7

2. W. G. C. Kumarage and E. Comini, *Lodimensional 2D metal oxide: Synthesis and Gas sensors application*, 2024, Elsevier Metal Oxide Series, Series Editor; Ghenadii Korotcenkov, (under preparation)

Articles

1. W. G. C. Kumarage, *Nanostructures Based on Cobalt Oxide*, Nanoscience & Nanotechnology | Engineering, Chemical, https://encyclopedia.pub/13908

Abstracts

1. W. G. C. Kumarage, D. Zappa, V. A. Maraloiu, C.G. Mihalcea, M. Stefan, E. Comini, Surface functionalization of Co_3O_4 nanostructures, APS march meeting 2023, 20^{th} -22^{nd} March 2023, Lasvegas, Nevada, USA.

2. W. G. C. Kumarage, P. S. Jayawadena, D. Zappa, M. Shimomura, N. Poli, E. Comini, Synthesis and characterization of hybrid Co3O4/ZnO nanowires network gas sensing, TCM-TOEO 2022, 16^{th}-21^{st} October 2022, Crete, Greece.

3. Navpreet Kaur, Mandeep Singh, Gayan Chathuranga Kumarage Wadumesthree, Abderrahim Moumen, Hakimeh Pakdel, Dario Zappa, Vardan Galstyan, Elisabetta Comini, Metal Oxides Nanowires for Chemical Sensing and Solid Oxide Fuel Cell Applications, TCM-TOEO 2022, 16^{th}-21^{st} October 2022, Crete, Greece.

4. Elisabetta Comini, Navpreet Kaur, Mandeep Singh, Abderrahim Moumen, Giorgio Duina, Wadumasthree Kumarage, Dario Zappa, Vardan Galstyan, Metal Oxides and Composites for Chemical Sensing, Meet. Abstr. 2021, MA2021-01, 1450

5. W. G. C. Kumarage, G. Duina, A. Moumen, N. Poli, D. Zappa, and E. Comini, Thermal oxidized Co3O4 nanostructures for gas sensing, Advanced materials for sensing technologies, New Times-new trends in material science and engineering, 1st international virtual conference, 14^{th}-18^{th}, June 2021, pp46.

6. S. A. Panamaldeniya, D. C. Maddumage, R. D. L. Sandaruwan, H. M. M. Munasinghe Arachchige, W. G. C. Kumarage, B. S. Dassanayake and N. Gunawardhana, Nano-structured TiO_2-B for lithium-ion battery applications, PGIS Congress, 29^{th} – 31^{st} October 2021, Sri Lanka, 223 pp 171

TABLE OF CONTENTS

LIST OF FIGURES

LIST OF TABLES

CHAPTER I

Introduction

1.0 Background

A long and healthy life is the desire of every living being. While aging cannot be completely prevented, it can be mitigated to some extent through living in healthy environments and consuming quality foods. Unfortunately, both indoor and outdoor environments are increasingly being contaminated. Outdoor pollution is caused by natural events like windblown dust and volcano eruptions as well as human activities such as burning fossil fuels and industrial emissions. One of the major concerns is air pollution from harmful substances like sulfur oxides (SO_2), nitrogen oxides (NOX), carbon monoxide (CO), ammonia (NH_3), methane (CH_4), and volatile organic compounds (VOCs). Thus, monitoring and controlling toxic air pollution is crucial for society's and the environment's safety.

Air pollution poses a serious threat to human health and the environment. When primary pollutants mix with the atmosphere, they can transform into even more dangerous secondary pollutants, such as ozone (O_3) and nitrogen and sulfur compounds, which can cause harm to ecosystems and the environment [1]. While some of these pollutants are removed by natural processes like dry or wet deposition, many remain in the atmosphere and contribute to air pollution. The indoor environment is also polluted by a variety of sources, including VOCs, perfumes, hairsprays, cleaning products, paint, tobacco smoke, and more. This exposure can lead to a variety of health problems, including headaches, respiratory infections, heart disease, lung cancer, and more. In 2012, approximately 8% of global deaths were attributed to air pollution, and this number rose to 12% in 2019 [2]. Monitoring toxic and exhaust gases is crucial for ensuring society's and the environment's safety.

The demand for sensors with the ability to detect environmental pollutants, such as volatile/semi-volatile organic compounds (VOCs/SVOCs), harmful gases, particles, and chemicals, continues to grow. These sensors must possess high sensitivity, selectivity, stability, reliability, low power consumption, durability, affordability, and ease of use to be considered as effective sensors for real-world applications. As a result, numerous sensors have become an integral part of daily life, monitoring various environmental and human body parameters, with CHEMICAL GAS SENSORS being among the most versatile in detecting a wide range of toxic gases and VOCs.

Chemical sensors typically consist of metal oxides (MOXs) that are divided into two categories: n-type and p-type. N-type MOXs, such as ZnO, SnO_2, In_2O_3, TiO_2, Fe_3O_2, WO_3 are usually semiconductors with electrons as the majority carriers. While NiO, Co_3O_4, Cr_2O_3, Mn_3O_4, CuO have holes as the majority carriers [3,4]. Although p-type MOX gas sensors are less researched compared to n-type, they have potential advantages, such as high catalytic activity, which allows for low operating temperatures in gas sensors [5]. On the other hand, n-type MOXs have high electron density, resulting in a higher conductance.

The development of MOX nanostructures is a rapidly growing research area in the field of chemical sensors. This is due to the benefits of higher surface-to-volume ratios, increased stability, and larger active areas, which enhance gas sensing functionality, as evidenced by various studies [5-8]. Additionally, techniques such as noble metal functionalization [9,10] compositing [11,12], doping [13], and heterostructuring [14] can further improve the gas sensing abilities of chemical sensors.

This thesis aims to develop various MOX nanostructures and improve their gas sensing capabilities through composite formation and functionalization. The thesis begins by introducing chemical gas sensors, including their background, operating principle, and basic functionality test. The process of synthesizing MOXs and characterizing them is then described in the materials and methods section. In chapter 4, the gas sensing abilities of the prepared sensors and the results of physical characterization are thoroughly discussed. Finally, the main findings are summarized in the conclusion.

As the foundation of the thesis, the basic structure and material properties of the material under investigation are presented below.

1.1 Cobalt oxide (Co_3O_4)

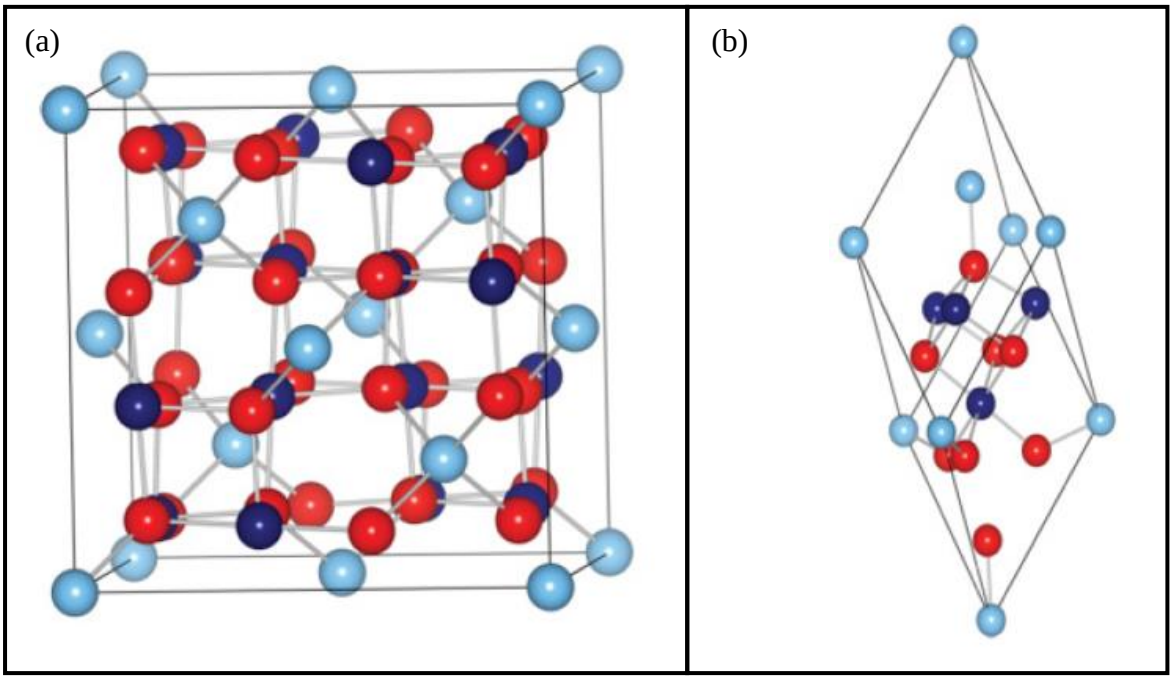

Figure 1.1. (a) Unit cell and (b) primitive cell (right) of Co_3O_4. Light cyan and navy-blue balls indicate Co^{2+} and Co^{3+} ions, red balls indicate O^{2-} ions [15].

The formula for the spinel structure is typically represented as $(A)[B_2]C_4$, where A and B are cations in tetrahedral and octahedral coordination, respectively, and C represents anions. For stability, A is typically divalent and B is trivalent, such as in the formula $(A^{2+})[B^{3+}]C_4$. The cobalt oxide (Co_3O_4) follows this structure as $(Co^{2+})[Co_2^{3+}]O_4$. The high spin Co^{2+} and low spin Co^{3+} occupy interstitial tetrahedral (8a) and octahedral (16d) sites in the close-packed face-centered cubic lattice of $CoO.Co_2O_3$. The material's p-type conductivity is due to Co vacancies in the crystal lattice and/or excess oxygen at interstitial sites. The band structure and the relevant spins are shown in Figure 1.2 (a,b) respectively. However, the charge carrier concentration can vary with operating temperature or doping. Also, the stability of the material under the different oxygen level is crucial for the gas sensing applications. In this case, among the supposed two ideal and six defect Co_3O_4 (1 1 0) surface models, the B surface with octahedral cobalt cations vacancy is easiest to form in an O-rich atmosphere and the A-terminated surface with the three-fold surface oxygen anion vacancy in an O-rich atmosphere. Among the Co_3O_4 (1 1 1) surfaces, the B′ surface terminated with the Co^{tet} cation is most stable (Figure 1.3) [16].

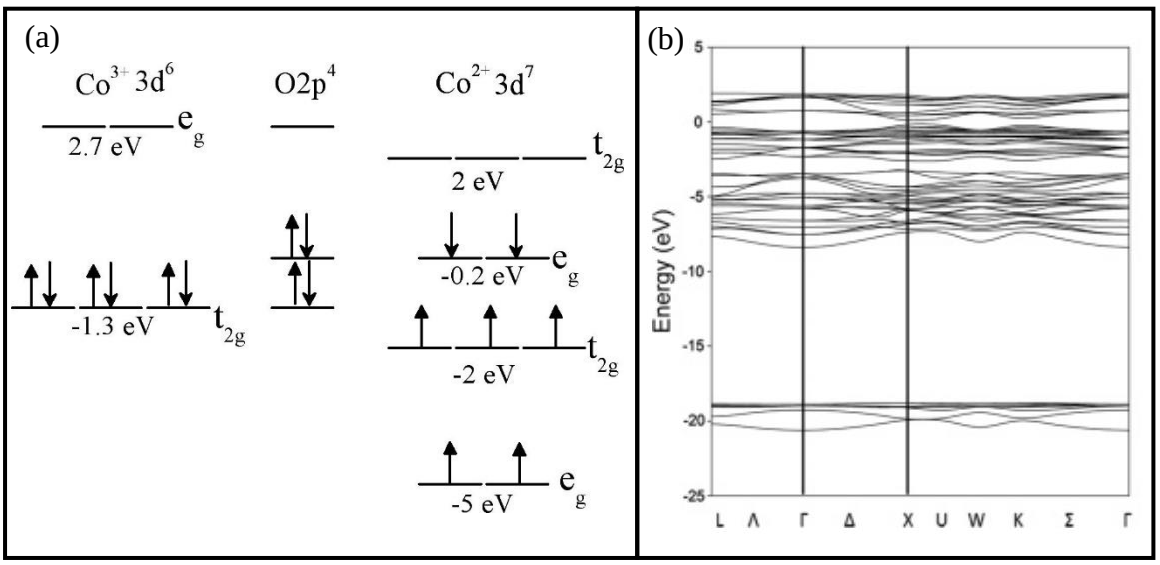

Figure 1.2. Schematic crystal field splitting and occupations of the Co 3d electrons in tetrahedral and octahedral environments. The relative energy of Co(3d) and O(2p) derived from density of states calculations are indicated, with reference to the valence band maximum at 0 eV [16], (b) band structure of Co_3O_4 obtained by PBE [15].

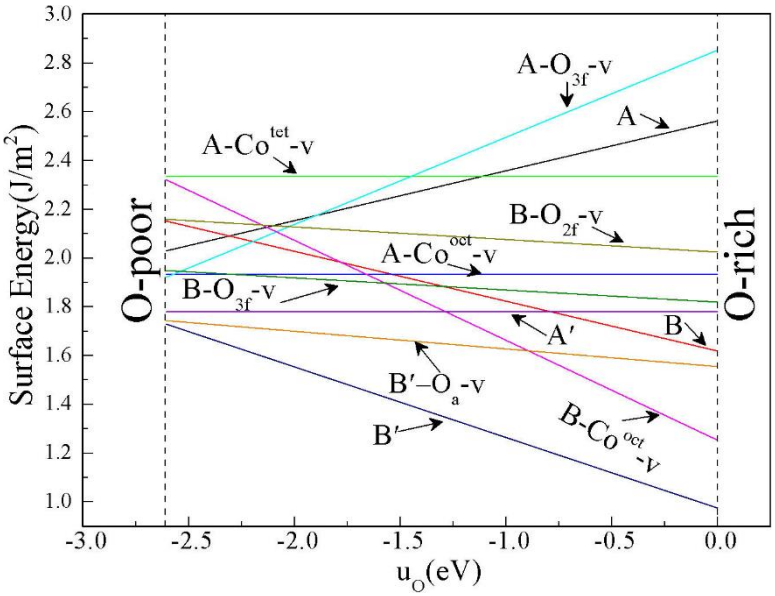

Figure 1.3. Surface energies of the Co_3O_4 (1 1 0) and Co_3O_4 (1 1 1) surfaces as a function of the oxygen chemical potential, μ_o, using μ_o^{gas} as zero reference. The dotted vertical lines mark the oxygen-poor and oxygen-rich limits for μ_o following the same approach as that of Reuter and Scheffler.

Consequently, studies on the gas sensing applications of Co_3O_4 have grown (Figure 1.4) due to its exceptional sensitivity, response/recovery, stability at high and low temperatures, superior electrical and chemical properties, and abundant availability. Accordingly, various nanostructures of Co_3O_4 have been studied for gas detection, such as nanoparticles [17,18], nanowires [19-21], nanorods [22,23], nanosheets [24,25], nanocubes [26], nanoneedles [27], hollow microspheres [28,29], and urchin-like structures [30,31].

However, mass production, stability, and manufacturing cost are key challenges in reported Co_3O_4 studies. This work aims to address these issues by exploring low-cost, green synthesis of Co_3O_4 nanowires and stable composite nanowires to improve gas sensing functionality and the scalability of Co_3O_4-based gas sensor manufacturing.

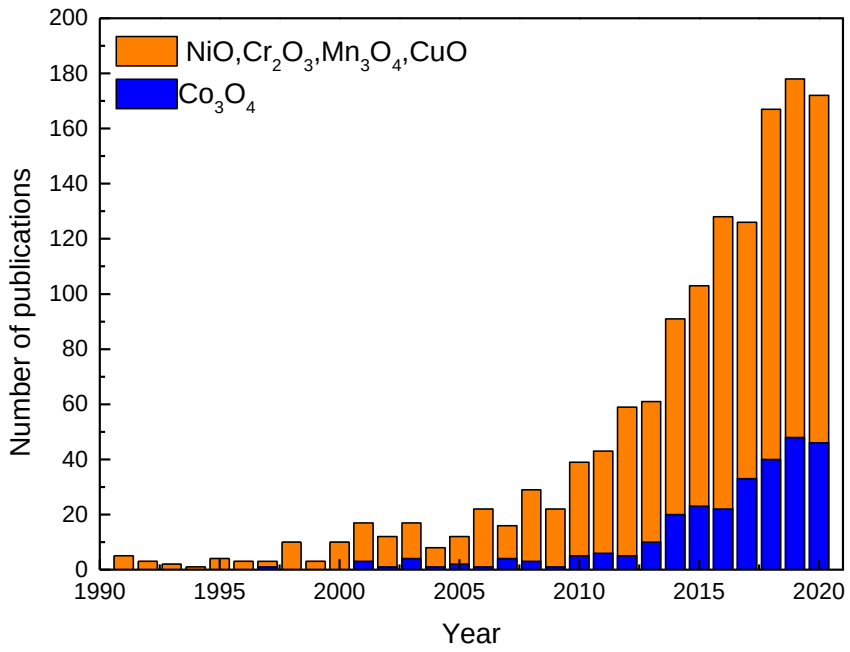

Figure 1.4. The advancement of p-type MOX gas sensors by yearly [5].

1.2 Titanium dioxide (TiO_2)

TiO_2 is a desirable transition-metal oxide for its biocompatibility, stability, abundance, and cost-effective production [32,33]. Figure 1.5 shows its crystallite phases, including anatase, rutile and brookite [34]. The building blocks of TiO_2 are chains of TiO_6 octahedra that form tetragonal lattice structures. The anatase structure has zigzag chains of octahedra linked by four edge-shared bonds (faces sharing, Figure 1.5(a)), while the rutile phase has linear chains of

octahedra at each corner, linked by two opposite edges of each octahedron (Figure 1.5(b)). Rutile is the most stable crystal structure in bulk materials, but brookite structures (Figure 1.5(c)) can also occur depending on growth techniques and mechanisms [35].

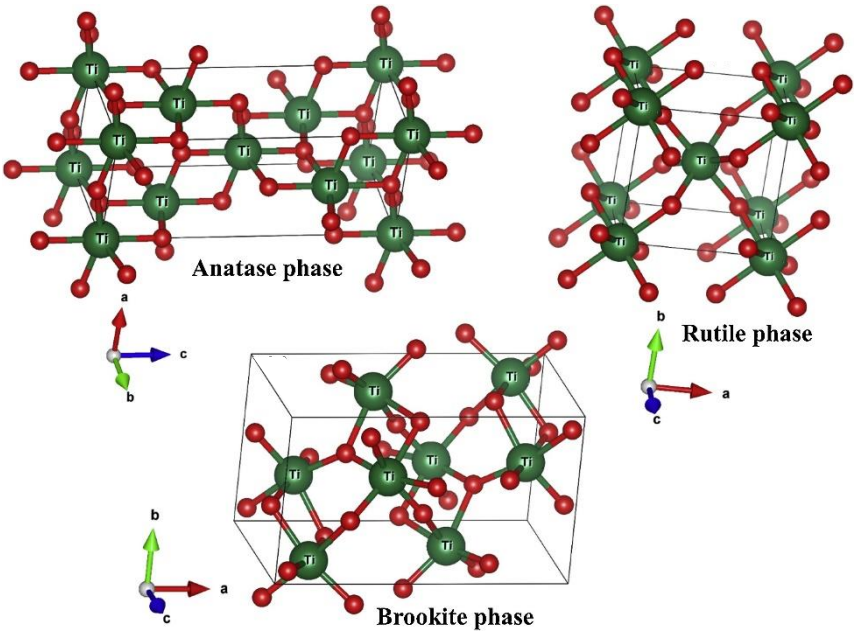

Figure 1.5. Crystal structure of anatase, rutile, and brookite phase of TiO_2.

In addition to the three crystal phases, there is another crystal phase called TiO_2-(B) (monoclinic, Figure 1.6). TiO_2-(B) has a layer structure that leads to low density, high specific capacity, and more open frameworks compared to other phases [36,37]. Despite its potential, the monoclinic TiO_2 is rarely seen in literature due to synthesis difficulties. The pioneering work on TiO_2-(B) was reported in 1980 by Marchand et al. [38]. Since then, numerous research works have been published on TiO_2-(B) showing its high catalytic and electrochemical properties [39,40].

Today there many growth techniques, such as atomic layer deposition [41], electrochemical anodization [42], hydrothermal method [43], chemical vapor deposition (CVD) [44], and electrospinning [45], have been used to produce low-dimensional TiO_2 structures for gas sensing applications [32]. This work focuses on utilizing the straightforward hydrothermal method to grow TiO_2 nanostructures for chemical gas sensing and investigating the possibility of using acetic acid instead of HCl in the protonation process.

1.3 Niobium oxide (Nb_2O_5)

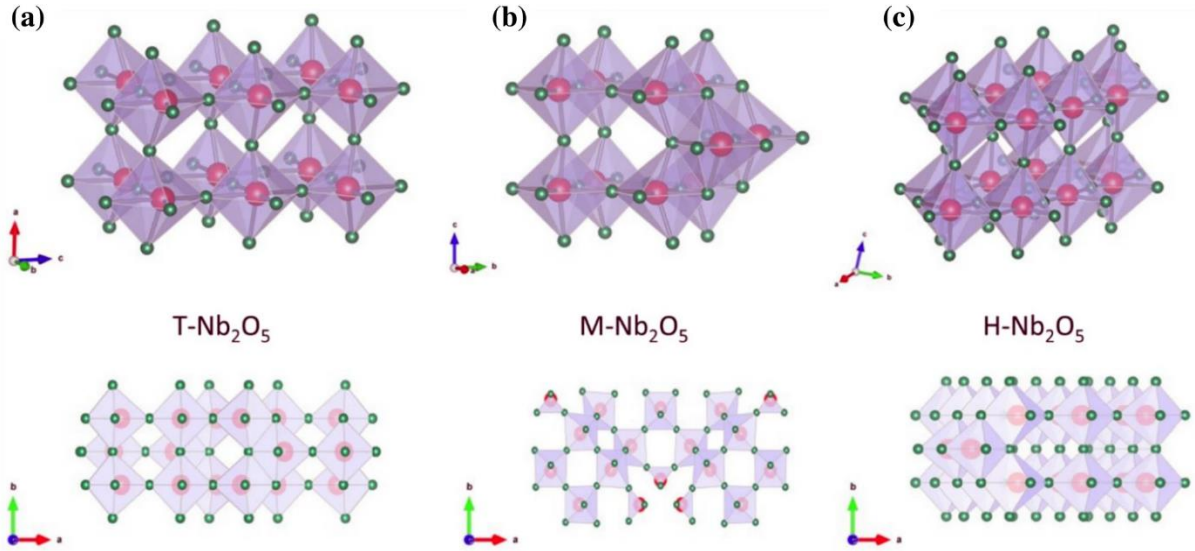

Figure 1.6. The crystal phase diagrams of (a) orthorhombic (T-Nb_2O_5), (b) tetragonal (M-Nb_2O_5), (c) monoclinic (H-Nb_2O_5) and the corresponding crystallographic plan views along the *c*-axis. The red and green balls represent Nb atoms and O atoms, respectively.

Nb_2O_5, known as Nobia, is a MOX that has gained significant attention due to its various crucial properties that make it ideal for a wide range of applications [46-48]. These properties include its strong surface acidity and water tolerance in acid-catalyzed reactions. There is an increasing interest in niobium-containing materials for chemical gas sensing [49-51]. Nb_2O_5 has several polymorphic forms, including amorphous (a- Nb_2O_5), orthorhombic (T-Nb_2O_5), tetragonal (M-Nb_2O5), and monoclinic (M-Nb_2O_5) (Figure 1.6), which are formed by distorted NbO_6 octahedra. The extent of distortion depends on the connections of edges and corners and is influenced by the preparation temperature (Figure 1.7).

Both B-Nb_2O_5 and T-Nb_2O_5 both show comparable band structures, including conduction and valence bands, as depicted in Figure 1.8. The Nb atoms play the biggest role in the conduction band, specifically in the d orbitals. Furthermore, the T-Nb_2O_5 phase has a higher density of d-orbital states than the B-Nb_2O_5 phase. Systems with d and f orbitals are recognized for possessing strong electron correlations. [52].

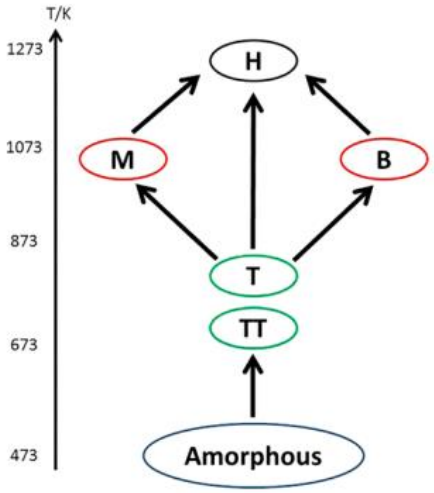

Figure 1.7. Phase Transition of Nb_2O_5 as a Function of Temperature [52].

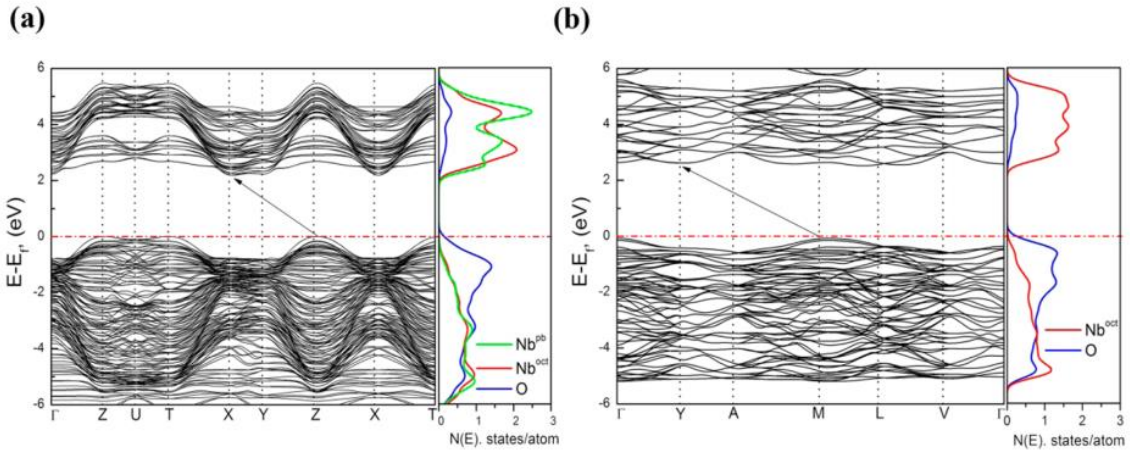

Figure 1.8. Band structure and projected DOS calculated with GGA for T-Nb_2O_5 (a) and B-Nb_2O_5 (b) phases [52].

References

[1] Hopke, Philip K., Qili Dai, Linxuan Li, and Yinchang Feng. "Global Review of Recent Source Apportionments for Airborne Particulate Matter." Science of The Total Environment 740 (2020): 140091. https://doi.org/10.1016/j.scitotenv.2020.140091.

[2] "State of Global Air." Home | State of Global Air. Accessed March 14, 2023. https://www.stateofglobalair.org/.

[3] Patil, Dewyani, Pradip Patil, Vijayanand Subramanian, Pattayil A. Joy, and Hari S. Potdar. "Highly Sensitive and Fast Responding CO Sensor Based on CO_3O_4 Nanorods." *Talanta* 81, no. 1-2 (2010): 37–43. https://doi.org/10.1016/j.talanta.2009.11.034.

[4] Kim, Hyo-Joong, and Jong-Heun Lee. "Highly Sensitive and Selective Gas Sensors Using P-Type Oxide Semiconductors: Overview." *Sensors and Actuators B: Chemical* 192 (2014): 607–27. https://doi.org/10.1016/j.snb.2013.11.005.

[5] Kumarage, Gayan W., and Elisabetta Comini. "Low-Dimensional Nanostructures Based on Cobalt Oxide (Co_3O_4) in Chemical-Gas Sensing." *Chemosensors* 9, no. 8 (2021): 197. https://doi.org/10.3390/chemosensors9080197.

[6] Galstyan, Vardan, Abderrahim Moumen, Gayan W.C. Kumarage, and Elisabetta Comini. "Progress towards Chemical Gas Sensors: Nanowires and 2D Semiconductors." Sensors and Actuators B: Chemical 357 (2022): 131466. https://doi.org/10.1016/j.snb.2022.131466.

[7] Comini, E., and D. Zappa. "One- and Two-Dimensional Metal Oxide Nanostructures for Chemical Sensing." Semiconductor Gas Sensors, 2020, 161–84. https://doi.org/10.1016/b978-0-08-102559-8.00005-7.

[8] Zappa, Dario, Vardan Galstyan, Navpreet Kaur, Hashitha M.M. Munasinghe Arachchige, Orhan Sisman, and Elisabetta Comini. "'Metal Oxide -Based Heterostructures for Gas Sensors'- A Review." Analytica Chimica Acta 1039 (2018): 1–23. https://doi.org/10.1016/j.aca.2018.09.020.

[9] Munasinghe Arachchige, Hashitha M.M., Dario Zappa, Nicola Poli, Nanda Gunawardhana, and Elisabetta Comini. "Gold Functionalized MOO3 Nano Flakes for Gas Sensing Applications." Sensors and Actuators B: Chemical 269 (2018): 331–39. https://doi.org/10.1016/j.snb.2018.04.124.

[10] Waclawik, Eric R, Jin Chang, Andrea Ponzoni, Isabella Concina, Dario Zappa, Elisabetta Comini, Nunzio Motta, Guido Faglia, and Giorgio Sberveglieri. "Functionalised Zinc Oxide Nanowire Gas Sensors: Enhanced NO_2 Gas Sensor Response by Chemical Modification of Nanowire Surfaces." Beilstein Journal of Nanotechnology 3 (2012): 368–77. https://doi.org/10.3762/bjnano.3.43.

[11] Galstyan, Vardan, Andrea Ponzoni, Iskandar Kholmanov, Marta M. Natile, Elisabetta Comini, Sherzod Nematov, and Giorgio Sberveglieri. "Reduced Graphene Oxide–TiO_2 Nanotube Composite: Comprehensive Study for Gas-Sensing Applications." ACS Applied Nano Materials 1, no. 12 (2018): 7098–7105. https://doi.org/10.1021/acsanm.8b01924.

[12] Kovalenko, V. V., M. N. Rumyantseva, A. M. Gaskov, E. V. Makshina, V. V. Yushchenko, I. I. Ivanova, A. Ponzoni, G. Faglia, and E. Comini. "SnO_2/FE_2O_3 Nanocomposites: Ethanol-Sensing Performance and Catalytic Activity for Oxidation of Ethanol." Inorganic Materials 42, no. 10 (2006): 1088–93. https://doi.org/10.1134/s0020168506100074.

[13] Epifani, Mauro, Teresa Andreu, Reza Zamani, Jordi Arbiol, Elisabetta Comini, Pietro Siciliano, Guido Faglia, and Joan R. Morante. "PT Doping Triggers Growth of TiO_2 Nanorods: Nanocomposite Synthesis and Gas-Sensing Properties." CrystEngComm 14, no. 11 (2012): 3882. https://doi.org/10.1039/c2ce06690d.

[14] Kaur, Navpreet, Dario Zappa, Matteo Ferroni, Nicola Poli, Marco Campanini, Raluca Negrea, and Elisabetta Comini. “Branch-like NIO/ZnO Heterostructures for VOC Sensing.” Sensors and Actuators B: Chemical 262 (2018): 477–85. https://doi.org/10.1016/j.snb.2018.02.042.
[15] Chen, Jia, Xifan Wu, and Annabella Selloni. “Electronic Structure and Bonding Properties of Cobalt Oxide in the Spinel Structure.” Physical Review B 83, no. 24 (2011). https://doi.org/10.1103/physrevb.83.245204.
[16] Xu, Xiang-Lan, Zhan-Hong Chen, Yi Li, Wen-Kai Chen, and Jun-Qian Li. “Bulk and Surface Properties of Spinel Co_3O_4 by Density Functional Calculations.” Surface Science 603, no. 4 (2009): 653–58. https://doi.org/10.1016/j.susc.2008.12.036.
[17] Xu, Keng, Xing Yu, Wei Zhao, and Wen Zeng. “Density-Dependent of Gas-Sensing Properties of Co_3O_4 Nanowire Arrays.” Physica E: Low-dimensional Systems and Nanostructures 118 (2020): 113956. https://doi.org/10.1016/j.physe.2020.113956.
[18] Kozlovskiy, A.L., and M.V. Zdorovets. “The Study of the Structural Characteristics and Catalytic Activity of $CO/CoCo_2O_4$ Nanowires.” Composites Part B: Engineering 191 (2020): 107968. https://doi.org/10.1016/j.compositesb.2020.107968.
[19] Nguyen, Hoa, and Sherif A. El-Safty. “Meso- and Macroporous Co_3O_4 Nanorods for Effective VOC Gas Sensors.” The Journal of Physical Chemistry C 115, no. 17 (2011): 8466–74. https://doi.org/10.1021/jp1116189.
[20] Wen, Zhen, Liping Zhu, Weimin Mei, Liang Hu, Yaguang Li, Luwei Sun, Hui Cai, and Zhizhen Ye. “Rhombus-Shaped Co_3O_4 Nanorod Arrays for High-Performance Gas Sensor.” Sensors and Actuators B: Chemical 186 (2013): 172–79. https://doi.org/10.1016/j.snb.2013.05.093.
[21] Wang, Shuangming, Jing Cao, Wen Cui, Longlong Fan, Xifei Li, Dejun Li, and Tong Zhang. “One-Dimensional Porous Co_3O_4 Rectangular Rods for Enhanced Acetone Gas Sensing Properties.” Sensors and Actuators B: Chemical 297 (2019): 126746. https://doi.org/10.1016/j.snb.2019.126746.
[22] Deng, Shaojuan, Xu Liu, Nan Chen, Dongyang Deng, Xuechun Xiao, and Yude Wang. “A Highly Sensitive VOC Gas Sensor Using P-Type Mesoporous Co_3O_4 Nanosheets Prepared by a Facile Chemical Coprecipitation Method.” Sensors and Actuators B: Chemical 233 (2016): 615–23. https://doi.org/10.1016/j.snb.2016.04.138.
[23] Zhang, Ziyue, Zhen Wen, Zhizhen Ye, and Liping Zhu. “Gas Sensors Based on Ultrathin Porous Co_3O_4 Nanosheets to Detect Acetone at Low Temperature.” RSC Advances 5, no. 74 (2015): 59976–82. https://doi.org/10.1039/c5ra08536e.
[24] Lü, Yinyun, Wenwen Zhan, Yue He, Yiting Wang, Xiangjian Kong, Qin Kuang, Zhaoxiong Xie, and Lansun Zheng. “Mof-Templated Synthesis of Porous Co_3O_4 Concave Nanocubes with High Specific Surface Area and Their Gas Sensing Properties.” ACS Applied Materials & Interfaces 6, no. 6 (2014): 4186–95. https://doi.org/10.1021/am405858v.
[25] Sun, Chao, Xintai Su, Feng Xiao, Chunge Niu, and Jide Wang. “Synthesis of Nearly Monodisperse Co_3O_4 Nanocubes via a Microwave-Assisted Solvothermal Process and Their Gas Sensing Properties.” Sensors and Actuators B: Chemical 157, no. 2 (2011): 681–85. https://doi.org/10.1016/j.snb.2011.05.039.
[26] Wen, Zhen, Liping Zhu, Yaguang Li, Ziyue Zhang, and Zhizhen Ye. “Mesoporous co3o4 Nanoneedle Arrays for High-Performance Gas Sensor.” Sensors and Actuators B: Chemical 203 (2014): 873–79. https://doi.org/10.1016/j.snb.2014.06.124.
[27] Park, Jinsoo, Xiaoping Shen, and Guoxiu Wang. “Solvothermal Synthesis and Gas-Sensing Performance of Co3o4 Hollow Nanospheres.” Sensors and Actuators B: Chemical 136, no. 2 (2009): 494–98. https://doi.org/10.1016/j.snb.2008.11.041.

[28] Shen, Shui Fa, Mei Li Xu, Dong Bao Lin, and Hai Bo Pan. “The Growth of Urchin-like Co_3O_4 Directly on Sensor Substrate and Its Gas Sensing Properties.” Applied Surface Science 396 (2017): 327–32. https://doi.org/10.1016/j.apsusc.2016.10.147.
[29] Li, Cheng Chao, Xiao Ming Yin, Tai Hong Wang, and Hua Chun Zeng. “Morphogenesis of Highly Uniform $CoCO_3$ Submicrometer Crystals and Their Conversion to Mesoporous Co_3O_4 for Gas-Sensing Applications.” Chemistry of Materials 21, no. 20 (2009): 4984–92. https://doi.org/10.1021/cm902126w.
[30] Lee, Jong-Heun. “Gas Sensors Using Hierarchical and Hollow Oxide Nanostructures: Overview.” Sensors and Actuators B: Chemical 140, no. 1 (2009): 319–36. https://doi.org/10.1016/j.snb.2009.04.026.
[31] Xu, Jiaqiang, Ding Wang, Lipeng Qin, Weijun Yu, and Qingyi Pan. “SNO_2 Nanorods and Hollow Spheres: Controlled Synthesis and Gas Sensing Properties.” Sensors and Actuators B: Chemical 137, no. 2 (2009): 490–95. https://doi.org/10.1016/j.snb.2009.01.011.
[32] Kaur, Navpreet, Mandeep Singh, Abderrahim Moumen, Giorgio Duina, and Elisabetta Comini. “1D Titanium Dioxide: Achievements in Chemical Sensing.” Materials 13, no. 13 (2020): 2974. https://doi.org/10.3390/ma13132974.
[33] Tian, Xu, Xiuxiu Cui, Tingrun Lai, Jie Ren, Zhichao Yang, Mingjing Xiao, Bingsen Wang, Xuechun Xiao, and Yude Wang. “Gas Sensors Based on TiO_2 Nanostructured Materials for the Detection of Hazardous Gases: A Review.” Nano Materials Science 3, no. 4 (2021): 390–403. https://doi.org/10.1016/j.nanoms.2021.05.011.
[34] Singh, Mrityunjay Kumar, and Mohan Singh Mehata. “Phase-Dependent Optical and Photocatalytic Performance of Synthesized Titanium Dioxide (TiO_2) Nanoparticles.” Optik 193 (2019): 163011. https://doi.org/10.1016/j.ijleo.2019.163011.
[35] Lin, Haifeng, Liping Li, Minglei Zhao, Xinsong Huang, Xiaomei Chen, Guangshe Li, and Richeng Yu. “Synthesis of High-Quality Brookite TiO^2 Single-Crystalline Nanosheets with Specific Facets Exposed: Tuning Catalysts from Inert to Highly Reactive.” Journal of the American Chemical Society 134, no. 20 (2012): 8328–31. https://doi.org/10.1021/ja3014049.
[36] Dai, Jun, Juan Yang, Xiaohan Wang, Lei Zhang, and Yingjie Li. “Enhanced Visible-Light Photocatalytic Activity for Selective Oxidation of Amines into Imines over TiO_2(b)/Anatase Mixed-Phase Nanowires.” Applied Surface Science 349 (2015): 343–52. https://doi.org/10.1016/j.apsusc.2015.04.232.
[37] Yang, Dongjiang, Hongwei Liu, Zhanfeng Zheng, Yong Yuan, Jin-cai Zhao, Eric R. Waclawik, Xuebin Ke, and Huaiyong Zhu. “An Efficient Photocatalyst Structure: TiO_2(B) Nanofibers with a Shell of Anatase Nanocrystals.” Journal of the American Chemical Society 131, no. 49 (2009): 17885–93. https://doi.org/10.1021/ja906774k.
[38] Marchand, René, Luc Brohan, and Michel Tournoux. “TiO_2(B) a New Form of Titanium Dioxide and the Potassium Octatitanate K2TI8O17.” Materials Research Bulletin 15, no. 8 (1980): 1129–33. https://doi.org/10.1016/0025-5408(80)90076-8.
[39] Zhou, Nan, Yufan Wu, Qing Zhou, Yiran Li, Shihan Liu, Hongbo Zhang, Zhi Zhou, and Mao Xia. “Enhanced Cycling Performance and Rate Capacity of SIO Anode Material by Compositing with Monoclinic TiO_2 (B).” Applied Surface Science 486 (2019): 292–302. https://doi.org/10.1016/j.apsusc.2019.05.025.
[40] Andreev, Yuri G., Pooja M. Panchmatia, Zheng Liu, Stephen C. Parker, M. Saiful Islam, and Peter G. Bruce. “The Shape of Tio2-b Nanoparticles.” Journal of the American Chemical Society 136, no. 17 (2014): 6306–12. https://doi.org/10.1021/ja412387c.
[41] Dvorak, Filip, Raul Zazpe, Milos Krbal, Hanna Sopha, Jan Prikryl, Siowwoon Ng, Ludek Hromadko, Filip Bures, and Jan M. Macak. “One-Dimensional Anodic TiO_2 Nanotubes

Coated by Atomic Layer Deposition: Towards Advanced Applications." Applied Materials Today 14 (2019): 1–20. https://doi.org/10.1016/j.apmt.2018.11.005.
[42] Galstyan, Vardan, Elisabetta Comini, Camilla Baratto, Andrea Ponzoni, Matteo Ferroni, Nicola Poli, Elza Bontempi, Mariangela Brisotto, Guido Faglia, and Giorgio Sberveglieri. "Large Surface Area Biphase Titania for Chemical Sensing." Sensors and Actuators B: Chemical 209 (2015): 1091–96. https://doi.org/10.1016/j.snb.2014.12.027.
[43] Bindra, Prateek, Hardik Mittal, Bibhas R. Sarkar, and Arnab Hazra. "Synthesis of Highly Ordered TiO_2 Nanorods on a Titanium Substrate Using an Optimized Hydrothermal Method." Journal of Electronic Materials 51, no. 4 (2022): 1707–16. https://doi.org/10.1007/s11664-022-09436-7.
[44] Alotaibi, Abdullah M., Sanjayan Sathasivam, Benjamin A. Williamson, Andreas Kafizas, Carlos Sotelo-Vazquez, Alaric Taylor, David O. Scanlon, and Ivan P. Parkin. "Chemical Vapor Deposition of Photocatalytically Active Pure Brookite Tio2 Thin Films." Chemistry of Materials 30, no. 4 (2018): 1353–61. https://doi.org/10.1021/acs.chemmater.7b04944.
[45] Otieno, Odhiambo Vincent, Edina Csáki, Orsolya Kéri, László Simon, István Endre Lukács, Katalin Mészáros Szécsényi, and Imre Miklós Szilágyi. "Synthesis of TiO_2 Nanofibers by Electrospinning Using Water-Soluble TI-Precursor." Journal of Thermal Analysis and Calorimetry 139, no. 1 (2019): 57–66. https://doi.org/10.1007/s10973-019-08398-z.
[46] Yao, David D., Rozina A. Rani, Anthony P. O'Mullane, Kourosh Kalantar-zadeh, and Jian Zhen Ou. "High Performance Electrochromic Devices Based on Anodized Nanoporous Nb_2O_5." The Journal of Physical Chemistry C 118, no. 1 (2013): 476–81. https://doi.org/10.1021/jp410097y.
[47] Raba, A. M., J. Barba-Ortega, and M. R. Joya. "The Effect of the Preparation Method of NB2O5 Oxide Influences the Performance of the Photocatalytic Activity." Applied Physics A 119, no. 3 (2015): 923–28. https://doi.org/10.1007/s00339-015-9041-3.
[48] Molina, Maria José, Manuel López Granados, Antonella Gervasini, and Paolo Carniti. "Exploitment of Niobium Oxide Effective Acidity for Xylose Dehydration to Furfural." Catalysis Today 254 (2015): 90–98. https://doi.org/10.1016/j.cattod.2015.01.018.
[49] Khatoon, Rabia, Sajid Rauf, Mahmood Ul Haq, Sanam Attique, Salah Ud Din, Nasir Ali, Yichuan Guo, Hongwen Chen, Yang Tian, and Jianguo Lu. "Design of Highly Sensitive and Selective Ethanol Sensor Based on α-FE2O3/Nb2O5 Heterostructure." Nanotechnology 32, no. 19 (2021): 195503. https://doi.org/10.1088/1361-6528/abdd5e.
[50] Mao, Li-Wen, Li-Yuan Zhu, Tao Tao Wu, Lei Xu, Xuan-Hong Jin, and Hong-Liang Lu. "Excellent Long-Term Stable H_2S Gas Sensor Based on Nb_2O_5/SnO_2 Core-Shell Heterostructure Nanorods." Applied Surface Science 602 (2022): 154339. https://doi.org/10.1016/j.apsusc.2022.154339.
[51] Rani, Rozina Abdul, Ahmad Sabirin Zoolfakar, Jian Zhen Ou, Matthew R. Field, Michael Austin, and Kourosh Kalantar-zadeh. "Nanoporous Nb_2O_5 Hydrogen Gas Sensor." Sensors and Actuators B: Chemical 176 (2013): 149–56. https://doi.org/10.1016/j.snb.2012.09.028.
[52] Pinto, Mirele B., Antonio Lenito Soares, Andy Mella Orellana, Hélio A. Duarte, and Heitor A. De Abreu. "Structural, Electronic, and Thermodynamic Properties of the T and B Phases of Niobia: First-Principle Calculations." The Journal of Physical Chemistry A 121, no. 12 (2017): 2399–2409. https://doi.org/10.1021/acs.jpca.6b11383.

CHAPTER II

Chemical sensors

2.1 State-art-chemical sensors

Chemical Sensor is a device that converts chemical information into a measurable signal [1]. A gas sensor device constitutes of three main systems (Figure 2.1); (1) a system for transporting the chemical/gas which performs sampling, filtering, and preconditioning; (2) a section for detecting the analyte (sensing element); (3) a system for computing which process data and convert them into a readable format [2]. Furthermore, chemical sensors involve in two main processes: reception and transducer operation. The reception operation is the interaction of the analyte with the MOX surface. This involves in three gas sensing processes: gas diffusion, the material/analyte interactions (surface/bulk reaction), and the transport of electrical parameters [3]. The interaction occurs at the material/analyte interface and the particular processes are an adsorption reaction, liquid-solid interactions or ion exchange. The absorption process is to be by either strong chemical bonding by charge exchange process (chemisorption) or weak van der Waals force (physisorption) between MOXs surface and gas analytes. Conductimetric chemical sensors are based on the fundamental working principle of this interaction and its effect on the sensor resistance.

The transducer process involves converting the chemical signal into an electronic one in conductometric sensors. In this case, the sensing element is integrated with electrodes that can be either two-/three-/four-probes or interdigital electrodes (IDEs) by sputtering, conductive paste coating, or thermal evaporation to build electrical devices. Usually, insulating substrates such as polycrystalline Si/SiO_2, Al_2O_3, glass, polymers, and sapphire are utilized in device fabrication. Furthermore, the electrical parameters of the sensing layer, for example, conductivity (σ), work function (ϕ), and permittivity (ε) are significantly altered by gaseous analytes in this process.

Data processing is the use of raw electrical signals (conductometric sensors) for alarm or detection. Usually, raw data are processed from simple filtering/amplifying to advanced statistical methods for example, Linear discriminant analysis (LDA) and artificial neural networks (ANN) techniques.

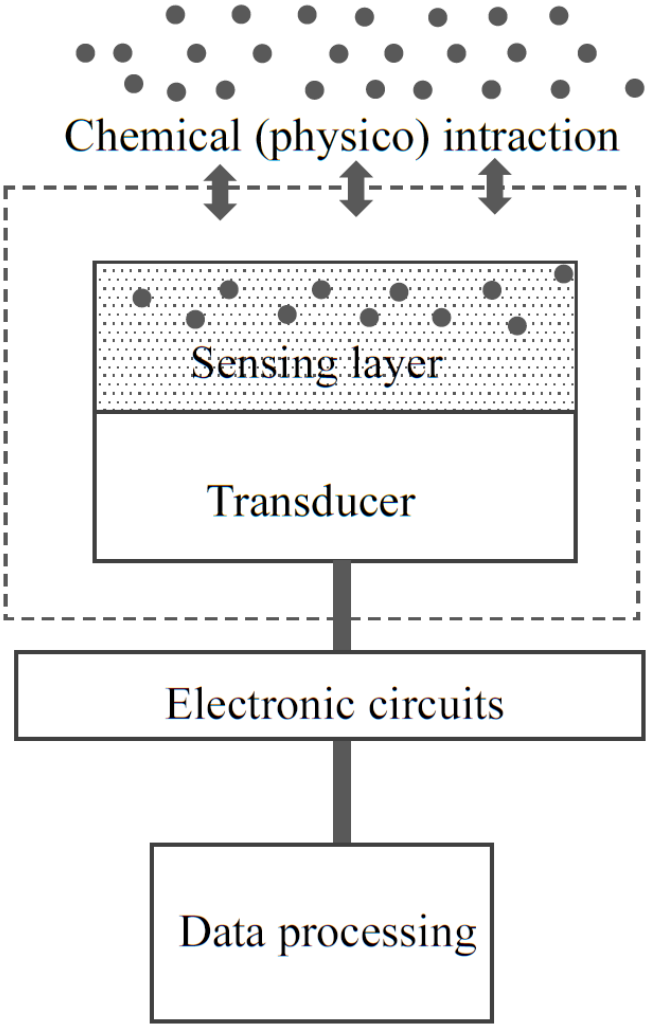

Figure 2.1. Illustration of parts of a chemical sensor.

It is difficult to make an exhaustive classification of all gas sensors that are currently available or in development. However, depending on the operation mode, the materials used and the detection mechanisms, we can distinguish between several main types that can be used in the field of gas detection according to the transduction mechanism. They can be electrical, mechanical, optical, thermal, calorimetric, or acoustic parameters. These parameters may be integrated into different types of gas sensors as classified in Figure 2.2. Besides, all of them have their own advantages and disadvantages as well as unique applications (Table 2.1) [4]. This dissertation work is focused on the second part of the sensor device which is the sensing layer that transforms the chemical interaction into an electrical signal in conductometric chemical sensors.

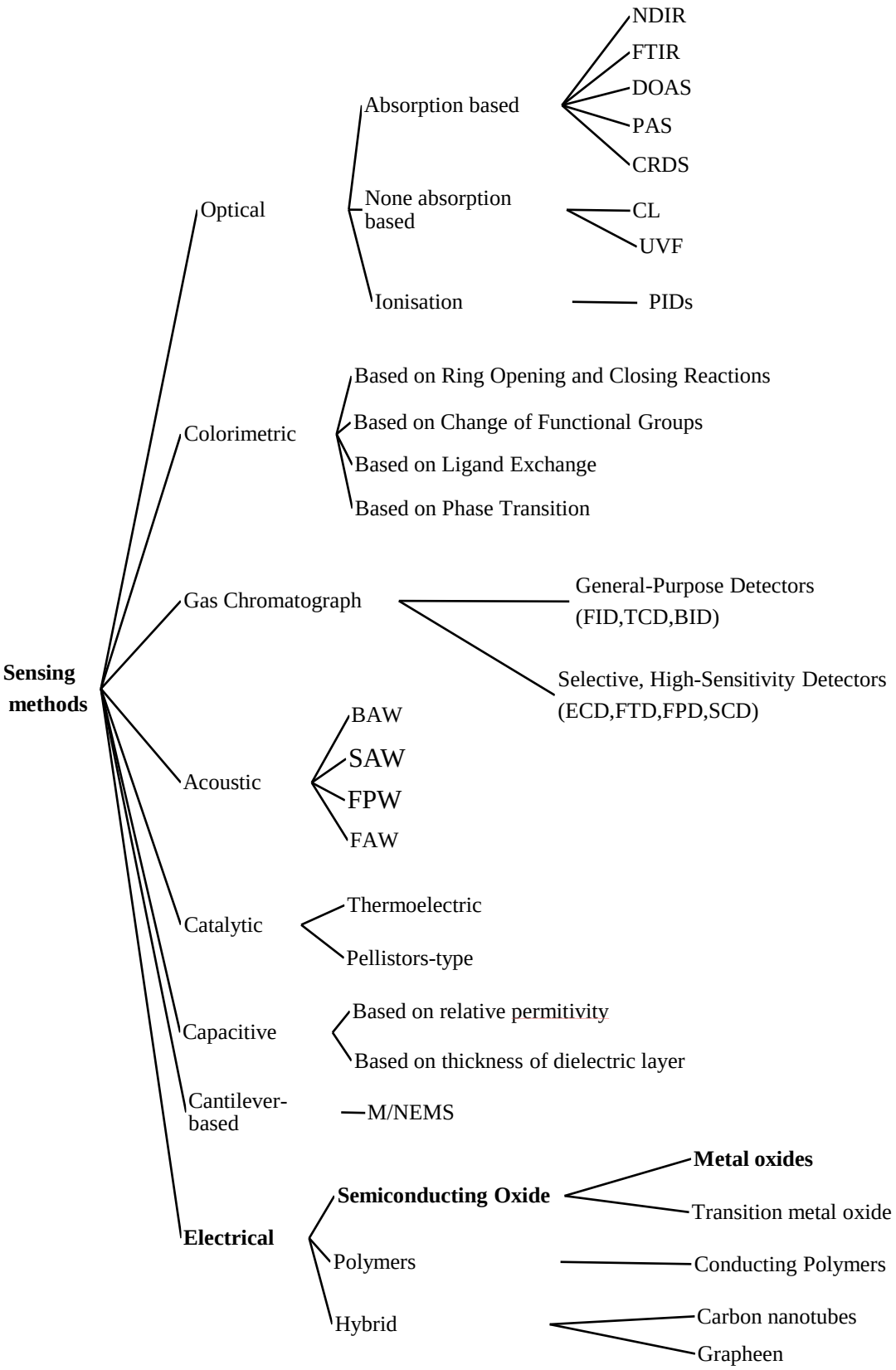

Figure 2.2. Classification of gas sensors based on sensing methods and types of gas sensors.

Table 2.1. Elementary gas sensing methods, advantages, disadvantage, and their application.

Methods	Advantages	Disadvantages	Application Fields
Electrical	(a) Low cost (b) Fast response time (c) High sensitivity (d) Low weight (e) Wide range of target gases	(a) Sensitive to environmental factors such as humidity (b) Energy consumption	(a) Industrial applications (b) Indoor air monitoring (c) Storage place of synthetic products such as paints, wax, or fuels
Optical	(a) High sensitivity, selectivity, and stability (b) Long lifetime (c) Insensitive to environmental change	(a) Difficulty in miniaturization (b) High cost	(a) Remote air quality monitoring (b) Gas leak detection systems with high accuracy and safety (c) High-end market applications
Infrared	(a) Highly selective and offer a wide range of sensitivities (b) The detector does not directly contact the gas (c) Corrosion resistance (d) Least amount of maintenance or replacement (e) Reliable design	(a) Perform poorly in extreme environments; high humidity, fog (b) Failure to detect hydrogen (c) Do not work well when multiple hydrocarbon-based gases	(a) Toxic and combustible gas monitoring (b) Industries, including the petrochemical industry

Calorimetric	(a) Stable at ambient temperature (b) Low limit of detection (c) Adequate sensitivity (d) Low power consumption	(a) Risk of catalyst poisoning and Explosion (b) Intrinsic deficiencies in selectivity	(a) Most combustible gases under industrial environment (b) Petrochemical plants (c) Mine tunnels (d) Kitchens
Gas Chromatograph	(a) Excellent separation Performance (b) High sensitivity and selectivity	(a) High cost (b) Difficulty in miniaturization for portable applications	Typical laboratory analysis
Catalytic	(a) Excellent Accuracy and reproducibility (b) Fast response (c) Low power consumption (d) Humidity independent response	(a) Catalytic poisoning (b) Sensor drift (c) Calibration	(a) Coal mines (b) Industrial sectors (c) Drunk driving detection
Acoustic	(a) Long lifetime (b) Avoiding secondary pollution (c) Detect nerve and blister agents	(a) Low sensitivity (b) Sensitive to environmental change (c) Difficulty in handling during the fabrication process	(a) Components of Wireless Sensor Networks (b) Electronic nose (c) Food quality testing
Cantilever	(a) Higher sensitivity (b) Fast response time (c) Low cost (d) Array format (e) Small overall dimensions	(a) Long-term stability (b) Poor performance in a viscous medium	Typical laboratory analysis such as health care, energy, security, artificial nose setup

2.2 Conductometric metal oxide chemical sensors

The pioneering work on employing semiconductors in chemical sensing has been reported by Brattain in the early 1950s [5]. This revolutionary idea was established on the study of a change in the electrical resistance of Ge when exposed to different environmental conditions. Accordingly, the first conductometry MOXs gas sensor was prepared in the 1960s in which ZnO thin film was employed to detect propane at the operating temperature of 485 °C (6). Today, many MOXs are known to demonstrate sensitivity to various gases [7-10]. Usually, below 500 °C, conductivity changes in MOXs for instance, TiO_2 and ZnO, are based on adsorption/desorption phenomena that alter the primary surface or grain boundary (only for porous polycrystalline materials) conductivity [11,12]. The surface reactions include adsorbed negatively charged oxygen species in the form of molecular (O_2^-) or atomic (O^-). However, at higher temperatures, above 900 ºC, this surface reaction is changed to bulk reactions. The bulk reactions occur between point defects in the oxides and oxygen (O_2) in the gas phase. Typically, most of the MOXs sensors are based on surface phenomena, allowing the ability to fit them to detect a broad range of gases.

2.3 Chemical gas sensing mechanism

2.3.1 Bulk conductivity

The modification in the stoichiometry of MOXs as a function of oxygen is well known. Besides, these changes in stoichiometry modify the electrical conductivity (σ) of the MOXs. Generally, this conductivity change is represented in equation 2.1 [11],

$$\sigma = \sigma_o \exp(-E_A/kT)\, p(O_2)^{1/n} \qquad (2.1)$$

k - Boltzmann's constant

T - temperature in degrees Kelvin

E_A - activation energy of bulk conduction, the energy required to form the ionic defects and their subsequent ionization by establishing charge carriers in the conduction or valence band.

$p(O_2)$ - partial pressure of the oxygen gas

n - depend on the nature of the point defects arising when oxygen is removed from the lattice

For example, TiO_2 oxygen sensor is operating at a low oxygen pressure environment and at a sufficient temperature to produce defects, the TiO_2 is supposed to reduce by forming Ti interstitials, $Ti^{\bullet\bullet\bullet\bullet}$, as in equation (2.2).

$$Ti_{Ti}^{x} + 2O_{O}^{x} \rightarrow Ti_{i}^{\bullet\bullet\bullet\bullet} + 4e + O_2(g) \quad (2.2)$$

with the charge neutrality,

$$4Ti_{i}^{\bullet\bullet\bullet\bullet} = n \quad (2.3)$$

The equilibrium constant of the reduction reaction (2.2) ,

$$K_R = [Ti_i^{\bullet\bullet\bullet\bullet}].n^4.p(O_2) \quad (2.4)$$

From equation (2.3) and (2.4),

$$n = 4.[Ti_i^{\bullet\bullet\bullet\bullet}] = (4\,K_R)^{1/5}.\,p(O_2)^{-1/5} \quad (2.5)$$

Accordingly, when the oxygen pressure becomes the order of n = -5, TiO_2 is reduced by formation of Ti interstitial defects.

2.3.2 Surface conductivity

The well-known clarification for surface conductivity is that negatively charged oxygen species play a crucial role in detecting analyte gases such as H_2 and CH_4. Once, oxygen is chemisorbed, onto the MOXs surface, charge carriers (electrons in n-type and holes in p-type MOXs) in the MOXs are extracted from the near surface region up to a certain depth of the MOXs. This process creates oxygen species: molecular O_2^-, atomic O^-, and O^{2-} at the temperature < 150 °C, 150 - 400 °C, and > 400 °C respectively, as shown in the equation (2.6) - (2.8), on the MOXs surface [3]. Among these, O^- is the most reactive species with reducing gases usually in the temperature range of 300-500 °C, in which most semiconductor gas sensors are operated. So, the response of the sensor is significantly dependent on the variation in surface coverage of O^-. Once, charge carrier is trapped (as in equating 2.6-2.8), an electron depletion region in an n-type (hole accumulating layer in p-type) will be formed. The built electron depleted layer

(or hole accumulating layer) acts as a potential barrier at the surface with a significant width and height.

$$O_{2(gas)} + e^{-} \rightarrow O_2^{-}{}_{(ads)} \quad (2.6)$$

$$O_2^{-}{}_{(ads)} + e^{-} \rightarrow 2O^{-}{}_{(ads)} \quad (2.7)$$

$$2O^{-}{}_{(ads)} + e^{-} \rightarrow O_2^{-}{}_{(ads)} \quad (2.8)$$

Consequently, the resistance of an n-type MOXs gas sensor is increasing as exposed to air, due to the development of a potential barrier. Furthermore, the space charge layer width (W) can be specified using Poisson's equation as follows [12,13]:

$$W = \frac{Q_s}{e.N_D} = \left[\frac{2.K.\varepsilon_0.\Delta\emptyset_s}{e.N_D}\right]^{1/2} \quad (2.9)$$

Q_S - surface charge

N_D - number of ionized donor states per unit volume

K - static dielectric constant of the oxide

ε_O- permittivity of the vacuum

$\Delta\varphi_S$- surface potential barrier height.

For example, with usual values ($K\varepsilon_O \sim 10^{-12}$ F/cm, $N_D \sim 10^{18} - 10^{20}$ cm^{-3} and $\Delta\varphi_S \sim 1V$), the space charge layer thickness is generally around 1 – 100 nm [11].

The electrical conduction is modified subject to the formation of the space charge layer (depletion layer or hole accumulation layer) due to the ionosorption species as shown in Figure 2.2. The change of the potential barrier in air and reducing gas environments due to the variation of the space charge region at each grain boundary, contact and surface of MOXs is shown in Figure 2.3 [14]. Furthermore, the electrical transport mechanism should be modified when the grain size (d_m) becomes low compared to the Debye length (λ_D). In a large grain, (grain size, $d_m >>$ thickness of the space charge layer, $2\lambda_D$), the conductance is limited by Schottky barrier at grain boundaries. Once, $d_m = 2\lambda_D$, conductance is restricted by necks between the grain, (Figure 2.4), while the conductance is highly affected by each grain once

$d_m < 2\lambda_D$. Typically, the lower grain size (d_m) enhances the sensor performance, especially in nanometer dimensions.

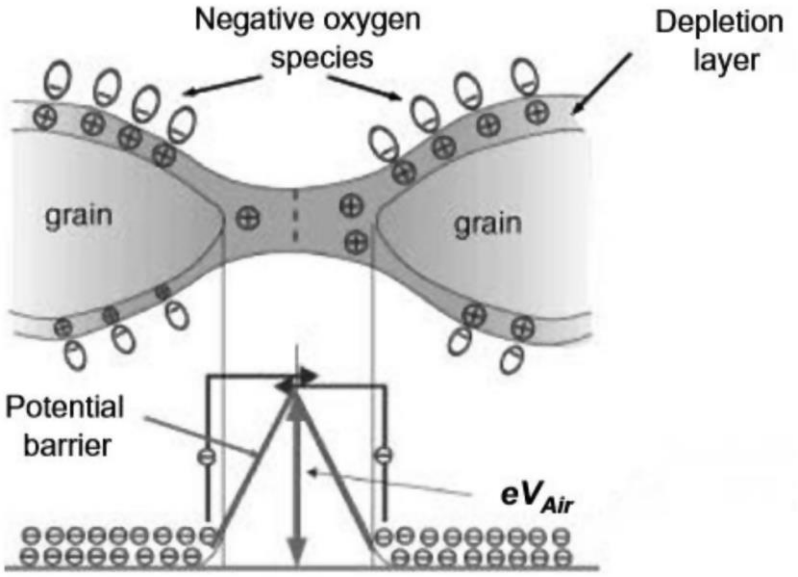

Figure 2.3. Formation of space charge layer in the presence of O_2. V_{Air} is the potential difference between the MOXs surface and the upper barrier in pure air [15].

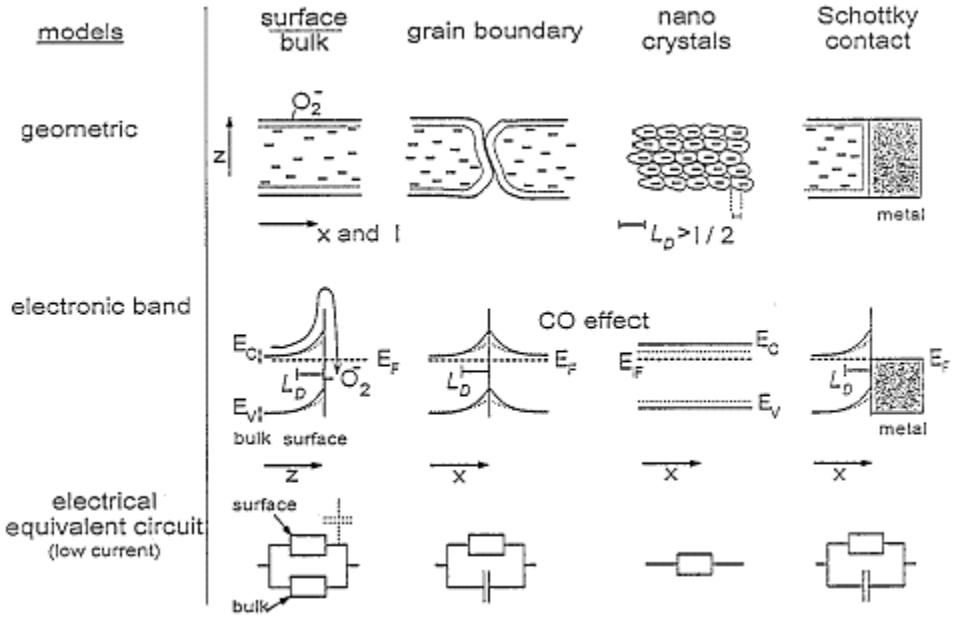

Figure 2.4. Effect of particle size and contacts on resistances and capacitances [14].

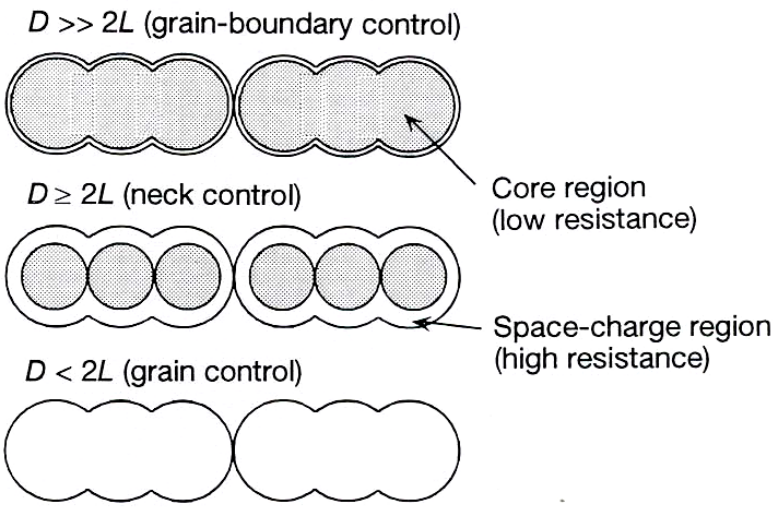

Figure 2.5. Schematic models for grain-size effects [16].

The operating temperature is another important parameter that directly alters the performance of the sensor. In general, higher adsorption/desorption process of the gas molecule, and the best operating temperature of sensors is above 200 °C. Typically, the detection process achieves a highest at an ideal temperature and decreases when the temperature is further increased. Consequently, when the operating temperature rises beyond the optimum value, the oxygen molecules are desorbed at the surface resulting decrement in the resistance by releasing more electrons into the grain of n-type MOXs [15].

Also, doping and decorating MOXs with oxide, noble metals, or carbon structure significantly enhance the surface phenomena. These methods have been well effective in enhancing the sensor performances such as sensitivity, speed, and low operation temperature. Unfortunately, it is not completely understood the mechanism that governs the effect of dopant materials on the sensing process. Besides, it is recognized that the sensitivity and speed are enhanced by the reduction of particle size, microstructural changes, and the alterations in electronics of the MOXs surface.

2.4 Sensor requirements and characteristics

The most important characteristic of sensors is 4 ‘S’: sensitivity (response), speed (response/ recovery time), selectivity, and stability. Besides, limit of detection (LOD), reproducibility, and repeatability are some typically utilized sensing parameters.

The response is generally defined as the fraction of the resistance on the sensing layer when interacting with the analyte gas (R_{gas}) and the one in the air (R_{air}). For instance, the response of an n-type MOXs sensors toward oxidizing analyte in air is shown in Equation 2.10. The sensitivity is described as the derivative of the calibration curve (response vs concentration). Selectivity defines the capability of identifying the target gas as other compound are present. The speed, response time (T_{res}) and recovery time (T_{rec}) are defined as the time required for the electrically transduced signals of the sensor to change to 90% of the saturation/baseline value after exposure to the target/purging gas. Long-term stability is the ability of the active material to keep its properties, such as electrical resistance in case of conductometric sensors, constant over time. The repeatability is the evaluation of the eventual signal change upon exposure to a specific concentration of the gaseous analyte. The coefficient of variation (CV) can be used to characterize either the repeatability of responses or the reproducibility of sensors, equation 2.11. The limit of detection is the least concentration of analyte gas that may be detected by the sensor. LOD can be calculated by two means. One is the IUPAC standard method and the second is the simple 10% response method. The IUPAC method involves when the signal is over three times of the noise level in the system. The root mean square (RMS) deviation at the baseline and the slope of the response curve have been utilized to calculate the noise level and theoretical LOD of a sensor [17,18]. Second method is the relationship of response vs. concentration. Based on the power fitting, the theoretical LOD is calculated to be the concentration with the response of 10% in line with the empirical assumption that $3RMS_{Noise}$ is normally lower than 10%. Lastly, operating temperature is the temperature where the sensor is operating.

$$\text{Response} = \Delta I/I_{air} = (V/R_{air} - V/R_{gas})/ (V/R_{air}) = R_{air}/R_{gas} - 1 \qquad (2.10)$$

I- current

V- DC voltage

R- resistance

$$CV = (R_{SD}/R_{average}) \times 100\% \quad (2.11)$$

R_{SD} - standard deviation

$R_{average}$ - average value of responses

$$LOD = 3.\frac{RMS_{noise}}{Slope} \quad (2.12)$$

Slope - the slope of the fitted curve (response vs concentration

RMS_{noise} - noise of the sensor, which can be calculated as in equation (2.13)

$$RMS_{noise} = \sqrt{\frac{v_x^2}{N}} \quad (2.13)$$

v_x^2 - standard deviation

N - total number of data points

References

[1] Worsfold, P. J. “Classification and Chemical Characteristics of Immobilized Enzymes (Technical Report).” Pure and Applied Chemistry 67, no. 4 (1995): 597–600. https://doi.org/10.1351/pac199567040597.

[2] Röck, Frank, Nicolae Barsan, and Udo Weimar. “Electronic Nose: Current Status and Future Trends.” Chemical Reviews 108, no. 2 (2008): 705–25. https://doi.org/10.1021/cr068121q..

[3] Kumarage, Gayan W., and Elisabetta Comini. “Low-Dimensional Nanostructures Based on Cobalt Oxide (co3o4) in Chemical-Gas Sensing.” Chemosensors 9, no. 8 (2021): 197. https://doi.org/10.3390/chemosensors9080197.

[4] Kumarage, Gayan W.C., and Elisabetta Comini. “Conductometric Gas Sensors.” Reference Module in Materials Science and Materials Engineering, 2023. https://doi.org/10.1016/b978-0-12-819728-8.00060-7.

[5] Brattain, Walter H., and John Bardeen. “Surface Properties of Germanium.” Bell System Technical Journal 32, no. 1 (1953): 1–41. https://doi.org/10.1002/j.1538-7305.1953.tb01420.x.

[6] Seiyama, Tetsuro, Akio Kato, Kiyoshi Fujiishi, and Masanori Nagatani. “A New Detector for Gaseous Components Using Semiconductive Thin Films.” Analytical Chemistry 34, no. 11 (1962): 1502–3. https://doi.org/10.1021/ac60191a001.

[7] Galstyan, Vardan, Abderrahim Moumen, Gayan W.C. Kumarage, and Elisabetta Comini. “Progress towards Chemical Gas Sensors: Nanowires and 2D Semiconductors.” Sensors and Actuators B: Chemical 357 (2022): 131466. https://doi.org/10.1016/j.snb.2022.131466.

[8] Korotcenkov, G., and B.K. Cho. “Instability of Metal Oxide-Based Conductometric Gas Sensors and Approaches to Stability Improvement (Short Survey).” Sensors and Actuators B: Chemical 156, no. 2 (2011): 527–38. https://doi.org/10.1016/j.snb.2011.02.024.

[9] Moumen, Abderrahim, Gayan C. Kumarage, and Elisabetta Comini. “P-Type Metal Oxide Semiconductor Thin Films: Synthesis and Chemical Sensor Applications.” Sensors 22, no. 4 (2022): 1359. https://doi.org/10.3390/s22041359.

[10] Kurugundla Krishna, Kurugundla Gopi, Saidireddy Parne, Nagaraju Pothukanuri, Velavan Kathirvelu, Suman Gandi, and Dhananjay Joshi. “Nanostructured Metal Oxide Semiconductor-Based Gas Sensors: A Comprehensive Review.” Sensors and Actuators A: Physical 341 (2022): 113578. https://doi.org/10.1016/j.sna.2022.113578.

[11] Möbius, Hans-Heinrich. “Solid State Gas Sensors: Herausgegeben Von P. T. Moseley Und B. C. Tofield; Bristol, Philadelphia, Adam Hilger, 1987; Zeitschrift für Chemie 29, no. 7 (2010): 268–68. https://doi.org/10.1002/zfch.19890290730.

[12] Barsan, Nicolae, and Udo Weimar. Journal of Electroceramics 7, no. 3 (2001): 143–67. https://doi.org/10.1023/a:1014405811371.

[13] Barsan, N., C. Simion, T. Heine, S. Pokhrel, and U. Weimar. “Modeling of Sensing and Transduction for P-Type Semiconducting Metal Oxide Based Gas Sensors.” Journal of Electroceramics 25, no. 1 (2009): 11–19. https://doi.org/10.1007/s10832-009-9583-x.

[14] Göpel, Wolfgang, and Klaus Dieter Schierbaum. “SnO_2 Sensors: Current Status and Future Prospects.” Sensors and Actuators B: Chemical 26, no. 1-3 (1995): 1–12. https://doi.org/10.1016/0925-4005(94)01546-t.

[15] Nunes Simonetti, Evelyn Alves, Thais Cardoso de Oliveira, Ádamo Enrico do Carmo Machado, Amanda Alvarenga Coutinho Silva, Alan Silva dos Santos, and Luciana de Simone Cividanes. “TiO_2 As a Gas Sensor: The Novel Carbon Structures and Noble

Metals as New Elements for Enhancing Sensitivity – a Review." Ceramics International 47, no. 13 (2021): 17844–76. https://doi.org/10.1016/j.ceramint.2021.03.189.
[16] Shimizu, Yasuhiro, and Makoto Egashira. "Basic Aspects and Challenges of Semiconductor Gas Sensors." MRS Bulletin 24, no. 6 (1999): 18–24. https://doi.org/10.1557/s0883769400052465..
[17] Wang, Chen, Yinglin Wang, Pengfei Cheng, Luping Xu, Fan Dang, Tianliang Wang, and Zhaohui Lei. "In-Situ Generated TiO_2/α-Fe_2O_3 Heterojunction Arrays for Batch Manufacturing of Conductometric Acetone Gas Sensors." Sensors and Actuators B: Chemical 340 (2021): 129926. https://doi.org/10.1016/j.snb.2021.129926.
[18] Song, Zhilong, Zeru Wei, Baocun Wang, Zhen Luo, Songman Xu, Wenkai Zhang, Haoxiong Yu, et al. "Sensitive Room-Temperature H2s Gas Sensors Employing SnO_2 Quantum Wire/Reduced Graphene Oxide Nanocomposites." Chemistry of Materials 28, no. 4 (2016): 1205–12. https://doi.org/10.1021/acs.chemmater.5b04850.

CHAPTER 3

Experimental procedure

3.0 Background

This chapter focuses on the procedures and general conditions used during the preparation of various MOXs nanostructures and gas sensing devices, rather than providing a detailed theoretical description. The most used techniques are thermal oxidation and hydrothermal, which have been widely discussed in the literature and will not be covered in depth. The emphasis is on the experimental techniques used in the fabrication of the samples. Furthermore, a brief discussion of the employed characterization techniques is included in the latter part of this chapter.

3.1 Processing

3.1.1 Substrate preparation

Nanostructures were grown on alumina (2 mm × 2 mm, Al_2O_3, Kyocera, Japan) substrate for conductometric gas testing and characterization. Prior to the deposition, all the Al_2O_3 substrates were ultrasonically cleaned for 15 min in an acetone ((C_3H_6O, Carlo Erba, Milano, Italy)) bath and then dried with synthetic air to remove dust particles. Additionally, Al_2O_3 substrates (3 mm×3 mm, Kyocera, Japan) were cleaned by using the same procedure for morphological and structural evaluation of the grown nanostructures.

3.1.2 Magnetron sputtering

Magnetron sputtering is a process that involves the use of a magnetron, a type of cathode, to generate plasma in a vacuum chamber. The plasma is then used to sputter, or physically remove, material from a target, which is then deposited onto a substrate. The process is widely used in the manufacturing of thin films, such as those used in coatings and semiconductors. Besides, magnetron sputtering is a popular technique due to its ability to produce high quality, uniform films with precise control over the thickness and composition of the deposited material.

In this dissertation study, direct current (DC) magnetron, has been used to deposit the metal catalysts: Pt, metal layers: Co, and electrodes/heaters: Pt, TiW. Also, DC sputtering has been

used to functionalize the grown Co_3O_4 nanostructures with Pt (Table 3.1). In this process, a DC power supply is used to create an electric field between a target material and a substrate, while a magnetic field is applied to the target material to increase the plasma density and improve the sputtering efficiency. The high-energy ions from the plasma are directed toward the substrate, where they collide with the surface, knock out the atoms from the target and allow the deposition a thin film onto the substrate positioned normally in line with the target. Furthermore, the preparation of several Co thin films for the creation of Co_3O_4/ZnO composite nanowires often involves the use of Radio Frequency (RF) sputtering. This method employs an alternating current power source to generate a plasma, in which a self-sustaining discharge is created by applying a radio frequency voltage to the target material. This results in the ionization of the target material.

Figure 3.1 shows a picture of the sputtering plant used in this work, made by Kenotec company (Italy). The magnetron sputtering system is made up of two separate chambers: the main, circular chamber where the deposition takes place and can hold up to four different target materials. The smaller, tubular chamber is known as the load-lock chamber where samples are placed before the deposition process without disrupting the vacuum in the main chamber. The two chambers are connected by a gate valve. A turbomolecular drag pumping station (TMH 064 D E) is used to create the vacuum in the load-lock chamber, with an electronic drive unit. Meanwhile, the main chamber is evacuated using a rotary and turbomolecular pump, specifically an Edwards Rotary Vane pump (RV12) with a maximum displacement of 17 m^3/h, maximum pumping speed of 14.2 m^3/h, and an ultimate total pressure of around 10^{-3} mbar.

The magnetron sputtering system is composed of a process chamber that has a designated home position and can accommodate four different target positions. Two of these positions are connected to a DC power supply while the other two are connected to an RF power supply (with a maximum power of 600W). The position of the sample holder is controlled by a step-by-step motor that is operated by a computer. The properties of the deposited film can be adjusted by adjusting parameters such as temperature (ranging from room temperature to 300 °C), plasma composition (using argon and oxygen from two separate lines, which have their flux and pressure controlled by two mass-flow controllers), the pressure within the chamber, and the applied electrical power. The system is fully controlled by custom Microsoft Access/Visual Basic software.

Figure. 3.1. Illustration of (a) The sputtering system, (b) the arrangement of the metal target inside the main chamber, (c) the dimension of the sputtering chamber.

Table 3.1. Parameter used in DC magnetron sputtering to deposit metals.

Parameters	Materials					
	Co	Co	Pt	Pt	Pt	TiW
Power (W)	50	100	50	75	75	75
Method	DC	RF	DC	DC	DC	DC
Temperature (°C)	RT	RT	RT	300	300	300
Time (s)	300 -600	1200	2	180	1200	180
Ar flow (sccm)	7	7	7	7	7	7
Pressure ($\times 10^{-3}$ m.Torr)	4.6	4.6	4.6	5.5	5.5	5.5
Usage	Thin film	Thin film	Catalyst Functionalizing	Adhesion pads	Electrodes Heaters	Adhesion pads

3.1.3 Co_3O_4/ZnO composite nanowires

The Co_3O_4/ZnO composite nanowires were synthesized through in-situ thermal oxidation and physical vapor deposition (PVD) in a specialized thermal evaporator chamber at the Sensors lab of the University of Brescia. The diagram illustrating the process of preparing and gas sensing the composite nanowires is presented in Figure 3.2.

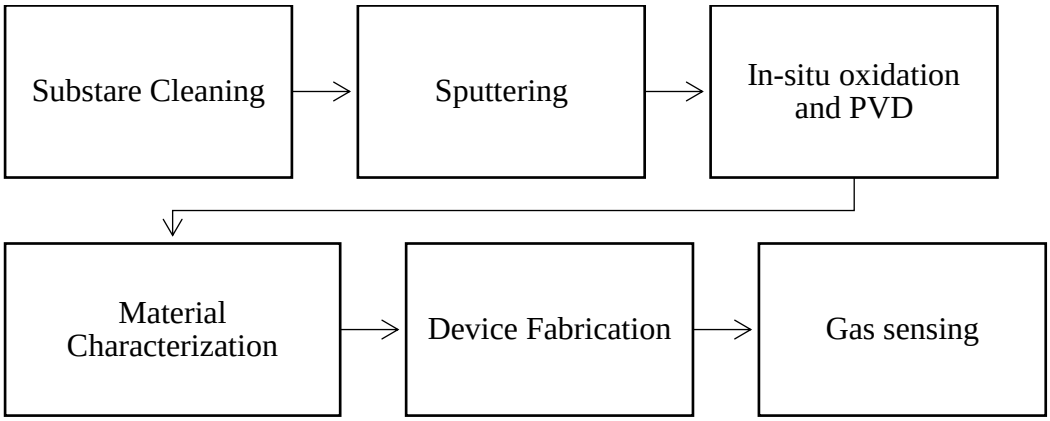

Figure 3.2. The block diagram of synthesis and characterization of ZnO/Co_3O_4 nanowires.

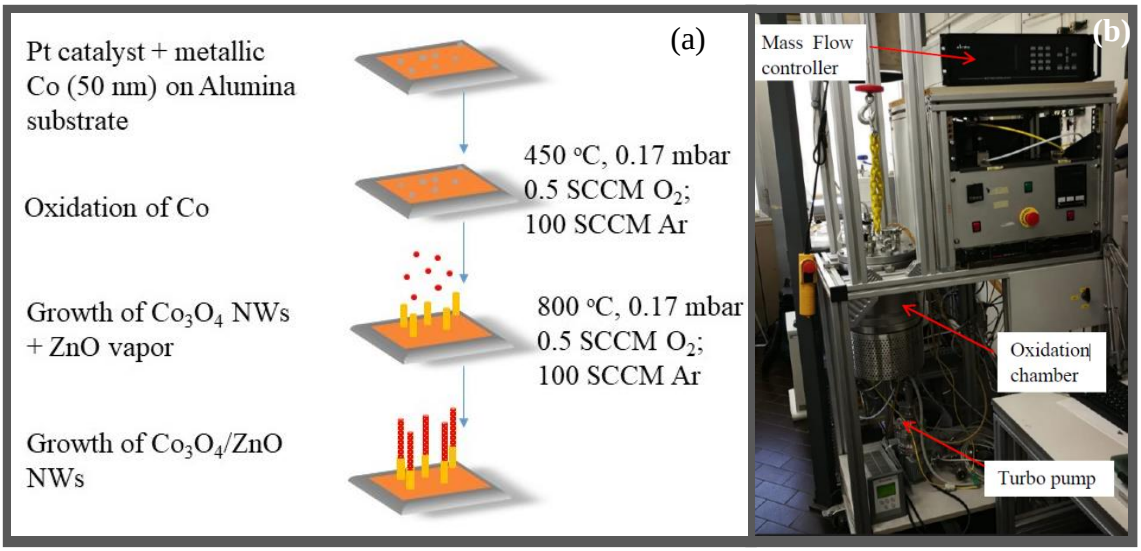

Figure 3.3. Illustration of (a) The visual interpretation of growth steps, (b) thermal evaporator used to prepare the ZnO/Co_3O_4 composite nanowires.

The process of preparing Co_3O_4/ZnO nanowires consists of several steps as illustrated in Figure 3.2. Initially, Al_2O_3 substrates (2 mm × 2 mm) were cleaned as outlined in section 3.1.

Subsequently, a thin layer of Co (50-100 nm) was deposited on the cleaned Al_2O_3 substrates using RF magnetron sputtering techniques with the parameters specified in Table 3.1. The Co thin metallic films (100 nm) were prepared by applying an RF plasma with the given parameters in Table 3.1. An ultra-thin layer of Pt (2-5 nm) was then deposited on top of the Co layer as a catalyst using DC magnetron (Table 3.1). The samples were subsequently placed into an oxidation chamber along with ZnO powder (99.9% purity, Sigma Aldrich) and heated to 450 °C at a rate of 20 °C per minute, under a pressure of 0.17 mbar and a flow of 100 sccm Ar and 0.5 sccm O_2 . The growth steps and oxidation chamber are illustrated in Figure 3.3 (a,b). The temperature was then elevated to 800 °C at a rate of 10 °C per minute, where the experiment was conducted for 3 hours at 800 °C at a pressure of 0.17 mbar.

3.1.4 Co_3O_4 nanowalls

A thin layer of Co (100 nm) was deposited on cleaned Al_2O_3 (2 mm × 2 mm) substrates using DC magnetron sputtering, with the parameters specified in Table 3.1. The samples were then immersed in 5 ml of distilled water (Carlo Erba Reagents S.A.S, France) in 25 mL glass beakers and boiled for 15 minutes until the water evaporated. Afterwards, the boiled samples were annealed at 280 °C for 6 hours on a hot plate in the air. Subsequently, the prepared Co_3O_4 nanostructures were functionalized with Pt nanoparticles using the parameters in Table 3.1. The key experimental steps are outlined in block diagram 3.4.

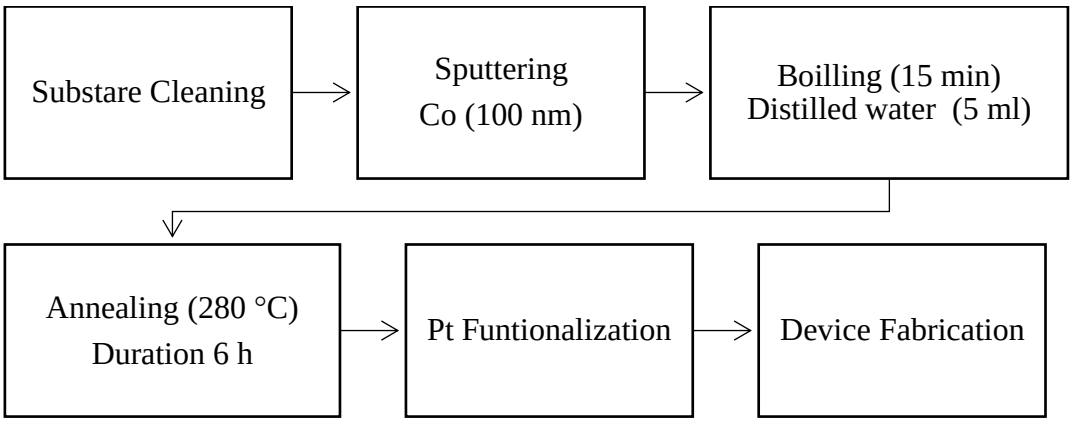

Figure 3.4. Block diagram for Co_3O_4 nano walls preparation.

3.4.1.1 Growth mechanism of Co_3O_4 nanowalls

The mechanism of growth for Co_3O_4 nanowalls that are produced by the thermal oxidation of Co foils has been previously explored [1,2]. However, the specific mechanism for the growth of Co_3O_4 nanowalls and nanowires in an atmospheric environment is not yet fully understood. However, the literature suggests the following mechanism for the growth of Co_3O_4 nanowalls (Figure 3.5) [3,4]:

The growth of Co_3O_4 nanowalls begins with the melting of the surface of the Co film at temperatures close to 300 °C, which creates liquid Co. Oxygen from the surrounding air diffuses into the liquid Co and causes oxidation, forming a thin layer of CoO on the surface of the Co film. Mantaining the oxidation process leads to the formation of Co_3O_4 on the surface of the CoO layer. Co_3O_4 will precipitate after saturation in a liquid state and the nanowalls start to grow. With longer oxidation times, the length of the nanowalls increases. This process stops upon cooling the substrates, as the liquid condenses into solid Co_3O_4 nanowalls. This two-step oxidation process continues deeper within the Co film as the oxidation time is prolonged. The growth mechanism of Co_3O_4 nanowalls is similar to the solid-liquid-solid (SLS) process [1,5].

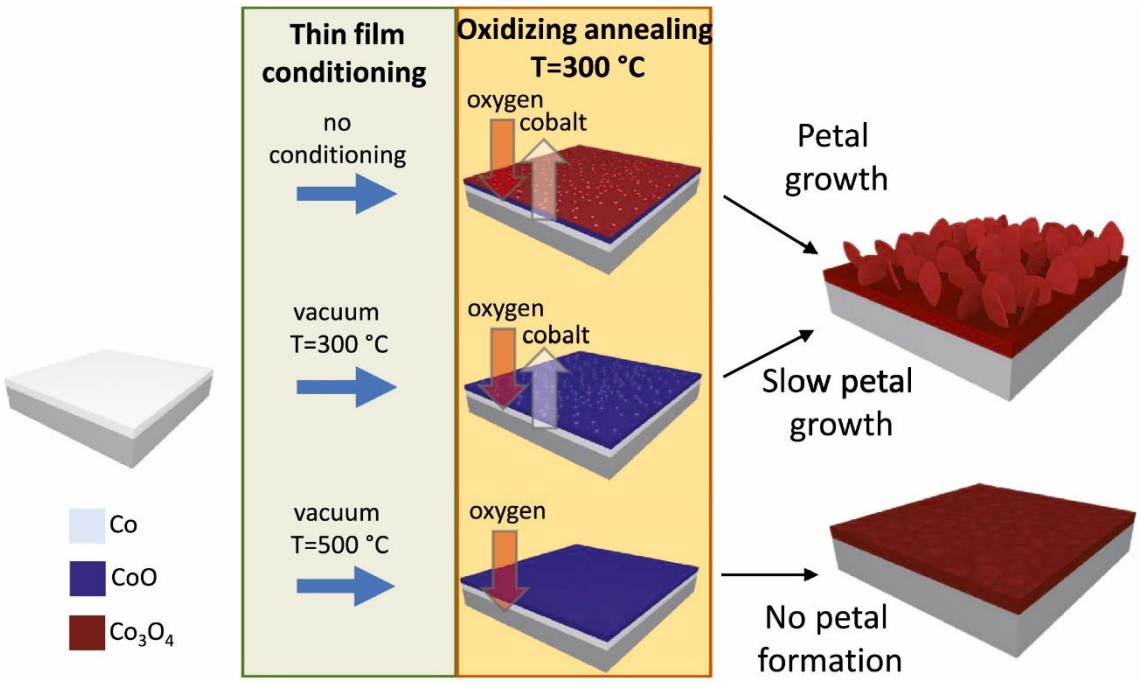

Figure 3.5. Sketch of the Co_3O_4 petal/walls formation process by oxidizing annealing of a metallic film [6].

3.1.5 Co_3O_4 nanowires

The experimental procedure began with cleaning the Al_2O_3 (2 mm x 2 mm) by sonication as described in section 3.1. Then, thin layers (50 nm and 100 nm) of metallic Co were deposited on the cleaned Al_2O_3 using Co plasma (DC) with the parameters specified in Table 3.1. The metallic Co films were subsequently thermally oxidized at a temperature of 300 °C under a pressure of 2.2 mbar and an Ar flow of 100 sccm for 3 hours in the oxidation chamber illustrated in Figure 3.3 (b). The process of preparation of Co_3O_4 nanowires is depicted in the block diagram of Figure 3.6.

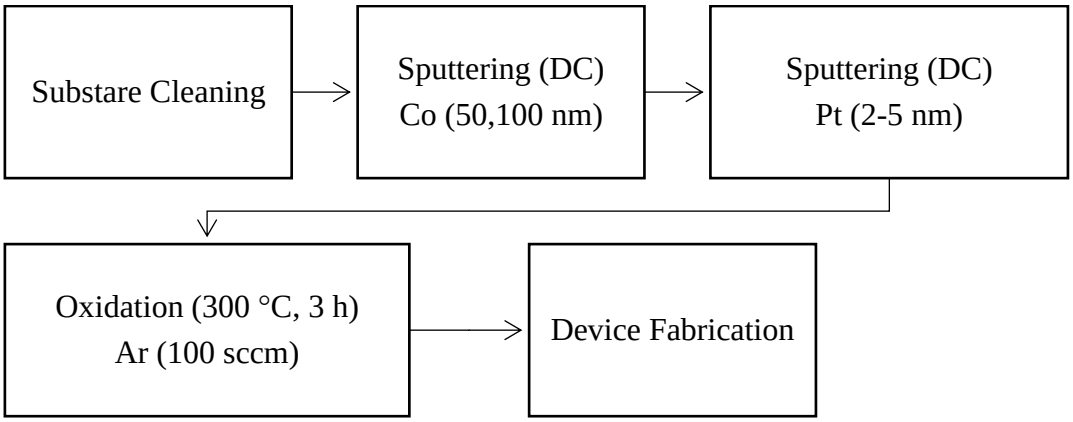

Figure 3.6. Block diagram for Co_3O_4 nanowires preparation.

3.5.1.1 Growth mechanism of Co_3O_4 nanowires

The Gibbs free energy of the reaction is an important measurement in determining possible reactions. A study by Li et al. found that the reaction between Co and O_2 has a negative value, which can lead to the formation of CoO and Co_3O_4 [7]. This results in the formation of cobalt oxide films and nanowires [8,9]. Based on previous research, it is believed that the nanowires are composed of three layers: Co as the bottom layer, CoO as the intermediate layer, and Co_3O_4 as the top layer [10-12]. Consequently, the schematic of mass transport phenomena is illustrated in Figure 3.7. The formation of the nanowires is prominent on the grain rather than the grain boundaries (Figure 1(d)) [13,14]. The lattice mismatch at the interface of the Co/CoO and the CoO/Co_3O_4 generates significant stress at the interface. Stress at the interfaces between these layers is thought to drive the diffusion of Co ions, which is facilitated by grain boundaries. Subsequently, Co ions diffuse from higher to lower

concentration Co_3O_4 nanowires roots i.e Co-CoO and CoO-Co_3O_4 as shown in Figure 3.7 [2,13]. In this context, grain boundaries offer a significant role by forming a path for the diffusion of Co ions [13].

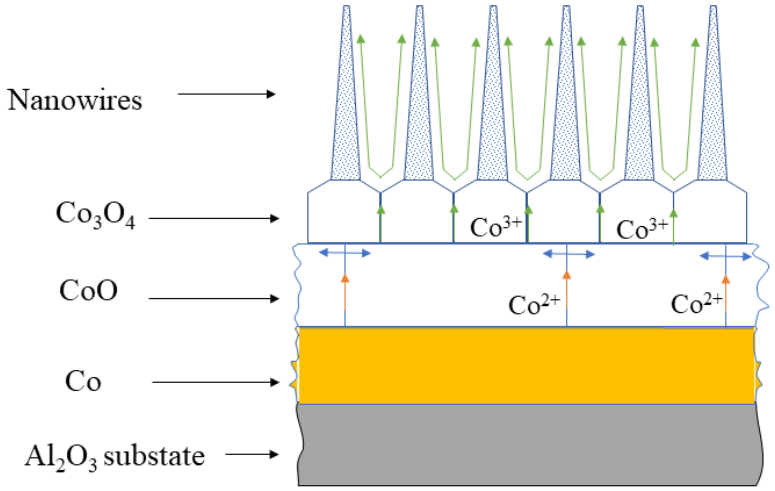

Figure 3.7. Schematic illustration of the mass flow phenomena of the formation of the Co_3O_4 nanowires.

3.1.6 TiO_2 nanobelts

The alkali-hydrothermal method was used to synthesize TiO_2 nanobelts. The process began by creating sodium titanate hydrate ($Na_2Ti_3O_7.mH_2O$) through hydrothermal means. A 1.0 g of titanium dioxide (TiO_2, powder, 21 nm primary particle size, ≥99.5%, Aldrich) was mixed with 70 mL of 10.0 $mol.dm^{-3}$ sodium hydroxide (NaOH, 98%, Loba Chemie, India) aqueous solution and mechanically stirred for 30 minutes followed by 15 minutes of ultrasonication. The stirring and sonication processes were repeated six times following each other. After that, the resulting mixture was placed in a 100 mL Teflon-lined stainless-steel autoclave and thermally treated for 48 hours at five different temperatures: 120 °C, 135 °C, 150 °C, 175 °C, and 200 °C. After that, the material was cooled down to room temperature. The resultant white slurry ($Na_2Ti_3O_7$) was washed thoroughly with deionized water followed by a filtration process until the pH of the washing solution reach the value of 7. Then, the wet slurry was soaked in 1 $mol.dm^{-3}$ acetic acid (99.5%, DAEJUNG) aqueous solution for 24 h to form protonated titanate form ($H_2Ti_3O_7$). The prepared $H_2Ti_3O_7$ was washed thoroughly with

distilled water and filtration till the washing solution become pH neutral. Later the obtained $H_2Ti_3O_7$ was dried at 80 °C for 24 hours, and then calcinated at 500 °C for 3 hours.

The basic chemical routing of the TiO_2 nanobelt growth can be written as follows [13].

The reaction starts with the dissolving of TiO_2, in the presence of NaOH.

$$3TiO_{2(s)} + 2NaOH_{(aq)} \rightarrow Na_2Ti_3O_{7(s)} + H_2O_{(l)} \quad (3.1)$$

During the CH_3COOH washing, the $Na_2Ti_3O_7$ nanobelt is known to convert as follows due to the ion exchange.

$$Na_2Ti_3O_{7(s)} + 2CH_3COOH_{(aq)} \rightarrow H_2Ti_3O_{7(s)} + 2CH_3COO^-Na^+_{(aq)} \quad (3.2)$$

In the calcination process, $H_2Ti_3O_7$ will convert to TiO_2.

$$H_2Ti_3O_{7(s)} \rightarrow 3TiO_{2(s)} + H_2O(g) \quad (3.3)$$

3.1.6.1 Growth mechanism of TiO_2 nanobelts

The formation of $H_2Ti_3O_7$ from anatase TiO_2 is a crucial step in the creation of nanobelt-like morphology in the final product, which is a result of the Dissolution-Recrystallization process. As OH^- ions from a NaOH solution infiltrate the initial 3D anatase TiO_2, the Ti–O–Ti bonds are broken down and single-layered sheets (nanosheets) made of TiO_6 octahedra are exfoliated [15]. As the TiO_6 sheets are formed, Na^+ ions insert themselves in the space between them to counterbalance the negative charge. This action regulates the Na/Ti proportion of the final titanate product, resulting in the formation of intermediate sodium titanate ($Na_2Ti_3O_7$), as expressed in equation (3.1) [16]. Dissolution and exfoliation are more effortless for small anatase precursor particles, resulting in the formation of sodium titanate sheet units. These sheet units replicate the epitaxial crystal growth along the c-axis, leading to the development of sheet-like structures (Figure 3.8 (a)) [17]. Next, $Na_2Ti_3O_7$ nanosheets are transformed into $H_2Ti_3O_7$ nanobelts when the ion exchange process is employed (equation (3.2) and Figure 3.8 (b)). Accordingly, the formation of nanobelts-like structure is ascribed to the splitting of nanosheets to release the excess strong stress upon the replacement of Na^+ by larger H_3O^+ cations when forming $H_2Ti_3O_7$ [18]. Finally, TiO_2-B nanobelts are obtained by annealing the $H_2Ti_3O_7$ at 500 °C as presented in equation (3.3) and Figure 3.8 (c).

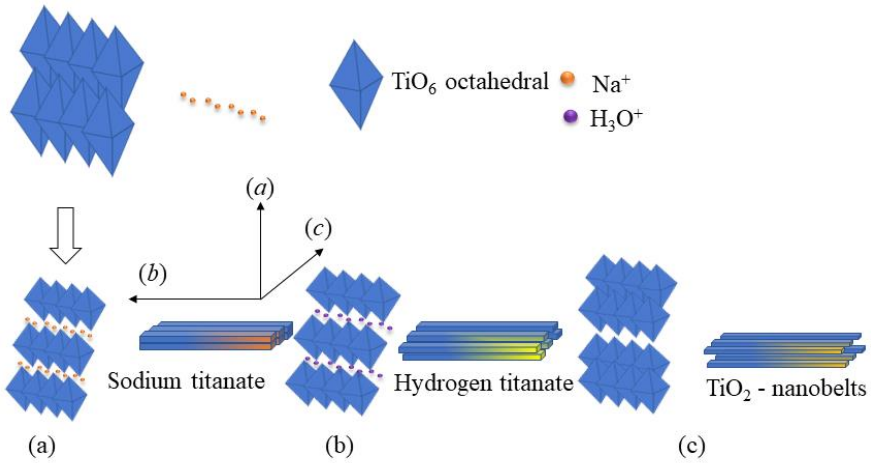

Figure 3.8. Schematic formation of (a) sodium titanate ($Na_2Ti_3O_7$) nanosheets (b) hydrogen titanate ($H_2Ti_3O_7$) nanobelts (c) TiO_2 nanobelts.

3.1.7 Nb_2O_5 microcolumns

Nb_2O_5 microcolumns were produced through a method previously described [19]. The starting material used for the synthesis of Nb_2O_5 microcolumns was commercially available Nb_2O_5 powder (325 mesh, 99.9% trace metals basis, Sigma Aldrich). The process began by adding 1.0 g of commercial Nb_2O_5 powder to 64 mL of 10 $mol.dm^{-3}$ Sodium Hydroxide (NaOH, AR, 98%, TECHNO PHARMCHEM HARYANA, India) solution and stirring for 30 minutes, followed by ultrasonication for 15 minutes. The process of agitation and ultrasonication was repeated four times. The obtained precursor was transferred into an 80 mL autoclave and placed in an oven at a temperature of 180 ℃ for 30 minutes and cooled to room temperature by natural cooling. After that, the precipitate was collected and washed with 1 $mol.dm^{-3}$ CH_3COOH (300 ml) followed by deionized water (400 ml, DI, 0.055 µS cm^{-1}). This washing process is repeated four times. The product was dried in a vacuum oven at 60 °C for 24 hours, which was named as Nb_2O_5-30. The same procedure was repeated for three different reaction times (60, 120, 180 minutes) and named as Nb_2O_5-60, Nb_2O_5-120, Nb_2O_5-180 respectively. Finally, as-synthesized Nb_2O_5 microcolumns (Nb_2O_5-30) were

calcined at 500 °C for 3 h to get hexagonal phase (Nb_2O_5-30/700 °C). The basic chemistry behind the formation of Nb_2O_5 microcolumns growth can be written as follows [20]:
The reaction starts with dissolving of Nb_2O_5, in the presence of NaOH.

$$Nb_2O_{5(s)} + 2NaOH_{(aq)} \rightarrow 2NaNbO_{3(s)} + H_2O_{(l)} \quad (3.4)$$

During the CH_3COOH washing due to ion exchange:

$$NaNbO_{3(s)} + CH_3COOH_{(aq)} \rightarrow HNbO_{3(s)} + CH_3COO^-Na^+_{(aq)} \quad (3.5)$$

In the calcination process (700 °C), $HNbO_3$ will convert to Nb_2O_5.

$$2HNbO_{3(s)} \rightarrow Nb_2O_{5(s)} + H_2O_{(g)} \quad (3.6)$$

3.1.7 Device fabrication

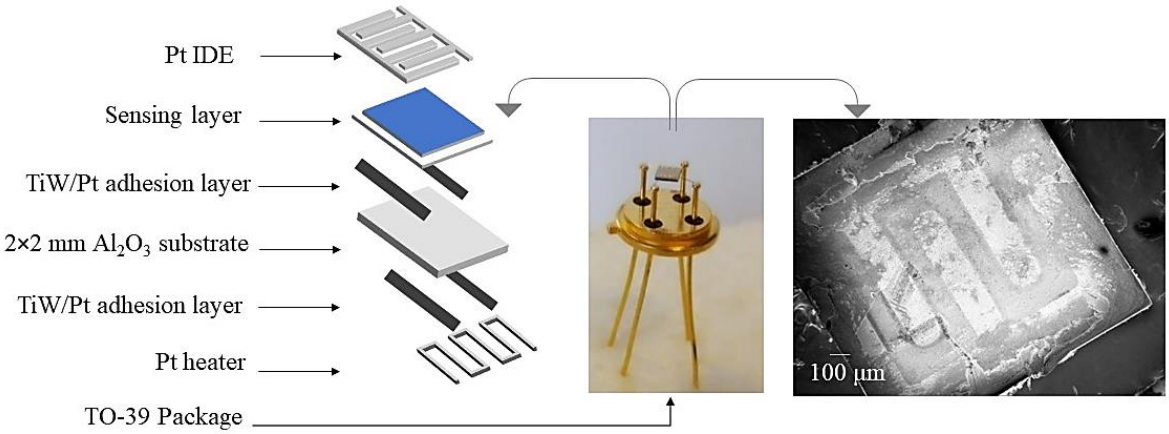

Figure 3.9. Schematic of fabricated sensor device.

The following steps were utilized to fabricate the conductometric gas sensing devices:

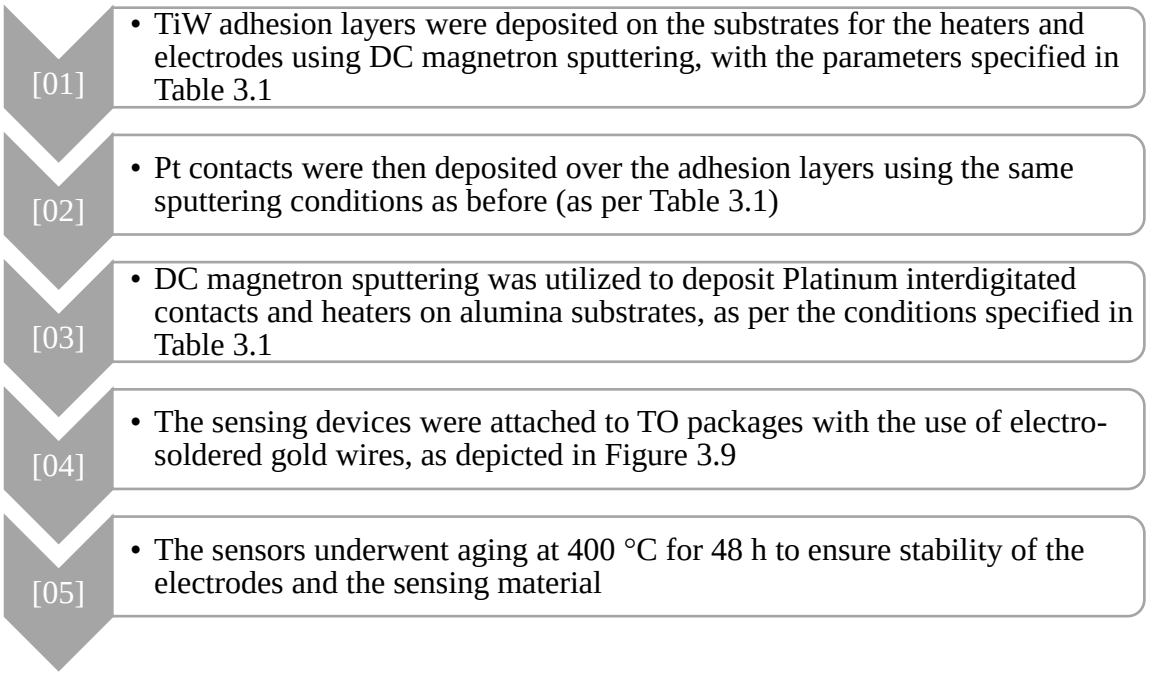

Figure 3.10. The steps of fabricating gas sensing device.

3.2 Material characterization

3.2.1 Crystallographic data collection and structure determination

The crystallographic analyses of the fabricated samples were done using X-ray diffraction (XRD), RAMAN at the Sensors Laboratory, and High resolution transmission electron microscopy (HR-TEM) techniques at Atomic Structures and Defects in Advanced Materials Laboratory, Bucharest, Romania.

3.2.1.1 X-ray Diffraction

The XRD measurements were performed using PANalytical X-ray diffractometer GIXRD (Figure 3.11), The Cu Kα radiation with λ=1.54184 Å was used in continuous mode at a generator voltage of 40 kV, 40 mA tube current. 0.05° scan step size and step time of 25 s was used in the 2θ in the range of 20 – 80°.

Figure 3.11. Panalytical diffractometer at the SENSOR Lab, Brescia, Italy- PANalytical.

3.2.1.2 Raman spectroscopy

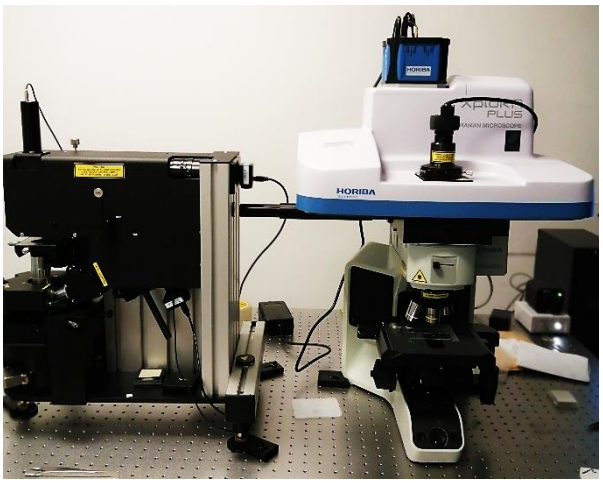

Figure 3.12. Raman instrument at the SENSOR Lab, Brescia, Italy- HORIBA, XploRA Nano.

Raman spectra (HORIBA) (Figure 3.12) were employed to evaluate the morphological, maps for elemental and structural properties of the prepared nanostructures. Raman spectra were measured using a fiber-coupled 124 confocal optical microscope (HORIBA, XploRA Nano) at 100× magnification. Spectra were 125 recorded in the wavelength range of 200 - 1200 cm^{-1} using a red laser source (638 nm).

3.2.1.3 High resolution transmission electron microscopy

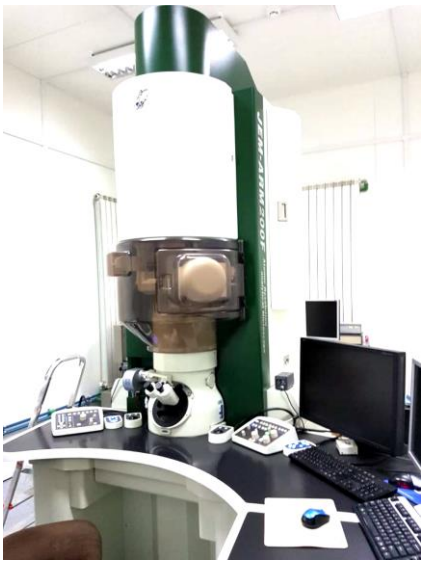

Figure 3.13. Transmission electron microscopy at the Atomic Structures and Defects in Advanced Materials Laboratory, Bucharest, Romania- a JEOL ARM-200F.

The transmission electron microscopy technique involves using a beam of electrons to pass through an ultrathin sample. As the electrons interact with the specimen, an image is formed through the electrons transmitted through the sample, magnified and focused by an objective lens. In this study, TEM images were taken using a JEOL ARM-200F analytical transmission 119 electron microscope operated at 200 kV, as shown in Figure 3.13. Also, TEM is equipped with an EDS detector to acquire 120 Energy Dispersive X-ray (EDS) spectra or maps for elemental investigation. The TEM, HR-TEM and EDS are performed at the from the Atomic Structures and Defects in Advanced Materials Laboratory, Bucharest, Romania.

3.2.2 Morphological evaluations

3.2.2.1 Field emission scanning electron microscope (FE-SEM)

Figure 3.14. Field Emission - Scanning Electron Microscope at the SENSOR Lab, Brescia, Italy- TESCAN-MIRA 3.

The Field Emission-Scanning Electron Microscope (FE-SEM) is capable of imaging organic and inorganic materials at nanoscale resolution. In this study, the surface morphology of nanostructures was examined using a TESCAN-MIRA 3 as shown in Figure 3.14. The samples were attached to a metallic stick using carbon glue tape to minimize charging effects. The SEM was typically operated at 3-5 kV, with a beam current of 130 μA, and a high vacuum of 10^{-10} Torr for the gun chamber and 10^{-6} Torr for the specimen chamber.

3.2.3 Magnetic resonance

3.2.3.1 Electron paramagnetic resonance (EPR)

Figure 3.15. Electron paramagnetic resonance at the Atomic Structures and Defects in Advanced Materials Laboratory, Bucharest, Romania- bruker ELEXSYS E580 spectrometer in the X-band and an ELEXSYS E500Q.

Electron Paramagnetic Resonance characterization, is one of the most informative techniques on the electronic structure of paramagnetic species, would be very useful study. Thus, EPR is the most direct and powerful method for the detection and identification of metal complexes with unpaired electrons and free radicals. Subsequently, interpretation of the electron paramagnetic resonance spectrum can provide confirmatory information on the magnetic susceptibility of the synthesis materials. Accordingly, EPR measurements were conducted using Bruker ELEXSYS E580 and E500Q spectrometers operating in the X-band (9.8 GHz) and Q-band (34 GHz) respectively, equipped with CF935 continuous flow cryostats from Oxford Instruments. For the EPR investigations the Co_3O_4 samples were deposited on alumina substrates cut into 1.4 x 1.4 mm^2 squares. For the X-band measurements three such samples were inserted in a 3 mm i. d. quartz tube, while for the Q-band measurements only one sample was inserted in a 2 mm i.d. quartz tube. The samples were submitted to thermal aging at 400 ^oC in air for 8 hours in a temperature stabilized (± 1^o) furnace (Figure 3.15).

3.3 Electrical characterization

3.3.1 Gas sensing system

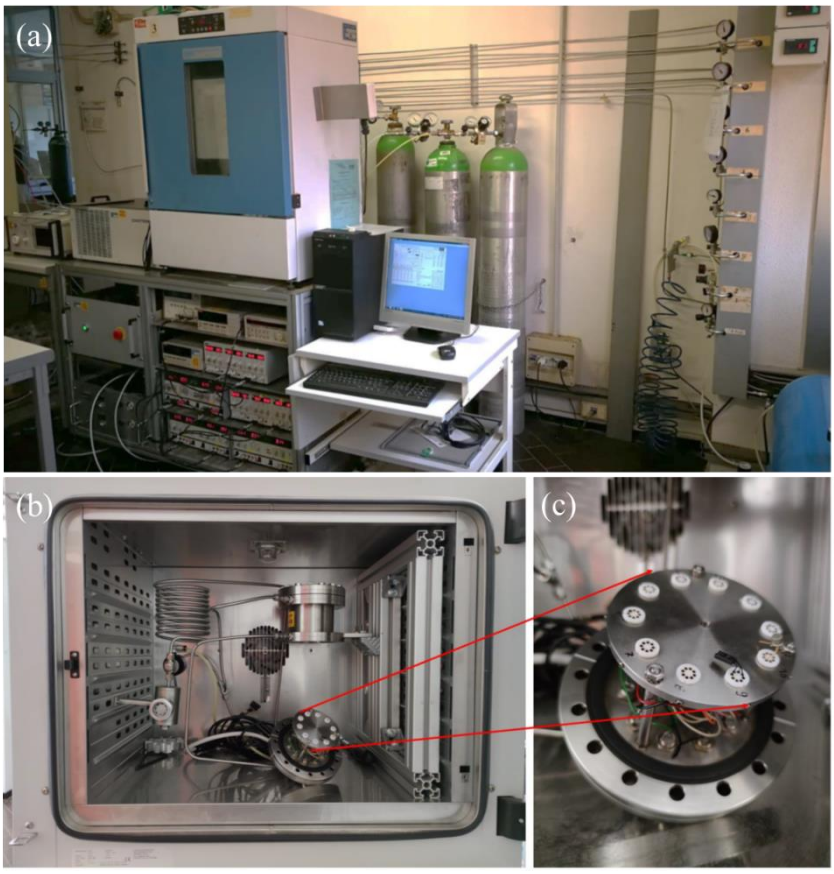

Figure 3.16. Illustration of (a) The functional testing system, (b) gas sensing chamber with sensor hub, (c) the sensors hub.

The functional testing system (Figure 3.15 (a-c)) uses a climatic chamber to maintain a constant temperature of 20 °C in the stainless-steel test chamber. The testing system ((Figure 3.15 (b)) allows for testing of various sensors under various conditions, including different atmospheres, temperatures, and humidity levels. The testing system has the capacity to hold up to ten sensors at once, enabling simultaneous measurement of their performance. The conductometric responses of the sensors were tested in a stainless steel chamber with a volume of 1 L, which is located inside a climatic chamber. A Dreschel bottle in a thermostatic bath set at 25 °C generates a saturated humid airflow, which is then mixed with synthetic dry air to reach the desired relative humidity (RH) level. A humidity sensor from Vaisala (Finland, model HMI 36) was utilized to monitor the atmosphere inside the test chamber and to regulate the flow of dry and humid air. Measurements were taken at a different humidity level for example, 40 RH% with a flow rate of 200 sccm.

The sensors were evaluated at various working temperatures ranging from 100 to 500 ºC and were stabilized for 10 hours at each temperature before being exposed to gases. Thurlbly-Thander PL330DP power supplies were used to apply controlled voltage to the heaters to reach the desired test temperatures for the sensors. A fixed voltage of 1 V was applied to the sensors, and their conductance was measured using specialized picoammeters from Keithley (6485). The sensors were subjected to fixed concentrations of target gases, provided by SIAD SPA (Italy), such as ethanol (C_2H_6O), acetone (C_3H_6O), methanol (CH_4), hydrogen (H_2), nitrogen dioxide (NO_2), carbon monoxide (CO), ammonia (NH_3) and hydrogen sulfide (H_2) for 20 min, and then the synthetic airflow was restored for 45 min to return to the baseline.

Depending on the semiconducting nature of the sensitive material, the gas response is calculated using the formulas:

For n-type MOXs

For reducing gas $$\frac{G_{gas}-G_{air}}{G_{air}}=\frac{\Delta G}{G} \quad (3.7)$$

For oxidizing gas $$\frac{G_{air}-G_{gas}}{G_{gas}}=\frac{\Delta G}{G} \quad (3.8)$$

For p-type MOXs

For reducing gas $$\frac{G_{air}-G_{gas}}{G_{gas}}=\frac{\Delta G}{G} \quad (3.9)$$

For oxidizing gas $$\frac{G_{gas}-G_{air}}{G_{air}}=\frac{\Delta G}{G} \quad (3.10)$$

References

[1] Yu, T., Y. W. Zhu, X. J. Xu, Z. X. Shen, P. Chen, C.-T. Lim, J. T.-L. Thong, and C.-H. Sow. "Controlled Growth and Field-Emission Properties of Cobalt Oxide Nanowalls." Advanced Materials 17, no. 13 (2005): 1595–99. https://doi.org/10.1002/adma.200500322.

[2] Dong, Zhao, Yunyi Fu, Qin Han, Yingying Xu, and Han Zhang. "Synthesis and Physical Properties of Co_3O_4 Nanowires." The Journal of Physical Chemistry C 111, no. 50 (2007): 18475–78. https://doi.org/10.1021/jp075365l.

[3] Kalinic, B., L. Girardi, P. Ragonese, A. Faramawy, G. Mattei, M. Frasconi, R. Baretta, et al. "Diffusion-Driven Formation of CO." Applied Surface Science 596 (2022): 153552. https://doi.org/10.1016/j.apsusc.2022.153552.

[4] Qiao, Zhiqiang, Daguo Xu, Fude Nie, Guangcheng Yang, and Kaili Zhang. "Controlled Facile Synthesis, Growth Mechanism, and Exothermic Properties of Large-Area Co_3O_4 Nanowalls and Nanowires on Silicon Substrates." Journal of Applied Physics 112, no. 1 (2012): 014310. https://doi.org/10.1063/1.4731798.

[5] Xing, Y.J, Q.L Hang, H.F Yan, H.Y Pan, J Xu, D.P Yu, Z.H Xi, Z.Q Xue, and S.Q Feng. "Solid–Liquid–Solid (SLS) Growth of Coaxial Nanocables: Silicon Carbide Sheathed with Silicon Oxide." Chemical Physics Letters 345, no. 1-2 (2001): 29–32. https://doi.org/10.1016/s0009-2614(01)00768-0.

[6] Kalinic, B., L. Girardi, P. Ragonese, A. Faramawy, G. Mattei, M. Frasconi, R. Baretta, et al. "Diffusion-Driven Formation of CO." Applied Surface Science 596 (2022): 153552. https://doi.org/10.1016/j.apsusc.2022.153552.

[7] Li, Yuan, Kassandra Keith, and Nitin Chopra. "Structural and Morphological Evolution of Free-Standing co3o4 Nanowires via Water Vapor-Assisted Thermal Oxidation of CO Foil." Journal of Alloys and Compounds 703 (2017): 414–23. https://doi.org/10.1016/j.jallcom.2017.02.004.

[8] Gulbransen, Earl A., and Kenneth F. Andrew. "The Kinetics of the Oxidation of Cobalt." Journal of The Electrochemical Society 98, no. 6 (1951): 241. https://doi.org/10.1149/1.2778139.

[9] Strawbridge, Anna, and Robert A. Rapp. "The Role of Reactive Elements on Scale Growth in High-Temperature Oxidation of Pure Nickel, Iron, Cobalt, and Copper: I . Oxidation Kinetics and Scale Morphology." Journal of The Electrochemical Society 141, no. 7 (1994): 1905–15. https://doi.org/10.1149/1.2055025.

[10] Yuan, Lu, Yiqian Wang, Rediola Mema, and Guangwen Zhou. "Driving Force and Growth Mechanism for Spontaneous Oxide Nanowire Formation during the Thermal Oxidation of Metals." Acta Materialia 59, no. 6 (2011): 2491–2500. https://doi.org/10.1016/j.actamat.2010.12.052.

[11] Yuan, Lu, Yiqian Wang, Rongsheng Cai, Qike Jiang, Jianbo Wang, Boquan Li, Anju Sharma, and Guangwen Zhou. "The Origin of Hematite Nanowire Growth during the Thermal Oxidation of Iron." Materials Science and Engineering: B 177, no. 3 (2012): 327–36. https://doi.org/10.1016/j.mseb.2011.12.034.

[12] Mema, Rediola, Lu Yuan, Qingtian Du, Yiqian Wang, and Guangwen Zhou. "Effect of Surface Stresses on CUO Nanowire Growth in the Thermal Oxidation of Copper." Chemical Physics Letters 512, no. 1-3 (2011): 87–91. https://doi.org/10.1016/j.cplett.2011.07.012.

[13] Chen, Mingji, Yumei Yue, and Yang Ju. "Growth of Metal and Metal Oxide Nanowires Driven by the Stress-Induced Migration." Journal of Applied Physics 111, no. 10 (2012): 104305. https://doi.org/10.1063/1.4718436.

[14] Li, Yuan, Kassandra Keith, and Nitin Chopra. “Structural and Morphological Evolution of Free-Standing co3o4 Nanowires via Water Vapor-Assisted Thermal Oxidation of CO Foil.” Journal of Alloys and Compounds 703 (2017): 414–23. https://doi.org/10.1016/j.jallcom.2017.02.004.

[15] Zhao, Zhenhuan, Jian Tian, Yuanhua Sang, Andreu Cabot, and Hong Liu. “Structure, Synthesis, and Applications of Tio2Nanobelts.” Advanced Materials 27, no. 16 (2015): 2557–82. https://doi.org/10.1002/adma.201405589.

[16] Li, Cao, Zheng, Alshehri, Alghamidi, Alzahrani et al., Synthesis of Mesoporous TiO2-B Nanobelts with Highly Crystalized Walls toward Efficient H2 Evolution, Nanomaterials. 9 (2019) 919. doi:10.3390/nano9070919.

[17] O. Otieno, E. Csáki, O. Kéri, L. Simon, I. Lukács, K. Szécsényi et al., Synthesis of TiO2 nanofibers by electrospinning using water-soluble Ti-precursor, Journal of Thermal Analysis And Calorimetry. 139 (2019) 57-66. doi:10.1007/s10973-019-08398-z.

[18] H. Liu, D. Yang, E. Waclawik, X. Ke, Z. Zheng, H. Zhu et al., A Raman spectroscopic study on the active site of sodium cations in the structure of Na2Ti3O7during the adsorption of Sr^{2+} and Ba^{2+} cations, Journal of Raman Spectroscopy. 41 (2010) 1792-1796. doi:10.1002/jrs.2634.

[19] Kolen'ko, Yury V., Kirill A. Kovnir, Anton I. Gavrilov, Alexei V. Garshev, Johannes Frantti, Oleg I. Lebedev, Bulat R. Churagulov, Gustaaf Van Tendeloo, and Masahiro Yoshimura. “Hydrothermal Synthesis and Characterization of Nanorods of Various Titanates and Titanium Dioxide.” The Journal of Physical Chemistry B 110, no. 9 (2006): 4030–38. https://doi.org/10.1021/jp055687u.

[20] H. Zhu, Z. Zheng, X. Gao, Y. Huang, Z. Yan, J. Zou, H. Yin, Q. Zou, S. H. Kable, J. Zhao, Y. Xi, W. N. Martens, and R. L. Frost,Structural Evolution in a Hydrothermal Reaction between Nb_2O_5 and NaOH Solution: From Nb2O5 Grains to Microporous $Na_2Nb_2O_6$,2/3H_2O Fibers and NaNbO3 Cubes, Jacs, no. 8, (2006) 2373–2384. https://doi.org/10.1021/ja056301w

CHAPTER 4

Results and discussion

4.0 Background

The following section presents the results of a comprehensive experimental study that was conducted to investigate a specific phenomenon or answer a set of research questions. The experiment was designed and executed with strict protocols to ensure accurate and reliable results. The results of this study provide valuable insights into the properties of these sensors and their potential for practical applications. The following section will thoroughly analyze the results, discuss their implications, and highlight their contribution to the field of MOXs gas sensors.

4.1 Co_3O_4/ZnO composite nanowires for acetone sensing

4.1.1 Material analysis

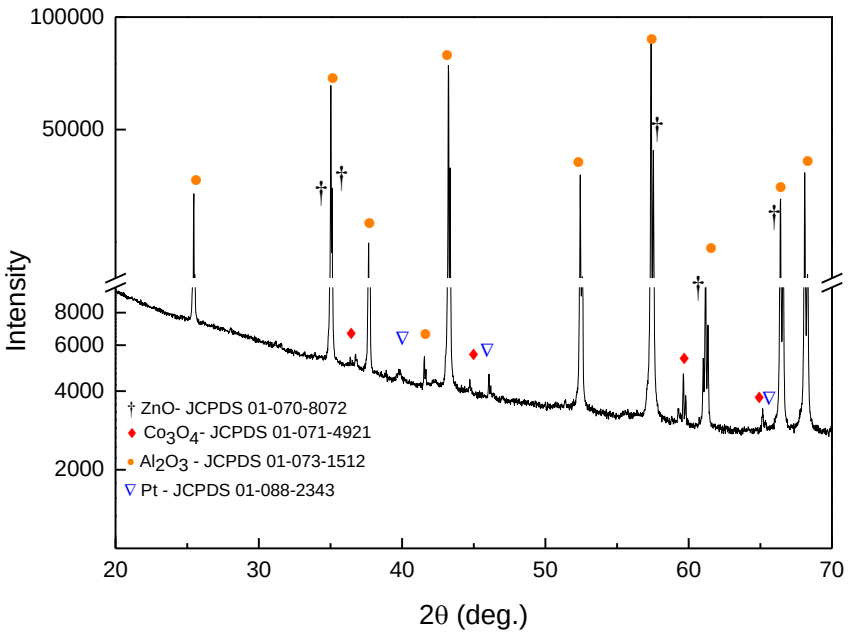

Figure 4.1. X-ray diffractogram of the prepared ZnO/Co_3O_4.

The X-ray diffraction (XRD) pattern in Figure 4.1 shows the reflection peaks that confirm the presence of ZnO and Co_3O_4 in the material being studied. The peaks at two theta values of

34.4°, 36.2°, 56.6°, 62.8°, and 67.9° belong to the (002), (101), (110), (103), and (112) reflection planes of wurtzite ZnO (JCPDS 01-070-8072), while the peaks at two theta values of 36.9°, 44.9°, 59.5°, and 65.5° are attributed to the (113), (004), (115), and (044) reflection planes of cubic Co_3O_4 (JCPDS 01-071-4921) [1,2]. Additionally, the presence of peaks at two theta values of 39.3°, 45.6°, and 66.5°, which belong to the (111), (002), and (022) reflection planes of Pt (JCPDS 01-088-2343), are also observed next to the reflection planes of the Al_2O_3 substrate (JCPDS 01-073-1512).

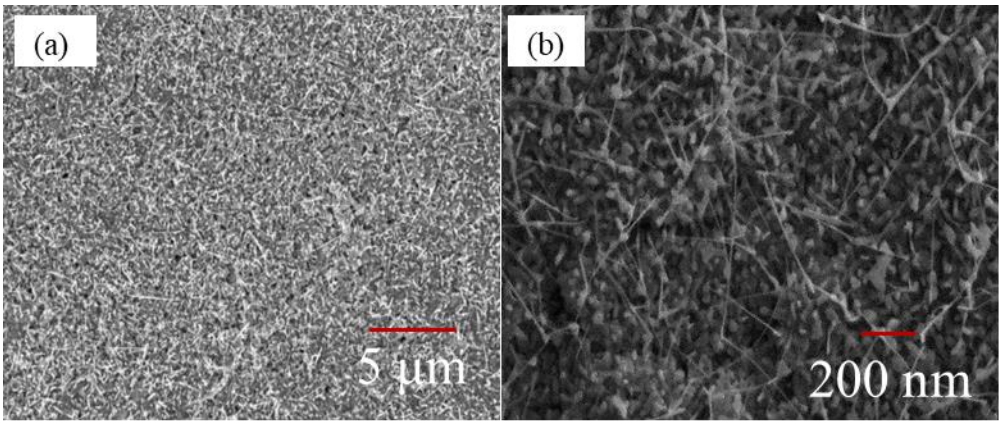

Figure 4.2. Field emission microscope image of the prepared Co_3O_4/ZnO nanowires (a) low magnification, and (b) higher magnification.

The low-magnified FE-SEM image in Figure 4.2 (a) shows the presence of Co_3O_4/ZnO nanowires in a large area, but it is difficult to observe their detailed morphology. However, Figure 4.2 (b) shows the existence of nanowires with various aspect ratios, with an estimated length range of 0.5-2.0 µm and a diameter of 30-50 nm. Notably, the image shows some nanowires crossing over each other. These overlapping and bridge nanowires significantly impact the Schottky junctions and space charge region, contributing to the sensor response [3,4].

The STEM image in Figure 4.3 (a) shows a Co_3O_4/ZnO nanowire, while Figure 4.3 (b) shows the corresponding EDX spectra of the nanowire from its tip to the root. The nanowire composition shows evidence of the elements Zn, Co, Pt, and O, and no impurities have been revealed. The EDX element maps in Figure 4. 3 (c-f) confirm the uneven distribution of these elements in the composite. The body is mostly Zn, resulting in a ZnO structure (Figure 4.3 (d)) while the tip of the nanowire is composed mainly of Pt (Figure 4.3 (f)). Additionally, Co

elements are present in the middle of the nanowire (Figure 4.3(c)), which could be due to the diffusion of a gradient in Co composition along the nanowire, resulting in the formation of a Co_3O_4/ZnO composite.

The EDX mapping near the tip of the nanowire in the dotted rectangular area of Figure 4.3 (a) is shown in Figure 4.4, it confirms that the tip of the nanowire is rich in Pt and Co, resulting in Co_3O_4 underneath the Pt. These results help identify the correct constituting elements at the tip of the nanowire, which is important for understanding the gas sensing mechanism. The synergistic catalytic activity (Pt and Co_3O_4) of the prepared material could enhance the sensing performance of the sensors. Moreover, the presence of "heads" on the tips of each nanowire is justified to be the catalytic Pt nanoclusters followed by Co_3O_4 by EDX mapping. The presence of Pt nanoparticles and the Co_3O_4 at the tip of the nanowire would contribute to higher gas sensing performances ascribed to spill-over and chemical sensitization [3, 5].

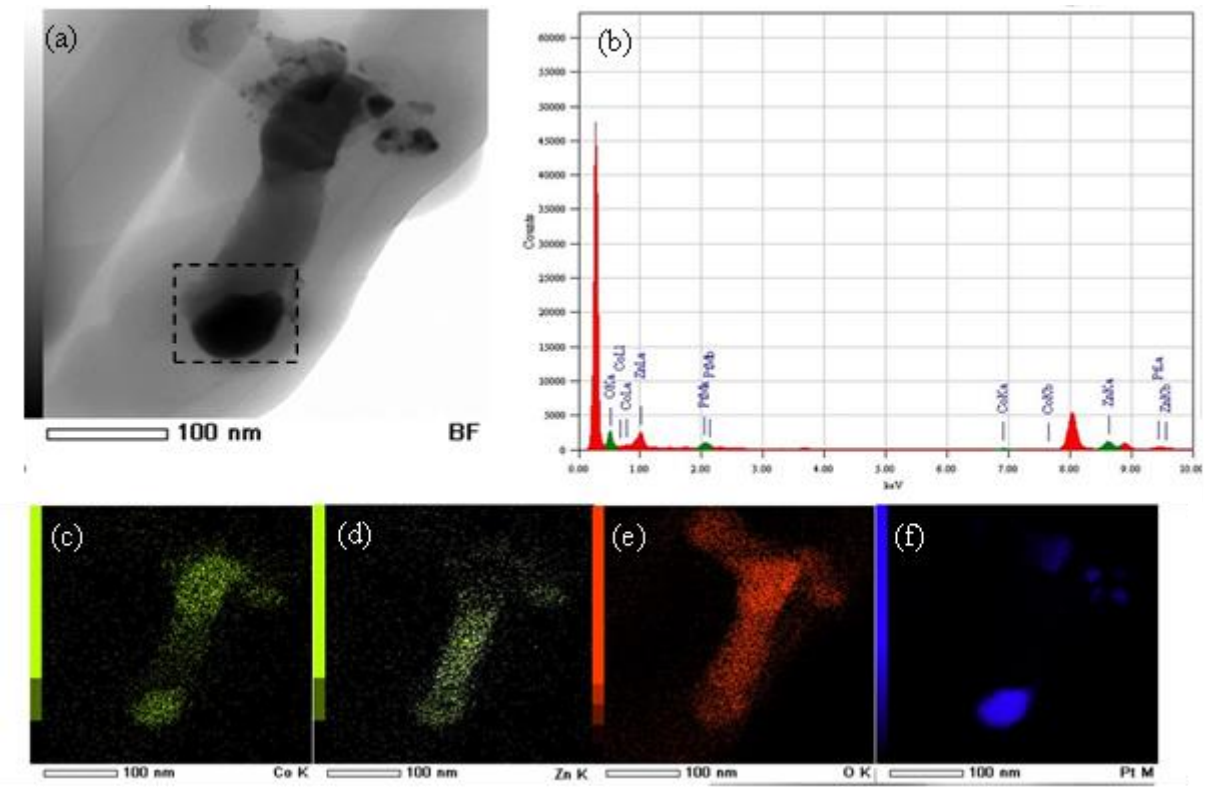

Figure 4.3. Scanning transmission electron microscopy (STEM) image of (a) a single Co_3O_4/ZnO nanowire; (b) Corresponding EDX spectra of the nanowire; elemental mapping of the composite (c) Co (d) Zn, (e) O, and (f) Pt.

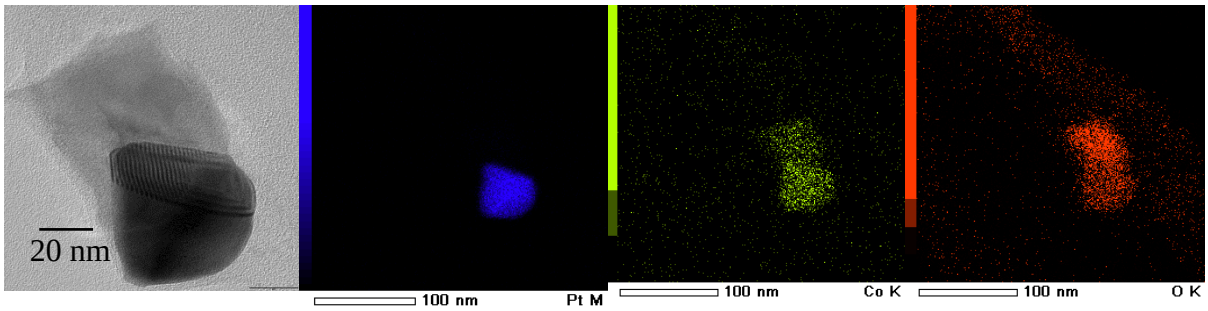

Figure 4.4. EDX mapping of the constituent elements near the tip of the Co_3O_4/ZnO composite nanowire. (a) conventional TEM, (b) mapping of Pt, (c) mapping of Co and (d) mapping of O.

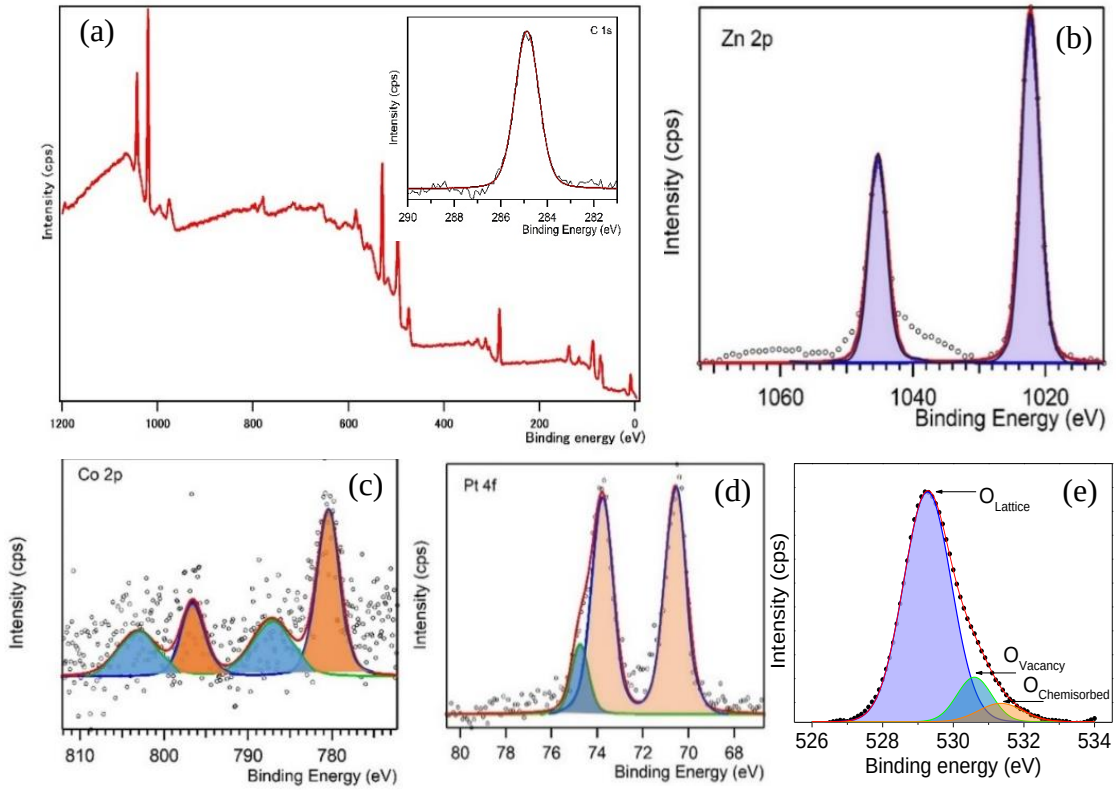

Figure 4.5. X-ray photoelectron spectroscopy (a) full spectrum, the spectrum of (b) Zn; (c) Co; (d) Pt, and (e) O.

The X-ray photoelectron spectroscopy (XPS) survey spectrum of the prepared Co_3O_4/ZnO nanowires confirms the presence of elements Co, Zn, Pt, and O, as seen in Figure 4.5 (a). The high-resolution XPS spectra in Figure 4.5 (b-e) further support the purity of the nanowires, as they are composed of only the elements identified in the energy-dispersive X-ray (EDX) analysis. The C 1S peak at 285 eV is used as the calibration for the XPS spectrum, as shown

in the inset of Figure 4.5 (a). The high-resolution spectra reveal two peaks in the binding energy corresponding to Zn (2P) at 1045.2 eV ($2p_{3/2}$) and 1022.1 eV ($2p_{1/2}$) in Figure 4.5 (b). These peaks are typically found at 1044.62 eV ($2p_{3/2}$) and 1021.69 eV ($2p_{1/2}$) for pure ZnO. The shift in the binding energy observed in Figure 4.5 (b) is likely due to the formation of Co_3O_4/ZnO, as Co has a higher electronegativity than Zn. Figure 4.5 (c) shows Co peaks at 780.39 eV and 796.19 eV, corresponding to Co $2p_{3/2}$ and Co $2p_{1/2}$, respectively, which are known to originate from Co 2p of Co_3O_4 [6,7]. Additionally, distinct satellite peaks near Co $2p_{1/2}$ (804.18 eV) and Co $2p_{3/2}$ (787.39 eV) suggest the presence of oxygen vacancies in Co_3O_4 [8]. Figure 4.5 (d) shows two peaks at 70.5 eV and 73.7 eV, suggesting the presence of metallic Pt [9]. The O 1s spectra in Figure 4.5 (e) shows three Gaussian peaks, indicating the presence of oxygen lattice, oxygen vacancies, and chemisorbed oxygen. The existence of oxygen vacancies in the nanowires is believed to contribute to the excellent sensing performance of the sensor at low working temperatures [10,11].

4.1.2 Gas sensing analysis

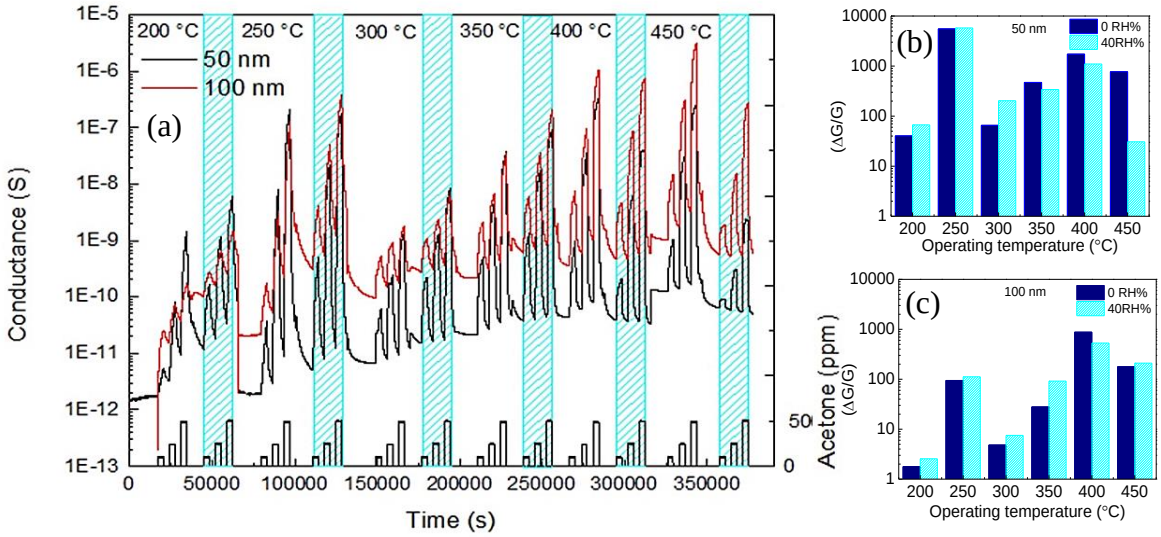

Figure 4.6. Gas sensing performances (a) Dynamic response of the Co_3O_4/ZnO sensors at both dry and 40 RH% air (light blue pattern area), (b) response value of the sensors towards 50 ppm acetone having initial Co thickness of 50 nm, and (c) 100 nm in the working temperature 200-450 °C.

A series of experiments was conducted to determine the optimal working temperature of the sensor. Prior to gas sensing evaluation, the prepared Co_3O_4/ZnO nanocomposite sensors were thermally aged at 400 °C for 48 hours in air. Figure 4.6 (a) illustrates the dynamic response of the sensors to 10, 25, and 50 ppm of acetone (C_3H_6O) at working temperatures ranging from 200-450 °C in both dry and humid air conditions (40% relative humidity). It is observed that the electrical conductance of all sensors increases with increasing temperature, typical behavior of metal oxide semiconductors. The variation of electrical conductance with air and reducing gas (C_3H_6O) clearly shows the n-type conductivity of grown nanowires [12]. Such n-type behavior is ascribed to the relatively high content of the constituting compound ZnO compared to that of Co_3O_4.

The sensors demonstrated a strong response to all concentrations of C_3H_6O at evaluated temperatures. As the concentration of C_3H_6O increased, the sensors' conductance also increased due to more molecules adsorbing onto the surface. Figure 4.6 (b, c) illustrates the response of sensors with initial Co layer thicknesses of 50 and 100 nm to 50 ppm of C_3H_6O. The sensors with 50 nm Co layers had a stronger response than those with 100 nm layers at all tested temperatures. This could be due to the higher density of nanowires in the 50 nm thick sample [13,14]. The sensors with a 100 nm thick Co layer have a lower resistance, resulting in faster recombination of charge carriers compared to the 50 nm thick layer. This leads to fewer gas molecules adsorbing onto the surface, resulting in a decreased response in the 100 nm thick Co sensor [15]. The sensor with a higher response is selected for further discussion. From now on, the term "sensors" refers to the sensors with an initial Co thickness of 50 nm (higher density of nanowires). The sensors' response increases as the working temperature increases before decreasing at 450 °C, which is typical behavior for metal oxide gas sensors and is attributed to the dynamics of the gas. At lower working temperatures, adsorption, desorption, and reactions are less active and gas adsorption is not efficient when the working temperature is too high, which negatively impacts the sensor performance [16].

The decrease in response at 450 °C could be caused by the combustion of C_3H_6O with lattice oxygen, which results in damage to the crystal structure. Additionally, a particularly high response is observed at a working temperature of 250 °C (Figure 4.6 (b, c)). This could be due to a combination of factors such as spill-over, chemical sensitization, and synergistic gas adsorption and catalytic properties of the nanowires, as described in the sensing mechanism. Sensors operating at low working temperatures have the benefits of low energy consumption, stability, increased safety, and portability. Figure 4.7 (a) shows the dynamic response of the

sensors to C_3H_6O concentrations of 10, 25, and 50 ppm at 250 °C. The response and recovery data have similar shapes, and the baseline value was not reached within the obtained time cycle. Figure 4. 7 (b) shows the dynamic response of the sensor at 400 °C, where the second-highest response was observed. The sensors still have a curvy shape at 400 °C, but they recover well to the baseline conductivity when operating at 40% relative humidity, which is a practical application.

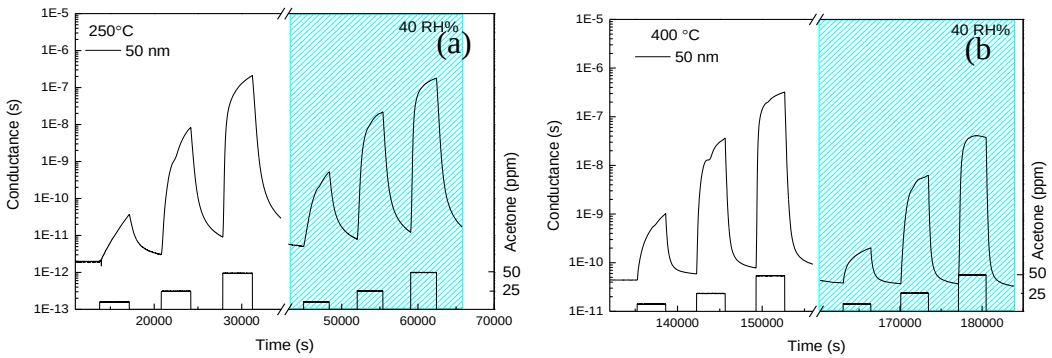

Figure 4.7. Dynamic response of the Co_3O_4/ZnO sensors at the working temperature of (a) 250 °C and (b) 400 °C both at dry and 40 RH% air conditions.

In practical applications, response and recovery time are just as important as response value when it comes to assessing the performance of sensors. The response time is not significantly affected by temperature in both dry and humid air, but recovery time varies significantly with working temperature (Figure 4.8). It is worth noting that the recovery of the response is slower than the response time. This could be due to the accumulation of byproducts on the sensor surface because of incomplete combustion of C_3H_6O. Based on these results, the optimal working temperature for C_3H_6O gas sensing using the Co_3O_4/ZnO composite is 400 °C. The corresponding response and recovery times are listed in Table 4.1 with a comparison of reported Co_3O_4/ZnO composites.

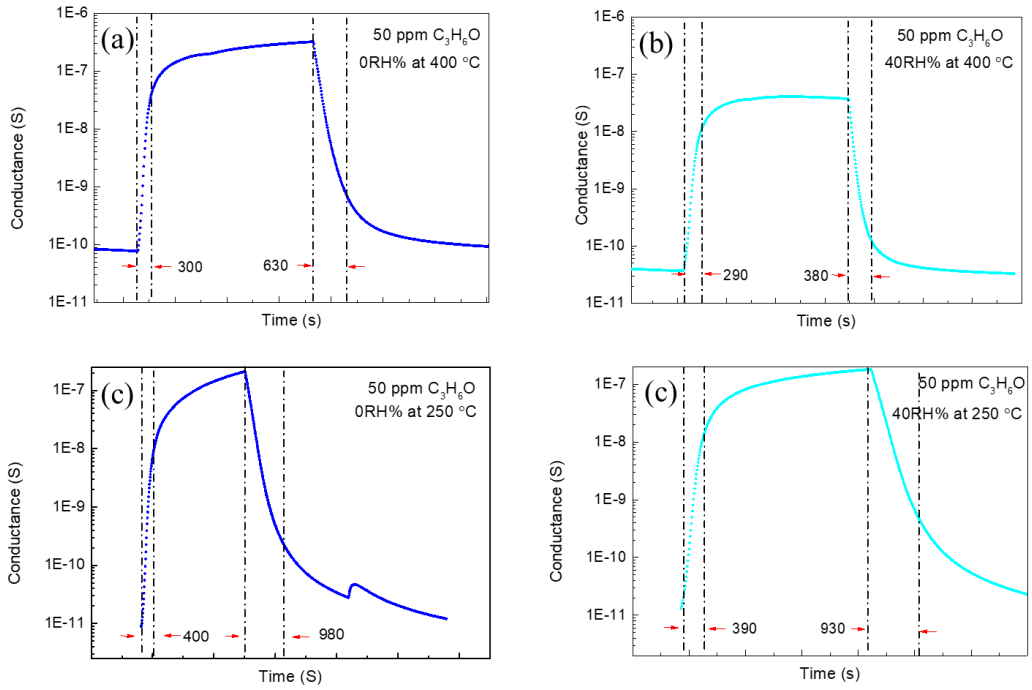

Figure 4.8. Response and recovery time of Co_3O_4/ZnO nanowires having a higher density of nanowires at (a) 400 °C, 0RH%, (b) 400 °C, 40RH%, (c) (a) 250 °C, 0RH%, (b) 250 °C, 40RH%.

Table 4.1. Comparison of the sensing performance of different Co_3O_4-ZnO related sensors for acetone sensing.

Material	Structure	Temp. (°C)	Gas Acetone (ppm)	Response	Response/ recovery time (s)	LOD (ppb)	Long-term stability / Reproducibility	Ref
Pd@Co_3O_4-ZnO	Nanofibers	240	200	44.9	16/13	1000	NA/180 Days	[17]
Co_3O_4–ZnO	Hetero-junction composite	290	100	113.8	24/18	500	5 cycles/30 days	[18]
Au @ ZnO	Porous tube	190	50	115	3/74	NA	NA/6 cycles	[19]
MOF ZnO/ Co_3O_4	Hetero-structure	300	100	30.01	8/2		30 day/ 5 cycles	[20]
Co_3O_4/ZnO	Nano-composite	180	100	63.7	N/A	200	11 cycles/10 weeks	[21]
Co_3O_4/ZnO	Nanowires	250	50	5780	390/930	400	3 cycles/3 weeks	This work
		400		3572	290/380	500		

*All the reported response values were calculated (R_{air}/R_{gas}) except reporting working in ($\Delta G/G$).

The sensors' calibration curves for C_3H_6O are plotted using a modified power law equation (Figure 4.9), $y = ax^b$, where '*a*' represents sensitivity and '*b*' represents the surface reaction between the target gas and the dominant oxygen species at the working temperature [22]. The fitting of the data to the power law relation is admirable, with correlation coefficients (R^2) of at least 0.94. The detection limit is determined by extrapolating the lowest detection limit to an acceptable response value ($\Delta G/G=0.1$) using the power law relation. The sensitivity (the slope of the power law fitting curve) and the detection limit are shown in (Table 4.2).

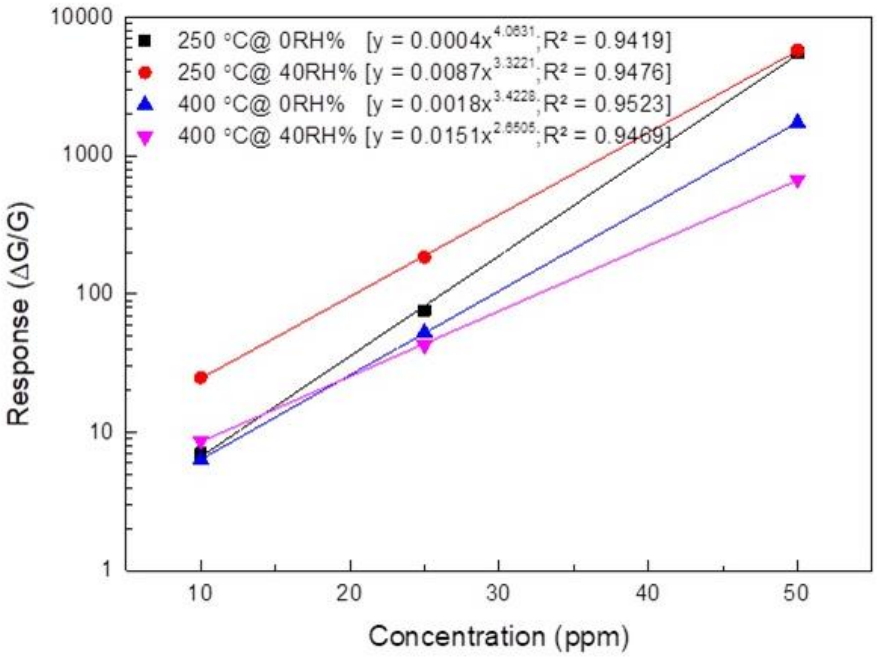

Figure 4.9. Power fitting of the Co_3O_4/ZnO sensors at the working temperature of 205 and 400 °C.

Table 4.2. Sensitivity and the detection limit of the Co_3O_4/ZnO sensors.

Sensors working condition	LOD (ppm)	Sensitivity (ppm^{-1})
250 0RH%	0.7	4.0×10^{-4}
250 40RH%	0.4	8.7×10^{-3}
400 0RH%	0.6	1.8×10^{-3}
400 40RH%	0.4	1.5×10^{-2}

The selectivity of the sensors towards other gases, such as C_2H_5OH, H_2S, NH_3, CO, NO_2, and H_2, was also evaluated (Figure 4.10). As seen in Figure 4.11 (a), the sensors display

exceptional selectivity for C_3H_6O when operated at the optimal temperature. The high response of the sensors to C_3H_6O compared to other gases may be due to the relatively low bond dissociation energy of C_3H_6O compared to other gases such as NH_3, H_2S, H_2, CO, and NO_2. The exact reason is not yet fully understood [23] and relatively low bond strength in C-C bond in C_3H_6O (345 KJ/mol) compared to O-H (462 kJ/mol) of C_2H_5OH (the most significant for the interactions with the adsorbed oxygen species) [24]. As a consequence, C_3H_6O molecules are being easily adsorbed and reacted on the surface of the sensors in contrast to other investigated gases and VOCs, leading to an excessive release of electrons that increases the electrical conductance of the sensor. In addition, morphology, materials compositions, gas adsorption capacity, different reaction processes including catalytic activity, and consumed number of chemisorbed oxygen species of different tested gas molecules are contributing to the selectivity of the gas sensor [17,25].

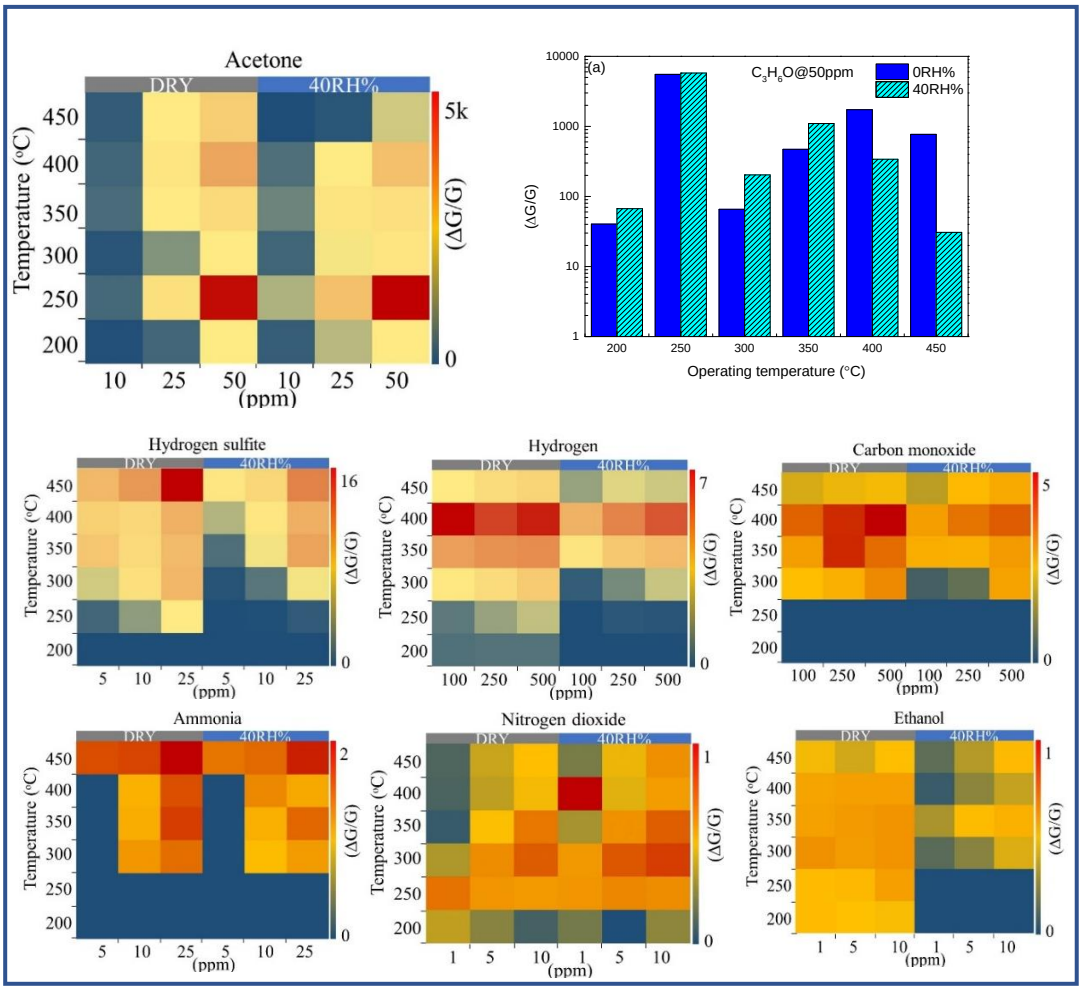

Figure 4.10. The selectivity performance of the Co_3O_4/ZnO sensors.

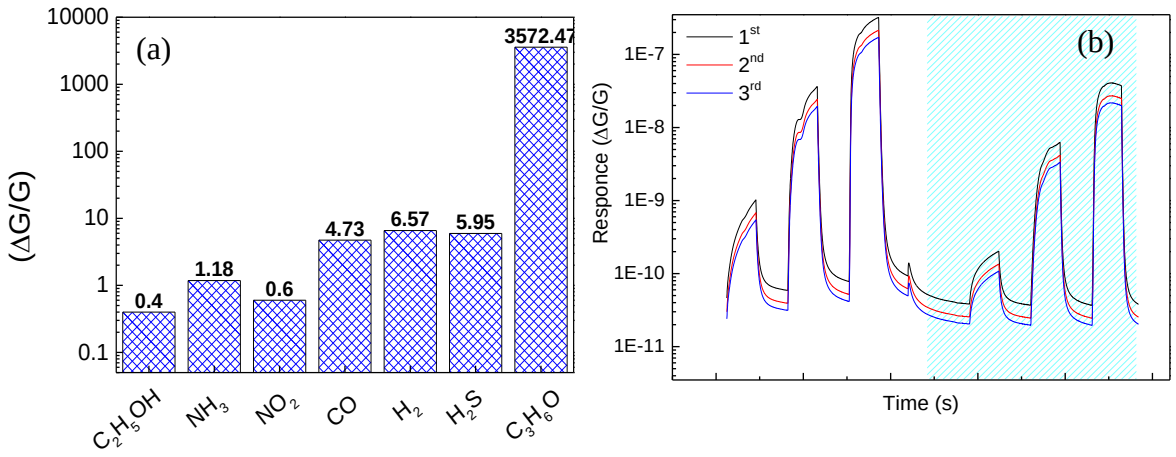

Figure 4.11. (a) selectivity; (b) repeatability of the Co_3O_4/ZnO sensors for three consecutive cycles when working at the optimum working temperature of 400 °C.

The repeatability and stability of the sensor are important considerations for commercialization. To evaluate these properties, tests were conducted using three consecutive cycles of 10, 25, and 50 ppm C_3H_6O in both dry air and 40% relative humidity air, at the optimum working temperature of 400 °C. The results, shown in Figure 4.11 (b), demonstrate the sensor's good repeatability, with similar response values and a return to baseline when the air flow is restored. Additionally, the stability of the sensor over a three-week period was evaluated. The sensor displayed considerable stability, with a response variation about 10% after three weeks.

4.1.3 Working mechanism

Based on the EDX mapping and electrical conducting type, the following hypothesis is suggested as shown in Figure 4.12 (a) in which the main sensing material is ZnO. A thin depletion layer forms on the surface due to surface states, resulting in minimal band bending at the surface. The gas sensing mechanism is likely due to the chemisorption of oxygen molecules on the ZnO surface, which traps electrons in the conduction band when the nanowires are exposed to air [18]. It is hypothesized that the main sensing element in the system, n-type metal oxide (ZnO), chemisorbs more oxygen to compensate for its deficiencies. However, the surface oxygen concentration on the transitional p-type (Co_3O_4) is significantly higher compared to that of n-type metal oxides. At temperatures below 150 °C, the adsorbed oxygen molecules form molecular O_2^-. At temperatures between 150-400 °C,

atomic O^- species are formed and at temperatures above 400 °C, O^{2-} species are formed by trapping electrons from the conduction band of the ZnO. This study focuses on the O^- species which is highly active in this range of tested temperatures. As a result, the depletion layer on the ZnO nanowires thickens. When the nanowires are exposed to C_3H_6O, the analyte gas reacts with the oxygen species present on the surface, leading to a reduction in the gas into CO_2 and H_2O, and releasing electrons back into the conduction band of the ZnO, as shown in Equations (4.1) and (4.2) [19,20]. The high response in the sensors may not be solely due to the simple sensing mechanism outlined previously. Additional factors, such as electron/chemical sensitization effects, the formation of p-n heterojunctions (Co_3O_4-ZnO), and the synergistic effect of Co_3O_4, may also contribute to the exceptional response observed.

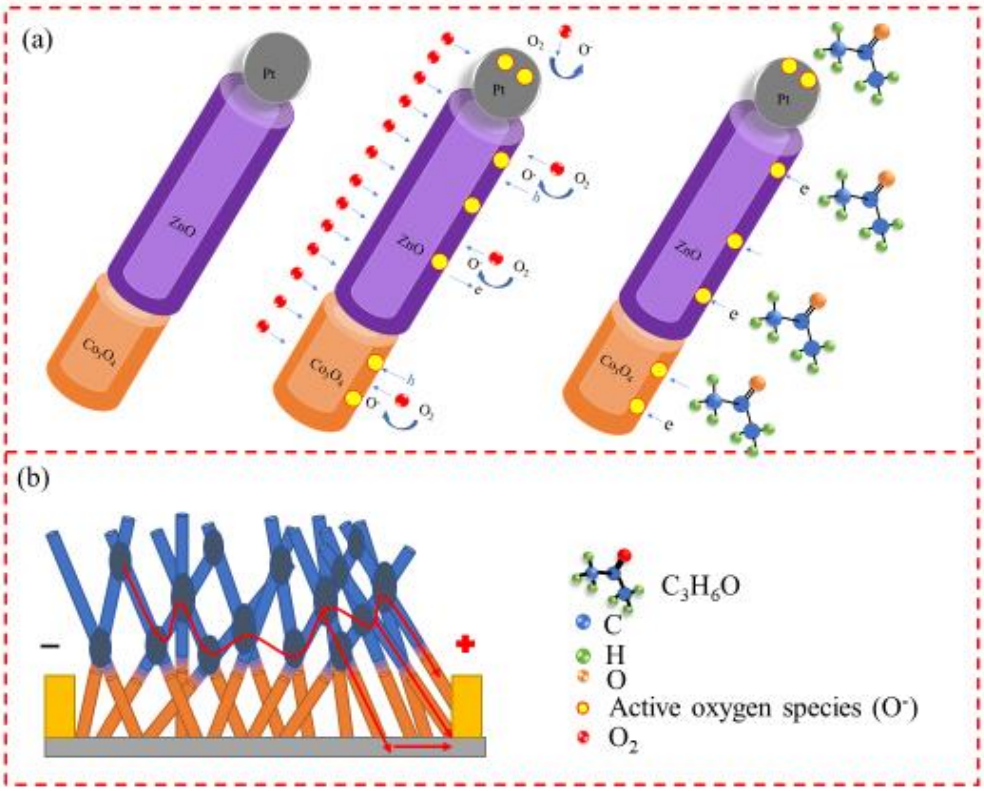

Figure 4.12. Schematic of the proposed (a) Co_3O_4/ZnO nanostructure; (b) the charge transfer path.

The formation of a n-p heterojunction between ZnO (n-type) and Co_3O_4 (p-type) in the composite material is a key factor in the high response observed in the sensors. The difference in work function between the two materials, with ZnO having a lower work function of 4.65 eV compared to Co_3O_4's 4.8 eV, likely plays a role in this effect [19,21]. As

a result of the preparation process, each ZnO (n-type) nanowire meets Co_3O_4 (p-type) creating n-p heterojunctions at the base of the nanowire. The higher work function of ZnO compared to that of Co_3O_4, causes electrons to transfer from the conduction band of ZnO to the valence band of Co_3O_4 and become trapped in Co_3O_4. This leads to the formation of an additional depletion layer between ZnO and Co_3O_4 at the base. Additionally, the presence of Co_3O_4 within the ZnO nanowire (as seen in Figure 4.3 (c,d))) creates an additional p-n junction inside the nanowire. This results in a drastic increase in band bending and a higher barrier potential, leading to higher resistance in the sensors. Furthermore, the formation of this n-p heterojunction is known to make the sensors more susceptible to attracting oxygen species and C_3H_6O [1, 26]. As a result, C_3H_6O molecules interact with both the holes (p-type Co_3O_4) and oxygen species (n-type ZnO) at the junction interface and produce intermediates (Equations 4.3, 4.4). Also, the formed intermediate interacts with oxygen species as shown in Equations 4.5,4.6 [27,28]. So, the depletion layer thickness of the heterojunction is further thinning resulting in lower barrier potential, in other terms high response. Additionally, Co_3O_4 shows the cubic structure which is in the *Fd-3m* space group and consists of two inequivalent Co^{2+} sites [29]. The Co^{2+} sites in the tetrahedron coordination of Co_3O_4 have a remarkable catalyzing property for oxygen reduction. Thus, Co^{2+} ions are oxidized into Co^{3+} ions when it is in the air which are subsequently reduced into Co^{2+} when interacting with the acetone gas. As a consequence, electrons are transferred promptly between gas molecules and the surface of the sensing material when the sensor is exposed to the gas. Also, Co^{3+} is reduced into Co^{2+} at its surface (in our case), and then Co^{2+} into Co [13]. Thus, both the Co^{2+} and Co^{3+} sites play an important role in the gas sensing process [30]. Accordingly, the catalytic property and the synergistic gas adsorption property of Co_3O_4 are believed to enhance sensor response [31,32]. Also, the oxygen vacancy on the surface of Co_3O_4 improves the adsorption of high dipole gases. Thereby, it is believed the presence of Co_3O_4 at the tip of the nanowire would enhance the gas adsorption hence enhancing the sensitivity toward the C_3H_6O [33,34].

$$1/2O_2(g) + e^- \leftrightarrow O^-(ad) \quad 4.1$$

$$C_3H_6O(g) + 8O^-_{(ion)} \rightarrow 3CO_2(g) + 3H_2O + 16e^- \quad 4.2$$

$$1/2O_2(g) \leftrightarrow O^-(ad) + h^+ \quad 4.3$$

$$C_3H_6O + O^- + h^+ \rightarrow CH_3CO^+ + CH_3O^- \quad 4.4$$

$$CO + h^+ + O^- \rightarrow CO_2 \quad 4.5$$

$$CH_3CO^+ \rightarrow CH^+_3 + CO \qquad 4.6$$

The composite sensor's exceptional performance can be attributed to several factors, including the formation of an n-p heterojunction between ZnO and Co_3O_4, the grain-grain interface contact, and the synergistic effect of Co_3O_4. The n-p heterojunction at the root of the nanowire creates a high resistance, which attracts more oxygen species and C_3H_6O. Additionally, the intercrossing of nanowires results in additional junctions between the overlapping nanowires, leading to a high electron motion and a high response when the sensor is exposed to gas [35]. The exceptional sensing performance of the sensors can also be attributed to the grain-grain interface contact. As seen in Figure 4.2 (b), the intercrossing of the nanowires creates an additional path for electrons to move through, shortening the distance to the electrodes as shown in Figure 4.12 (b). Furthermore, the presence of Pt nanoparticles at the tips of the nanowires forms Schottky junctions, which facilitates the transfer of electrons from the ZnO and Co_3O_4 (with lower work functions of 4.65 eV and 4.8 eV respectively) to the Pt (with a higher work function of 5.64 eV), resulting in a high level of electron negativity in the Pt [36]. As a result, oxygen molecules/atoms are chemisorbed on the surface of the Pt clusters. This could be the reason for the satellite peak in the XPS spectrum of Pt (Figure 4. 4 (d)). Thus, the amount of chemisorbed oxygen species at the sensor surface increases resulting in an enhancement in the sensor response [37].

Furthermore, when the sensor is exposed to the C_3H_6O, the chemical reaction between C_3H_6O and adsorbed oxygen species causes electrons to return to the sensing element surface. This increase in surface electron density raises the Fermi level, making it easier for electrons to overcome the barrier potential. Additionally, the Pt nanoparticles at the tip of the nanowires act as a catalyst, reducing the energy barrier for C_3H_6O adsorption on the sensing element surface and promoting the "spill-over effect." This results in the splitting of incoming C_3H_6O molecules into more active atomic species, which then react with the active sites (O^-) on the sensing surface [38]. Accordingly, the tremendous C_3H_6O sensing response may be ascribed to a higher amount of oxygen species, formation of heterojunction, synergistic catalytic effect, spill-over effect, and the synergistic gas adsorption of Co_3O_4.

4.2 Pt functionalize Co_3O_4 nanowalls for acetone sensing

4.2.1 Material analysis

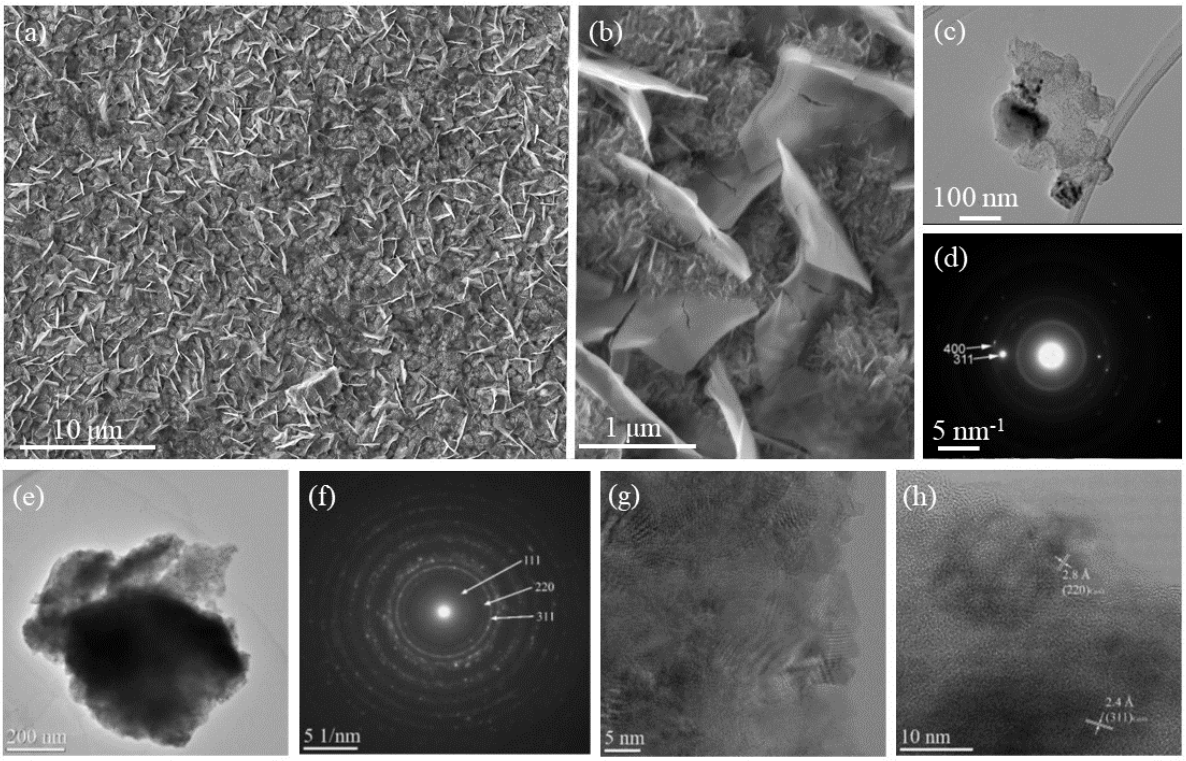

Figure 4.13. FE-SEM of Co_3O_4 (a) low magnification, (b) high magnification, (c) CTEM of Co_3O_4 nano wall, (d) electron diffraction pattern for the HRTEM of Co_3O_4 nanowalls, (e) CTEM of Co_3O_4 nano petals, (f) electron diffraction pattern for the HRTEM of Co_3O_4 nano petals, (g-h) HRTEM of Co_3O_4 nano petals.

FE-SEM images in Figure 4.13 (a) and (b) illustrate the synthesized Co_3O_4, which exhibits nanowalls with small nano petals. Figure 4.13 (c) presents TEM images of a nanowall, and the corresponding electron diffraction pattern in Figure 4.13 (d) confirms the FCC structure of Co_3O_4, with the most prominent diffraction spots being (311) and (400) crystallographic planes. The oxidation process typically starts at the surface of the Co thin film and progresses to the deeper layers of the film. Therefore, we believe that CoO is present in the deeper layers of the film close to the Al_2O_3 substrate. To analyze the composition of the nanostructures, TEM characterization was performed on the nano petals regions (as seen in Figure 4.13 (e)). The electron diffraction pattern in Figure 4.13 (f) corresponding to the image in Figure 4.13 (e) confirms the FCC structure of Co_3O_4 (as per CIF file no. 9005896). The image in Figure

4.13 (f) displays fringes with interplanar distances of 2.4 Å, corresponding to the separation between (311) lattice planes, 2.8 Å, corresponding to the separation between (220) lattice planes, and 4.7 Å, corresponding to the separation between (111) lattice planes. The (111) and (311) lattice planes correspond to CoO, while the (220) lattice plane corresponds to Co_3O_4. Figures 4.13 (g-h) present HRTEM images of Figure 4.13 (e) which show the crystal planes related to CoO and Co_3O_4. Additionally, Figure 4.14's EDX spectra confirm the nanowalls and petals are composed of Co and O without any impurities. Furthermore, Pt nanoparticles can be seen on the surface of the functionalized Co_3O_4 nanowalls in Figure 4.15 (a,b).

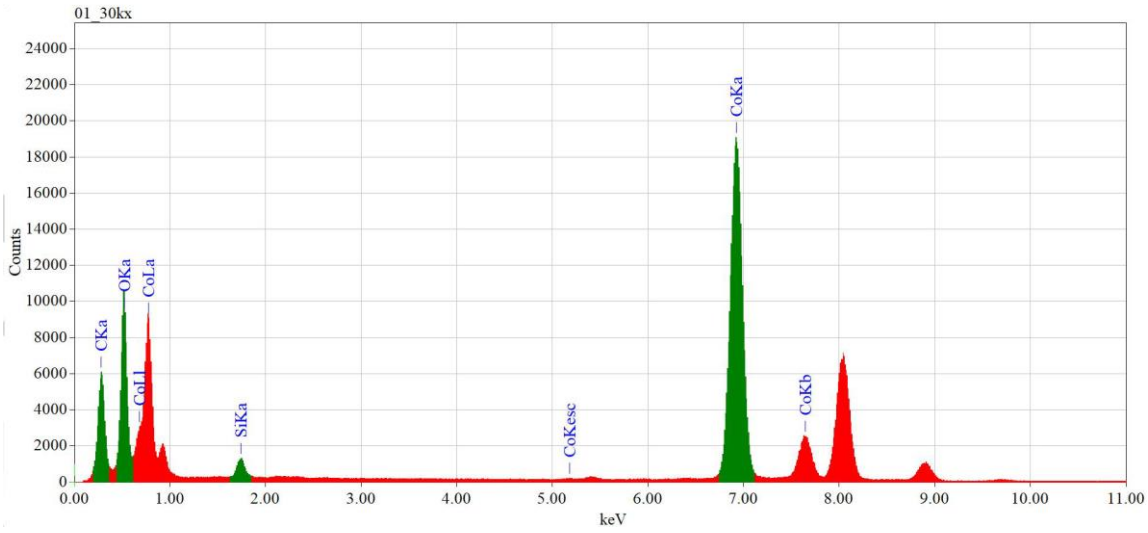

Figure 4.14. EDS spectra of the grown Co_3O_4 nanowalls.

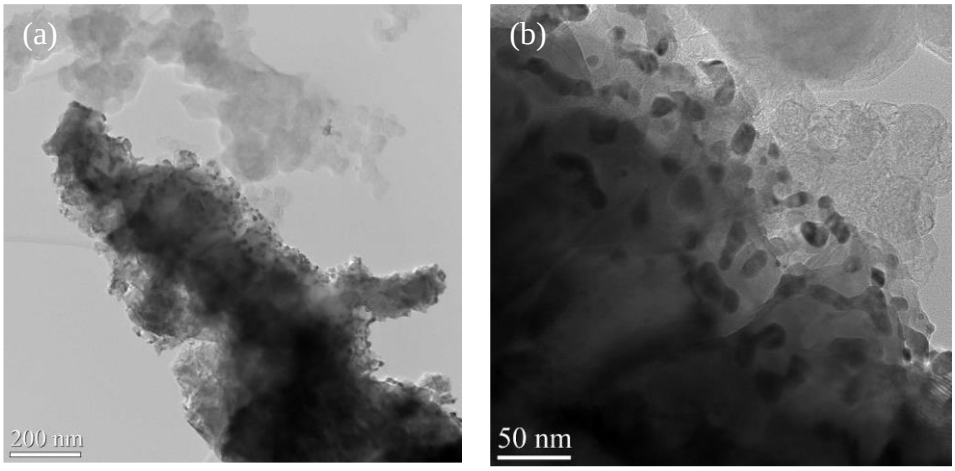

Figure 4.15. TEM image of the Pt functionalized Co_3O_4. The size of these nanoparticles ranges from 4 nm to 18 nm.

Typically, spinel Co_3O_4 exhibits Raman-active vibrations ($A_{1g}+E_g+3F_{2g}$), infrared-active vibrations ($4F_{1U}$), and inactive modes (F_{1g}, $2A_{2U}$, $2E_U$, $2F_{2U}$) in vibrational modes [39]. Figure 4.16 (a) shows the Raman spectra of the as-grown metallic Co sample. The spectra depict only one broader peak at 529.3 cm^{-1}. In general, a broader peak is expected for the metal. Besides, in Figure 4.16 (b), five characteristic peaks at 195, 482, 521, 620, and 692 cm^{-1} are visible which belong to the symmetric phonon modes of $F2g^1$, Eg, $F2g^2$, $F2g^3$ and Ag^1 the crystalline Co_3O_4 respectively [40]. The strongest Raman peak at 193 cm^{-1} is attributed to the tetrahedral sites while the peak at 692 cm^{-1} is attributed to the octahedral sites of spinal Co_3O_4. Additionally, the Co^{3+} ions occupy octahedral sites (16a Wyckoff sites) and Co^{2+} ions occupy tetrahedral sites (8a Wyckoff sites) in the spinal structure of Co_3O_4 [41]. Also, the bands at 193 cm^{-1} and 691 cm^{-1} could be ascribed to Raman vibration of Co^{2+}-O^{2-} and Co^{3+}-O^{2-} respectively [42]. This result confirms the formation of the Co_3O_4 and in which tetrahedral sites are dominant compared to octahedral sites in the prepared structures.

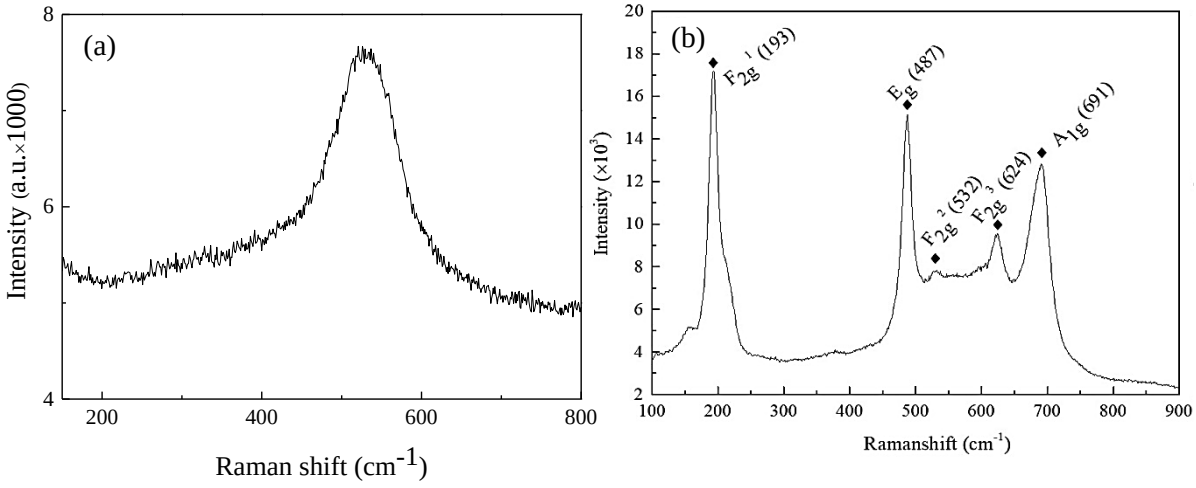

Figure 4.16. Raman spectra of the (a) metallic Co, (b) prepared Co_3O_4 nanowalls.

The EPR spectra of the as prepared Co_3O_4, in both X- and Q-bands (Figure 4.17 (a,b)), consist of a broad and intense line at low magnetic field which strongly decreases in intensity after annealing in air for 8 hours. As the measurement temperature is decreased to 100 K, the line broadens and moves to lower magnetic fields (Figure 4.17 (c,d)), a behavior associated with the presence of a ferromagnetic phase. Room temperature ferromagnetism has been previously observed in CoO nanoparticles and attributed to the presence of oxygen vacancies [43] or uncompensated surface spins [44]. For nanostructured Co_3O_4 ferromagnetic coupling

was detected in samples with exposed (100) and (111) planes and predicted for the interface between Co_3O_4 and CoO [45]. The strong decrease of the spectra intensity after annealing at 400 ^oC could be explained by the transformation of the observed CoO into Co_3O_4 and the decrease of the oxygen vacancies concentration.

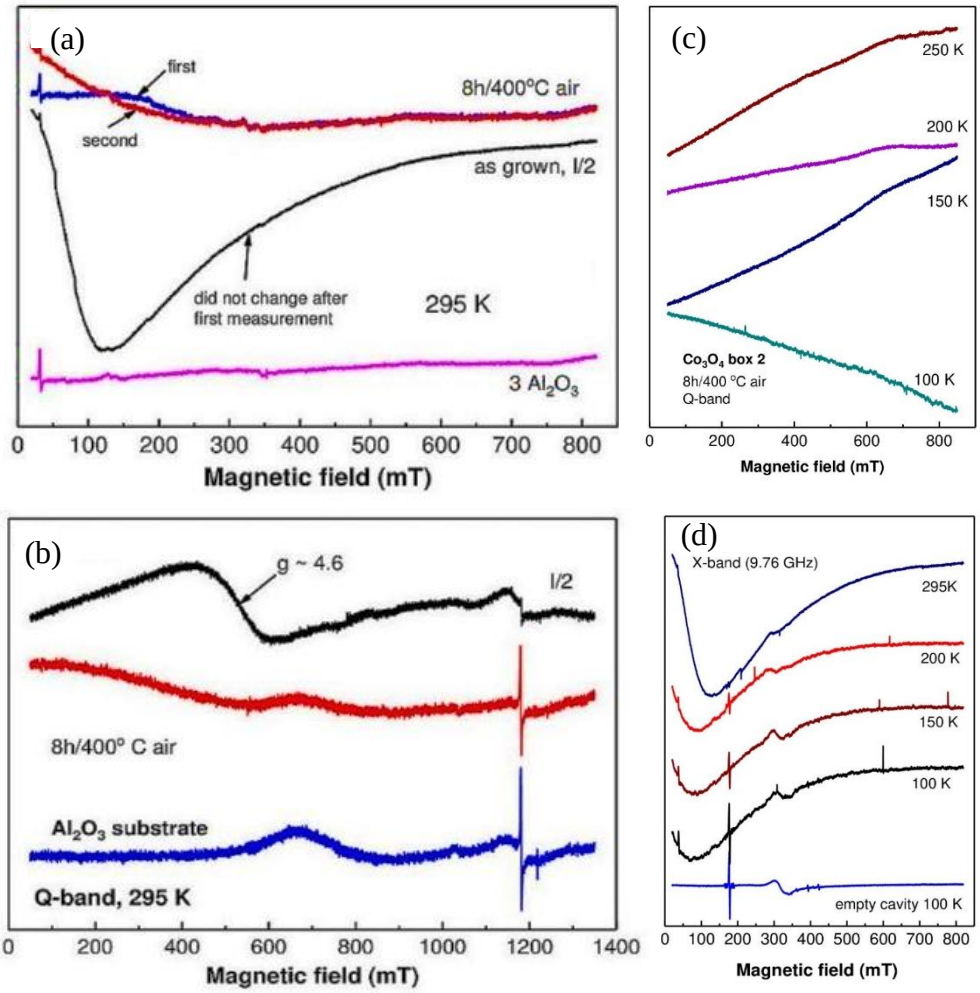

Figure 4.17. EPR measurement of the Co_3O_4 nanowalls X-band (a) before the thermal aging, (b) after thermal aging at 400 °C for 8 hours, Q- band spectra (c) before the thermal aging, (d) after thermal aging at 400 °C for 8 hours.

4.2.2 Gas sensing analysis

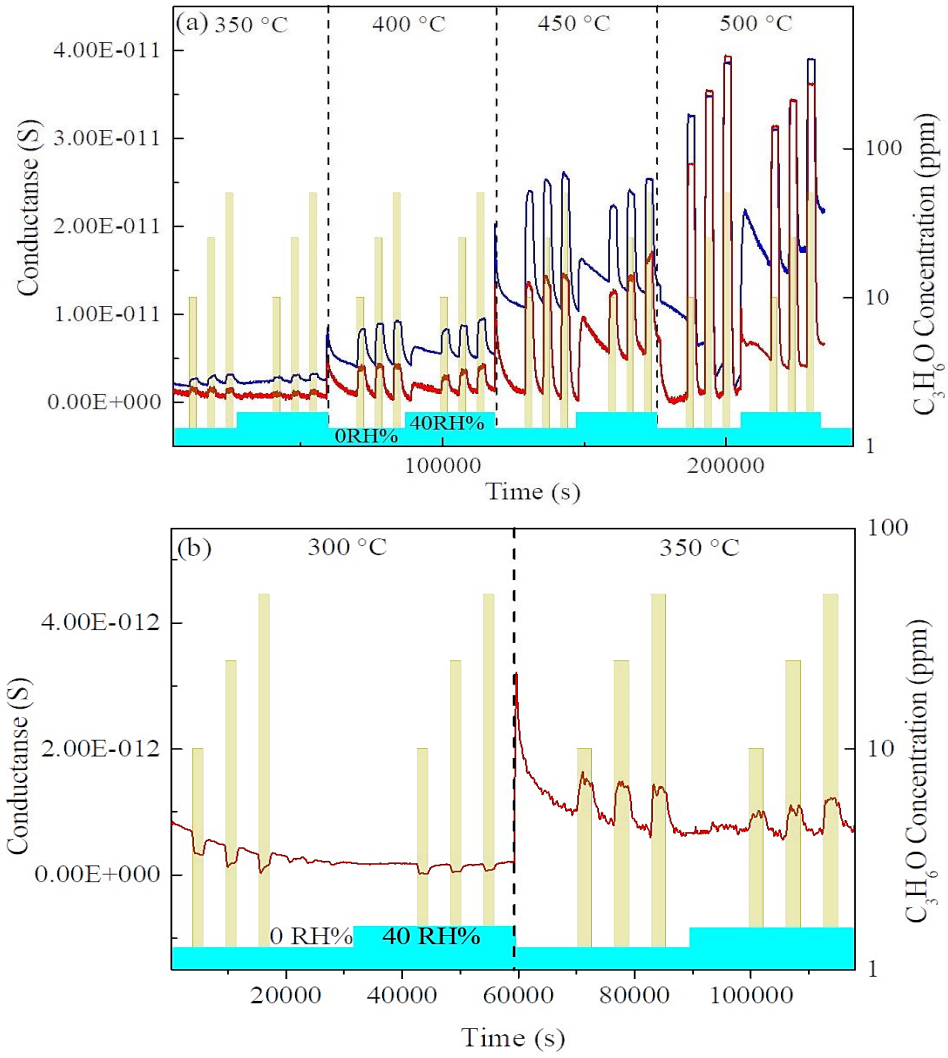

Figure 4.18. (a) Electrical responses of the fabricated Co_3O_4 nanowalls based sensor exposed to different acetone concentrations (10, 25 and 50 ppm) in dry (RH 0%) and humid air (40 RH%) at the range of operating temperature (350 °C, 400 °C, 450 °C and 500 °C). The dark yellow rectangles represent the acetone concentrations. The blue vertical lines divide the graphs, corresponding to different humidity values (0 RH%, 40 RH%), (b) Electrical responses of the fabricated Co_3O_4 nanowalls based sensor exposed to different acetone concentrations (10, 25 and 50 ppm) in dry (RH 0%) and humid atmospheres (40 RH%) at the operating temperatures (300 °C and 350 °C). The graph in red represents the Pt functionalized while graph in blue represents the pristine Co_3O_4.

The conductometry measurements were performed using an initial stabilization step of five hours at each operating temperature while applying a voltage bias of 1V. The device was then exposed to three different concentrations of acetone (10, 25, 50 ppm) in a cycle that lasted 90 minutes, with 30 minutes of exposure to gas followed by 60 minutes of exposure to synthetic air for recovery. The recorded current for both the Pt-functionalized (Pt-Co_3O_4) and the pristine sensors was found to be low. However, the electrical conductance was observed to increase slightly when humidity was introduced and decrease exponentially (Figure 4.18 (a)). This is an unusual n-type behavior for the prepared material, which is typically p-type. However, it is possible for the electrical conductance type to invert from p-n to n-p due to the high operating temperature, humidity, composition, additives (decoration) and reducing species [46-48]. Irrespective to the type of inversion (n-p or p-n) it is fascinating since it is beneficial to understand the sensing mechanism of the MOX. Regarding the Co_3O_4, Vladimirova et. al. has reported the inversion of conductance from p-n at a temperature higher than 250 °C in dry air due to the decomposition of $Co^T - O_2^{2-} - Co^O$ superficial adducts [49]. Additionally, Lin et. al. has reported the inversion of conductance due to the participation of lattice oxygen in the oxidation process [50]. This research found that the electrical conductance of our sensors increases slightly when exposed to humidity and decreases exponentially when exposed to acetone. This is an unusual behavior for the material, as it typically exhibits p-type conductance. However, when operating at temperatures greater than 300°C (Figure 18 (b)), we observed a transition in the sensor signal. Additionally, we observed that the electrical conductance increases with increasing temperature, which is a typical behavior for metal oxide semiconductors.

The Pt-Co_3O_4 sensors demonstrate a greater sensitivity to acetone compared to the non-modified Co_3O_4 sensor across the tested range of operating temperatures, as shown in Figure 4.18(a). This enhanced response in the Pt-Co_3O_4 sensors can likely be attributed to the spillover effect resulting from the Pt functionalization. The Pt-Co_3O_4 sensors were found to have a higher sensitivity to 10 ppm of acetone when operating in dry air at 500 °C, as shown in Figure 4.19 (a). Additionally, the Pt-Co_3O_4 sensors had a higher sensitivity compared to the pristine Co_3O_4 sensors in dry air at 500 °C, as shown in Figure 4.19 (b,c). Henceforth, the term "sensor" in this study refers to the Pt-Co_3O_4 sensor. Furthermore, the sensor demonstrated a quick response to the presence of acetone and returned to its baseline when acetone was no longer present in the chamber, as shown in Figure 4.19 (d).

The sensors were tested for their response and recovery time using conductometry measurements. The response and recovery time of the sensors were found to be ≤ 380 seconds and ≤ 650 seconds respectively, as per the results in Table 4.3.

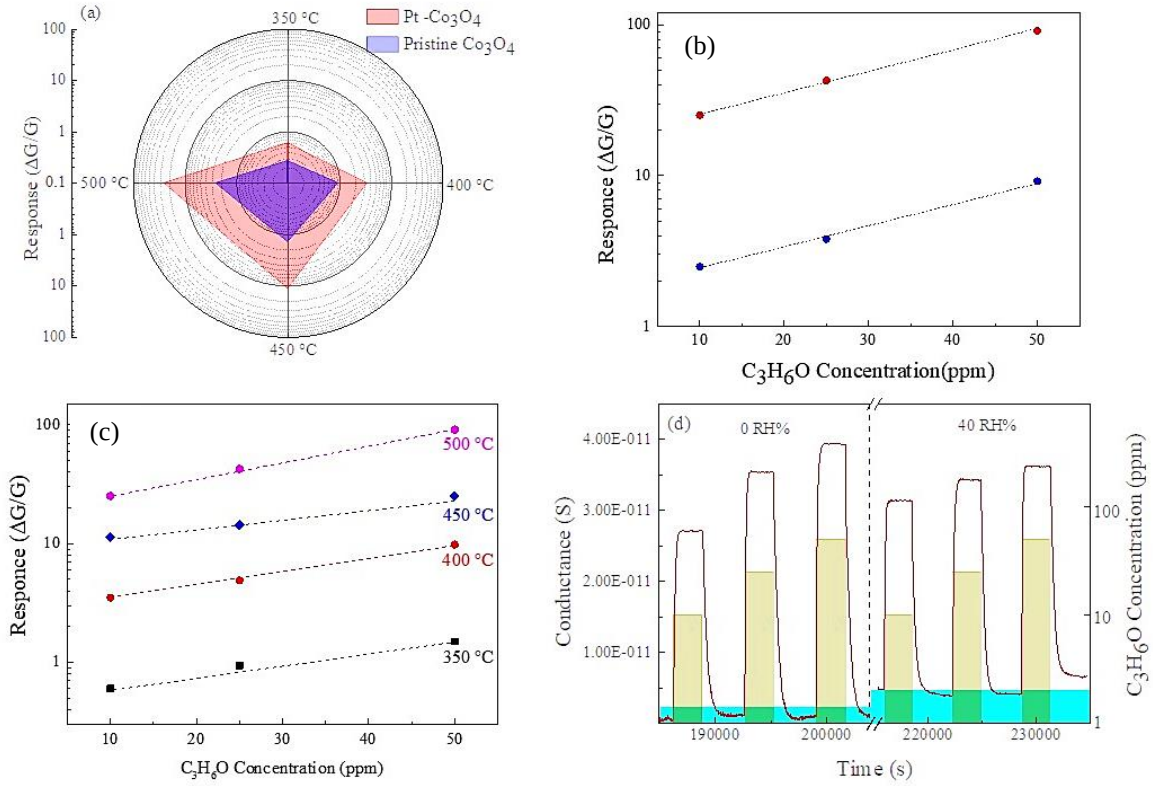

Figure 4.19. (a) response of the Pt-Co_3O_4 and pristine Co_3O_4 sensors to 10 ppm acetone at dry air, (b) response vs. acetone concentration of the Pt-Co_3O_4 and pristine sensor at the operating temperatures of 500 °C in dry air, (c) response vs. acetone concentration of the Pt-Co_3O_4 sensor at the range of operating temperature 350-500 °C in dry air, (d) conductance variation of the Pt-Co_3O_4 sensor at the operating temperature of 500 °C to 10, 25 and 50 ppm acetone in dry air and 40 RH% air.

The selectivity is one of the key properties of the sensors, hence we have tested the sensors toward H_2, NO_2, CO, C_2H_5OH in the operating temperature 350-500 °C and the response values are shown in Figure 4.20. The sensor has demonstrated good selectivity to acetone at its best operating temperature (Figure 4.21). Furthermore, the sensors have hold their sensing functionalities for three consecutive cycles (Figure 4.22 (a)) and good stability for tested four weeks (Figure 4.22 (b)). Table 4.4 summarize the recent advancement on Co_3O_4 in acetone sensing applications. In this context, the fabricated Pt-Co_3O_4 is a handy candidate for acetone sensing and can potentially be used in detecting breath acetone sensing.

Table 4.3. Acetone sensing dynamics of the Pt-Co_3O_4 and pristine Co_3O_4 sensor in dry air.

Temp. (°C)	Conc. (ppm)	Pt-Co_3O_4			Co_3O_4		
		Response	T_{res} (s)	T_{rec} (s)	Response	T_{res} (s)	T_{rec} (s)
350	10	0.6	310	330	0.27	420	690
	25	0.94	300	300	0.35	520	750
	50	1.5	310	390	0.39	570	750
400	10	3.5	390	500	0.95	750	830
	25	4.9	380	550	1.09	690	720
	50	9.8	390	610	1.14	570	810
450	10	11.3	370	660	1.05	750	900
	25	14.3	380	710	1.21	600	960
	50	25.2	450	800	1.46	540	900
500	10	25.2	380	650	2.51	540	660
	25	42.6	380	710	4.29	500	630
	50	91.0	420	770	7.88	480	780

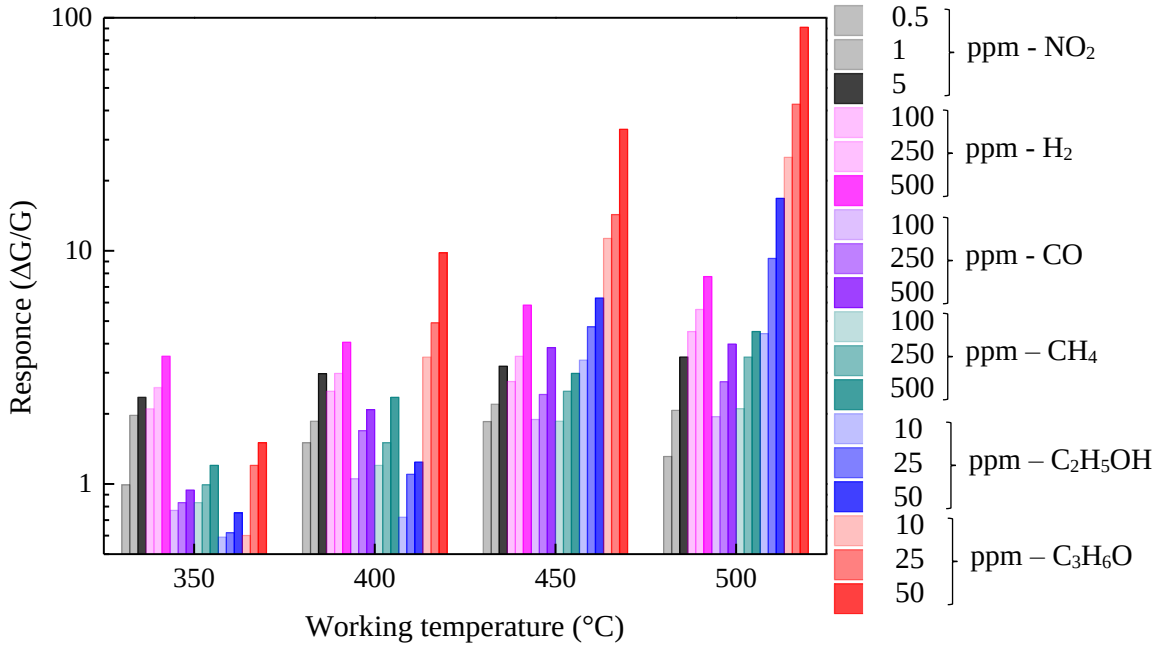

Figure 4.20. Gas sensing response of the Pt-Co_3O_4 sensor towards NO_2, H_2, CO, CH_4, C_2H_5OH and C_3H_6O at the range of operating temperature in dry air.

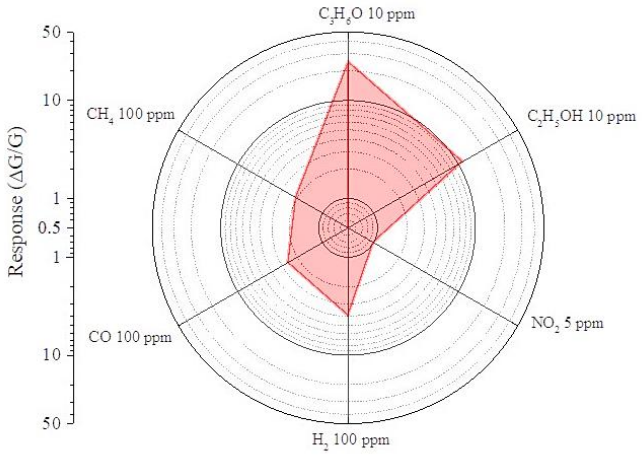

Figure 4.21. Pt-Co_3O_4 sensors response to acetone, ethanol, nitrogen dioxide, hydrogen, carbon monoxide and methene gases at 500 °C in dry air.

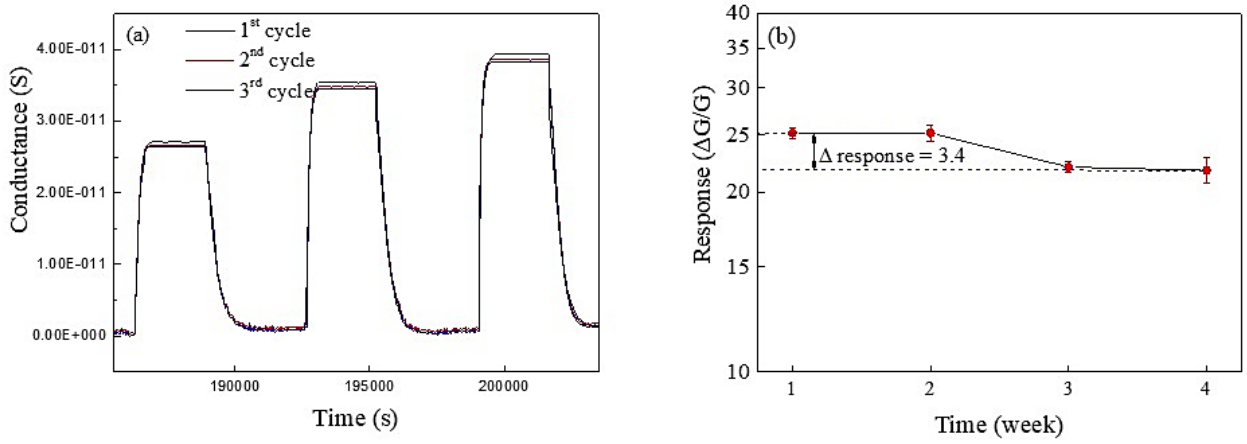

Figure 4.22. (a) repeatability of the Pt-Co_3O_4 sensors signal for three consecutive cycles, (b) stability of the response of the Pt-Co3O4 sensor to acetone for the period of four weeks.

Table 4.4. Recent advancement on acetone sensing by low dimensional Co_3O_4 nano structures.

Material	Structure	Conc. (ppm)	Temp. (°C)	Gas Response	LOD (ppm)	Ref.
Co_3O_4	nanosheets	50	160	6.1	5	[50]
Co_3O_4	Nano particles	100	200	8.61	0.1	[51]
Co_3O_4	hierarchical nanofibers	100	190	9.3	5	[52]
Ir–GO–Co_3O_4	Composite nanofiber	5	300	2.29	0.120	[53]
Au-doped Co_3O_4	Nano cubes	100	340	22.2	0.01	[54]
PdO-Co_3O_4	Hollow Nanocages	5	350	2.51	0.01	[55]
Co_3O_4	porous nanosheets	100	150	11.4	1.8	[56]
Co_3O_4	nanorods	100	240	5.6	2	[57]
Co_3O_4	Nano cubes	100	240	2.99	10	[58]
Co_3O_4	Porous rectangular rods	50	200	1.94	5	[59]
Co_3O_4	Nano petal with nano walls	10	500	2.5	0.6	This work
Pt-Co_3O_4	Nano petal with nano walls	10	500	25.2	0.07	This work

$$H_2O(g) \rightarrow OH^- + H^+ \quad (4.6)$$

$$H_2O\,(g) + (M_M + O_o) \leftrightarrow (M_M^{\delta+} - OH^{\delta-}) + (OH)_o^- + e^- \quad (4.7)$$

$$H_2O\,(g) + 2(M_M + O_o) \leftrightarrow 2(M_M^{\delta+} - OH^{\delta-}) + V_o^{++} + 2e^- \quad (4.8)$$

Two mechanisms of H_2O adsorption are worth noting. The first is the dissociation of H_2O and its reaction with a lattice oxygen to form O_O (Equation 4.6, 4.7). The second mechanism is the reaction of water with lattice oxygen forming two terminal hydroxyl groups ($M_M^+ – OH^–$) and one oxygen vacancy (VO^{++}, Equation 4.8). The adsorbed $OH^–$ group acts as a donor and the oxygen vacancies act as acceptors. This leads to increased conductance of the sensor in humid air (Figure 4.23 (a)). However, the response of the sensors decreases with increasing humidity levels when exposed to 10 ppm acetone at different humidity levels of 0, 20, 40, 60 and 75% at an operating temperature of 500 °C (Figure 4.23 (b)). This decrease may be due

to the formation of hydroxyl groups on the surface of the sensor's material [60]. It can be suggested that the following possibilities may be causing the decrease in the sensor's response: a decrease in band bending due to a decrease in ionosorption oxygen, the formation of Co_{Co}^{+}-OH^{-} dipole which increases electron affinity and leads to increased resistance to electron motion in the material, and competition between water molecules and acetone to react with oxygen species. Additionally, techniques such as diffuse-reflectance-infrared-Fourier-transformed-spectroscopy (DRIFTS) or in-situ operando measurements can provide more insight into this mechanism.

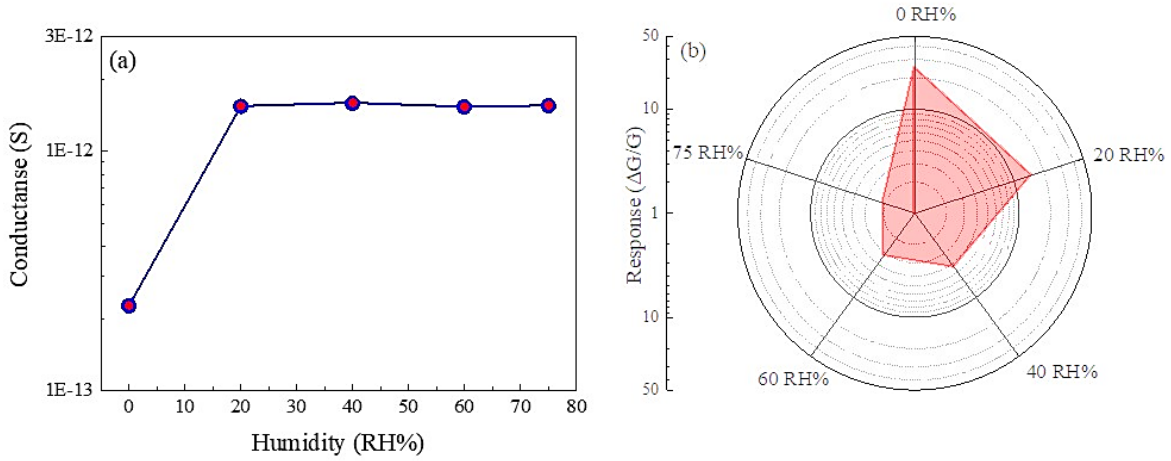

Figure 4.23. (a) Conductance, (b) response to 10 ppm acetone of the Pt-Co3O4 sensors at different humidity (0,20,40,60,75 RH%) in air when working the 500 °C.

4.2.3 Working mechanism

4.2.3.1 Inversion of the conductance from p-n

Co_3O_4 is typically a p-type semiconductor, where holes are the primary carriers. The energy band diagram of ideal Co_3O_4 is shown in Figure 4.24 (a). When the material is exposed to atmospheric air, oxygen is adsorbed on the surface and combines with oxygen vacancies by capturing electrons in the conductance band. This leads to an increase in hole concentration in the valence band and a downward bending of the energy band as shown in Figure 4.24 (b). The relevant reaction is shown in Equations 4.9 and 4.10 [61]. However, at higher operating temperatures (> 290 °C) the intra-lattice oxygen is diffused from the interior to the surface of

the crystal to maintain the oxygen equilibrium between the interior and the surface [62]. Accordingly, oxygen vacancies are created as shown in Equation (4.11). As a result, the surface-near region oxygen is replaced by both oxygens from the gas phase (as in the case of low temperature) and oxygen that has diffused in. The width of the hole accumulation layer is regulated by this diffusion. For example, when the concentration of oxygen vacancies at the surface $[V_0^{++}]_{surface}$ is equal to the concentration of oxygen vacancies in the bulk $[V_0^{++}]_{bulk}$, the space charge is eliminated and the band becomes flat as shown in Figure 4.24 (a). On the other hand, when $[V_0^{++}]_{surface} < [V_0^{++}]_{bulk}$, a negative charge trapped at a surface acceptor state (*Ea*) creates an electron depletion space charge layer, leading to upward band bending at the donor state (Ed) as shown in Figure 4.24 (c). This results in the transfer of electrons into the conduction band [63]. Furthermore, when the electron concentration is higher than the hole concentration the surface conductance type is inverted from p-n. Besides, the formed oxygen vacancies promote the adsorption of oxygen at the surface which in turn increases the upward band bending and the depletion layer width as represented in Figure 4.24 (d). Similarly, Vetter et. al. showed the effect of oxygen diffusion in the crystal lattice to surface Co_3O_4 and Choi et. al. showed the role of the oxygen vacancy site as an activity site for a sensing reaction and improving the selectivity of the Co_3O_4 sensor [34].

$$O_2 + e^- \rightarrow O_2^- \tag{4.9}$$

$$V_O^{++} + \frac{1}{2}O_2 \rightarrow O_O + 2h^+ \tag{4.10}$$

$$O_O^x \rightarrow \frac{1}{2}O_2 + \ddot{V_O} + 2e \tag{4.11}$$

$$CH_3COCH_3\ (gas) + 8O^- \rightarrow 3CO_2 + 3H_2O + 8e^- \tag{4.12}$$

A dot represents a positive charge and × denotes neutrality. Subscripts denote the atom which would normally occupy the site, and *e* denotes conduction electrons and (V_o) is a surface oxygen vacancy.

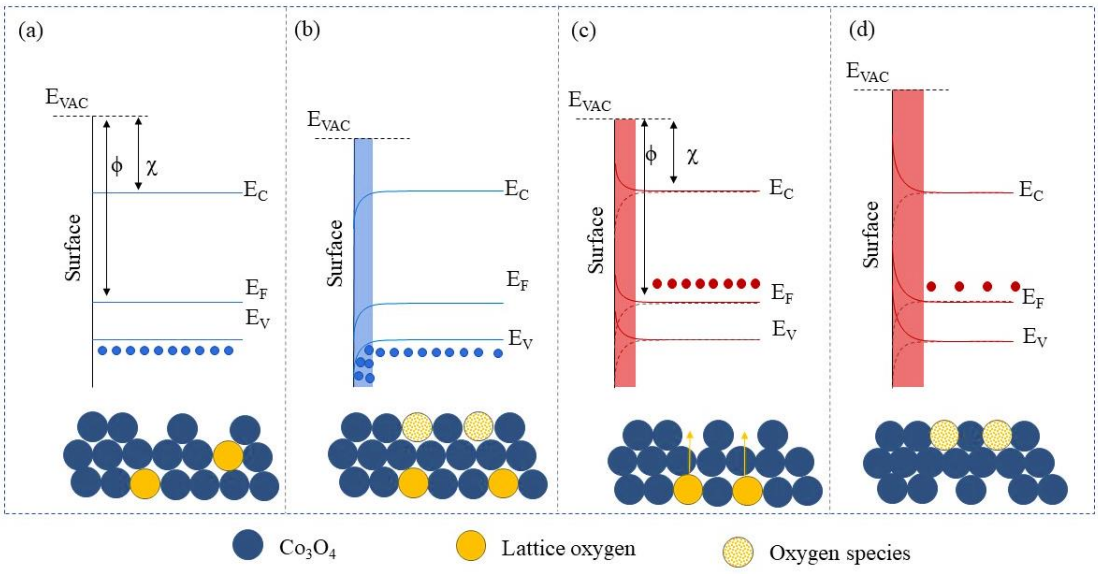

Figure 4.24. Illustration of the relative energy band diagram of Co_3O_4 (a) before interacting with air, (b) when interacting with air an operating temperature < 300 °C, (c) when operating at a higher temperature (> 300 °C) $[V_0^{++}]_{surface} < [V_0^{++}]_{bulk}$ (d) when air is interacting at a higher temperature.

4.2.3.2 Acetone sensing mechanisms and selectivity

When the material is exposed to atmospheric air, oxygen molecules are adsorbed and oxygen species are combined with oxygen vacancies as stated in Equations 4.9 and 4.10. Furthermore, when the sensor is operating at a higher temperature, the formation of oxygen vacancies on the surface of Co_3O_4 (Equation 4.11) increases the adsorption of molecular oxygen [62]. As a result, the increase of oxygen species on the surface of Co_3O_4 improves the interaction of acetone with the sensor because of more reactive sites. When acetone interacts with the material, electrons are donated to the oxygen species by acetone molecules as shown in Equation 4.12 [58]. As a result, the return of electrons to Co_3O_4 reduces the thickness of the electron depletion layer, decreasing the electrical resistance of the material, thus showing a gas sensing response to acetone. Additionally, the nanowalls structure with nano petals provides a good channel for carrier transport, promoting fast diffusion of charge carriers throughout the material, reaching the edges of the nanowalls and nano petals. Furthermore, the presence of the (111) crystal plane, where only Co^{2+} cations are present, in the grown Co_3O_4 enhances the catalytic activity of the material. This allows for easy

adsorption of more oxygen and analyte gas molecules, improving the sensor's response [30,64].

4.2.3.3 Higher response in Pt-Co_3O_4 compared to pristine Co_3O_4

Usually, functionalization provides chemical sensitization called as the spillover effect which activates or creates the reactive species in one phase and they are subsequently transported to another phase [65]. The gas sensing capabilities of MOXs are affected by various spillover processes. These include the spillover of the target gas, the spillover of oxygen, and the inverse spillover of oxygen from the MOX. These processes are commonly used to explain the increased efficiency of MOX gas sensors [63]. The process of inverse spillover refers to the adsorption and reaction of the target gas on the surface of the functionalizing material, leading to an increase in the catalytic activity of the material. This process is often used to explain the enhanced receptor function of MOX gas sensors. For example, a study by Yunil et al. demonstrated that the catalytic activity of Pt-loaded materials toward acetone was significantly enhanced at temperatures above 300 °C [66].

The inverse spillover process is a mechanism in which the adsorption and reaction of the analyte gas on the surface of the functionalizing material leads to an enhancement in the catalytic activity of the material. This process has been shown to improve the response of the Pt-Co_3O_4 sensor at high temperatures, such as above 300 °C. However, another possible explanation for the enhancement in response is the spillover activation of oxygen, which increases the concentration of active oxygen species at the surface. This leads to an initial increase in the band bending in the air compared to the pristine material, and in turn, results in changes in the surface charge and a greater sensor signal when exposed to acetone. [63]. On the other hand, spillover of the analyte gas process which is the enhancement of the adsorption and dissociation of the analyte gas molecules in which space charge layer is also available. However, this process is not effective until the acetone is present. On the other hand, the work function of Pt nanoparticles (5.35 eV) is higher than that of Co_3O_4 (4.5 eV) [67]. As a result of the inverse spillover process and the activation of oxygen, the transfer of electrons through the interface between Pt and Co3O4 can be facilitated, leading to an improvement in the response of the sensors by forming a Schottky barrier [68].

4.3 Co_3O_4 nanowires for hydrogen sensing

4.3.1 Material analysis

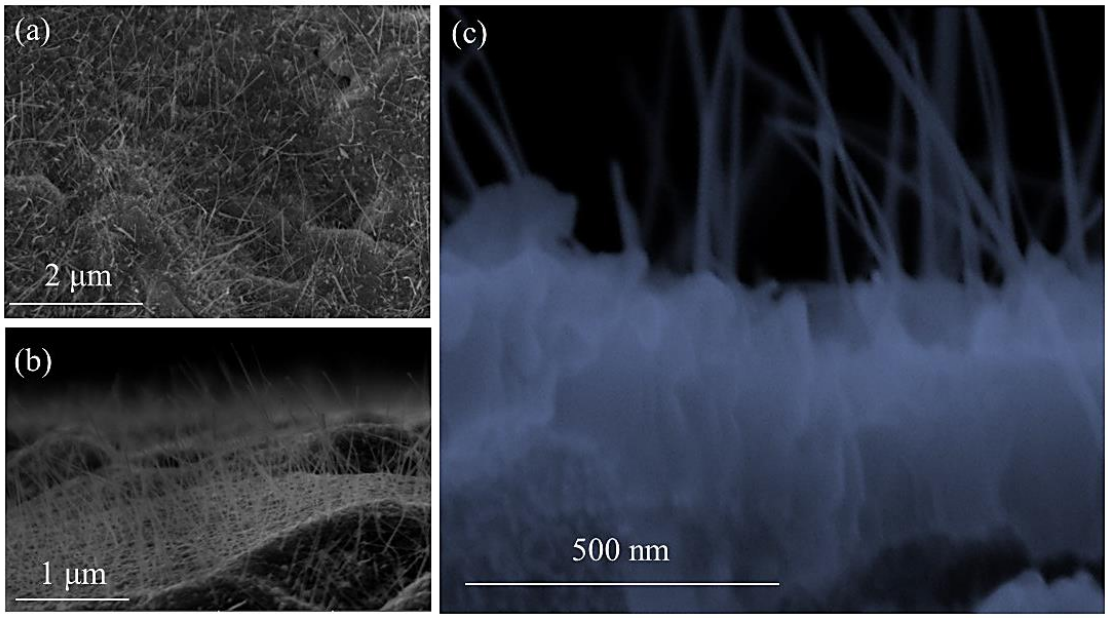

Figure 4.25. FE-SEM images of prepared Co_3O_4 nanowires (a) 100 nm thick (b) 50 nm thick, (c) cross-sectional view of Co_3O_4 nanowires with initial Co thickness of 200 nm.

Figure 4.25 (a-b) shows FE-SEM images of the prepared Co_3O_4, revealing the formation of nanowires. Figure 4.25 (b) displays a higher nanowire density in the 50 nm sample. The 100 nm sample shows a non-homogeneous distribution of longer nanowires. Figure 4.25 (c) is a cross-sectional FE-SEM view of the 200 nm thick material, revealing three layers. Nanowires grow on the small grain of the top layer. Consequently, the growth mechanism can be understood as described in Chapter 3, section 5.1.1 (Figure 3.7).

The TEM image in Figure 4.26 (a) shows nanowires with diameters 6-50 nm and lengths 1-5 µm. Figure 4.26 (b) shows electron diffraction indicating three main Co_3O_4 reflection planes: (111), (220), and (311) (CIF no. 9005896). HR-TEM images in Figure 4.26 (c,d) show that the most prominent plane is (311), indicating growth in the (311) direction of the Co_3O_4 crystal. Figure 4.27 (a) presents TEM characterization of various sections of the Co_3O_4 nanowires, with Figure 4.27 (b-d) confirming growth in the (311) direction throughout the wire. Figure 4.28 shows EDS analysis, revealed that the nanowires consist only of Co and O.

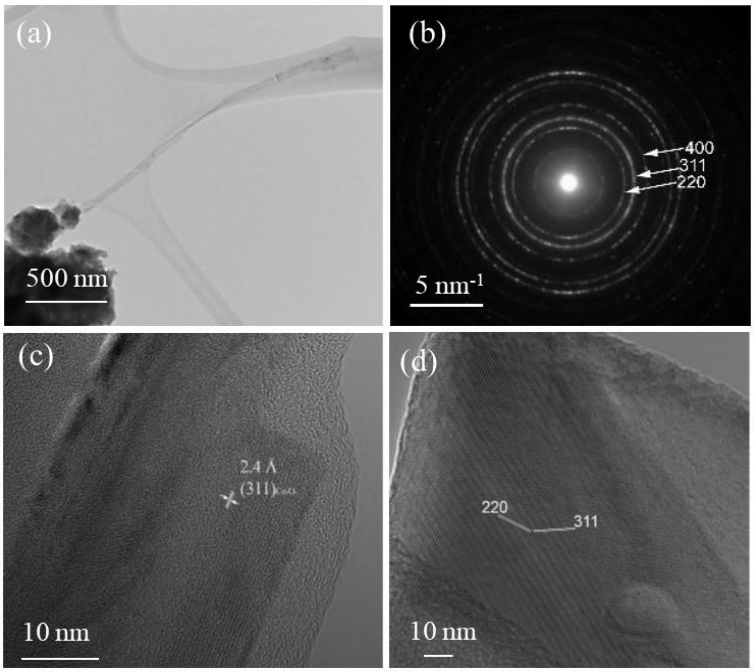

Figure 4.26. (a) conventional TEM image of a grown Co_3O_4 nanowire, (b) electron diffraction pattern (SAED), (c)-(d) HR-TEM image of the TEM image shown in (a).

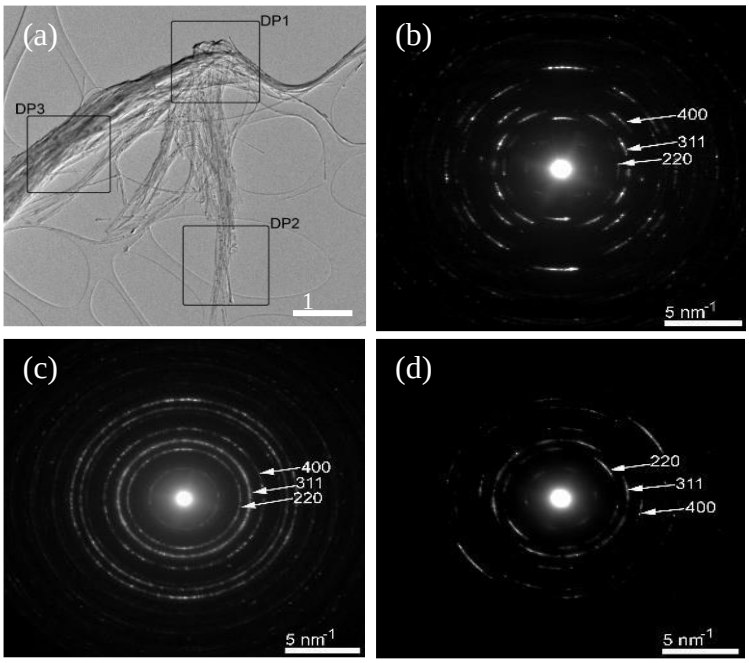

Figure 4.27. (a) An agglomeration of Co_3O_4 nanowires and the electron diffraction patterns obtained from different regions of the area shown in image a: (b) diffraction pattern obtained from the area marked with "DP1", (c) diffraction pattern obtained from the area marked with "DP2" and (d) diffraction pattern obtained from the area marked with "DP3".

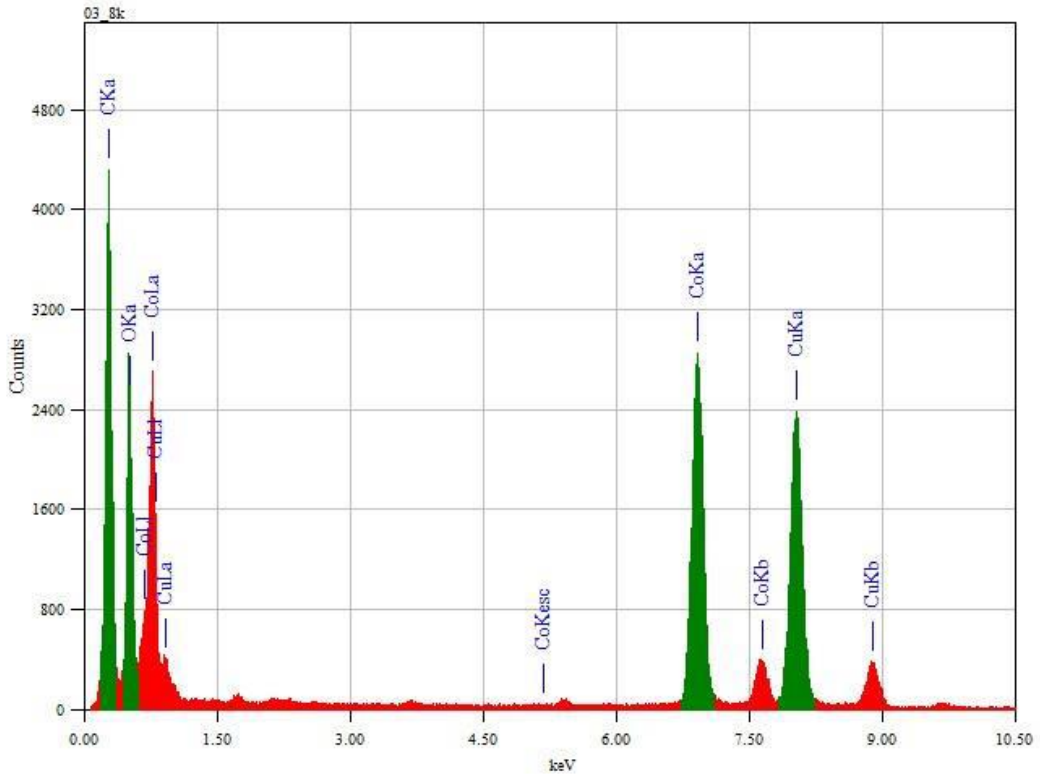

Figure 4.28**.** The EDS spectrum obtained on the agglomeration of nanowires, shown in figure (4.28), confirms the presence of Co and O; the presence of Cu and C peaks is due to electrons scattering on the TEM grid.

Raman spectra of Co_3O_4 reveals five characteristic peaks at 195, 482, 521, 620 and 692 cm^{-1}, which correspond to the F_{2g1}, E_g, F_{2g2}, F_{2g3}, and A_{g1} symmetric phonon modes of crystalline Co_3O_4 [40]. The strongest peak at 195 cm^{-1} is from Co^{2+} tetrahedral vibrations, while the weakest peak at 692 cm^{-1} is from Co^{3+} octahedral vibrations (Figure 4.29). Co3O4's cubic spinel structure has Co^{3+} at octahedral sites (16a Wyckoff) and Co^{2+} at tetrahedral sites (8a Wyckoff). The bands at 195 and 692 cm^{-1} can be assigned to the Raman vibrations of Co^{2+} - O^{2-} and Co^{3+} - O^{2-} respectively, which confirms the formation of Co_3O_4 and suggests that tetrahedral sites are dominant compared to octahedral sites in the prepared structures [69].

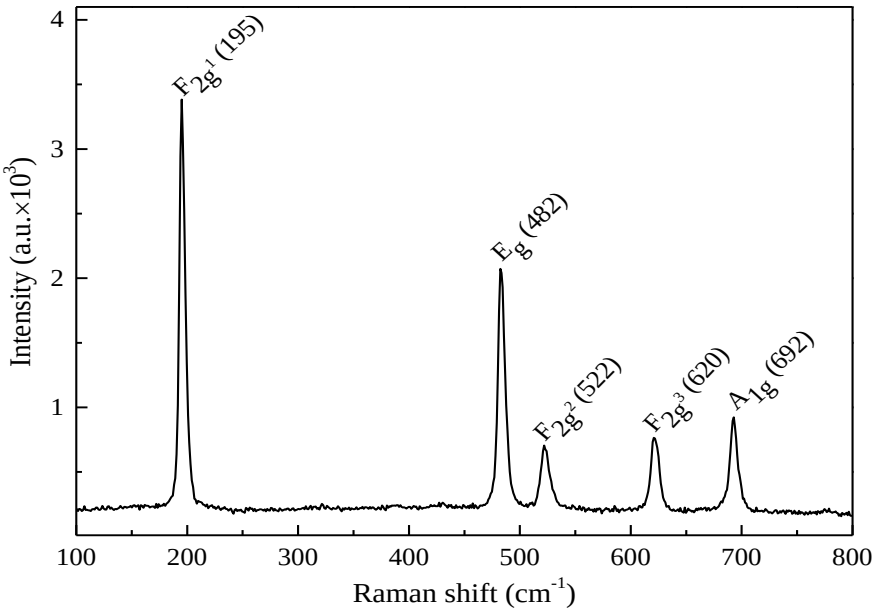

Figure 4.29. Raman spectra of the prepared Co_3O_4 nanowires.

Figures 4.30 (a,b) display the EPR spectra of the Co_3O_4 nanowires measured in the X- and Q-bands, respectively, before and after thermal aging at 400 ^oC. The X-band spectrum of the as-grown Co_3O_4 sample exhibits a very broad line at low magnetic fields, which further broadens as the temperature is decreased to 100 K (Figure 4.30 (c)). After the thermal aging of the Co_3O_4 sample this line disappears and the X-band spectrum shows no difference from the spectrum of the alumina substrate [Figure 4.30 (a)]. A similar evolution of the broad line is observed in the Q-band spectrum as well (Figure 4.31 (b)). This line is associated with the presence of a minority ferromagnetic phase, consisting probably of Co and/or CoO clusters [70] due to the incomplete oxidation of the cobalt layer. The disappearance of the line after the 400 ^oC annealing could be due to the dissolution of the ferromagnetic clusters or oxidation processes that affected the ferromagnetic couplings.

It should be mentioned that the EPR signature spectrum of Co_3O_4 consists of a Lorentzian shaped line with g ~ 2.23 [71] corresponding to ~314 mT in the X- and ~1090 mT in the Q-band spectra, respectively, from the paramagnetic Co(II) ions in tetrahedral sites. The absence of this line in the recorded spectra, even for the more sensitive Q-band, can be explained by the very small amount of Co_3O_4 actually measured (sample volume of ~ 10^{-3} mm^3).

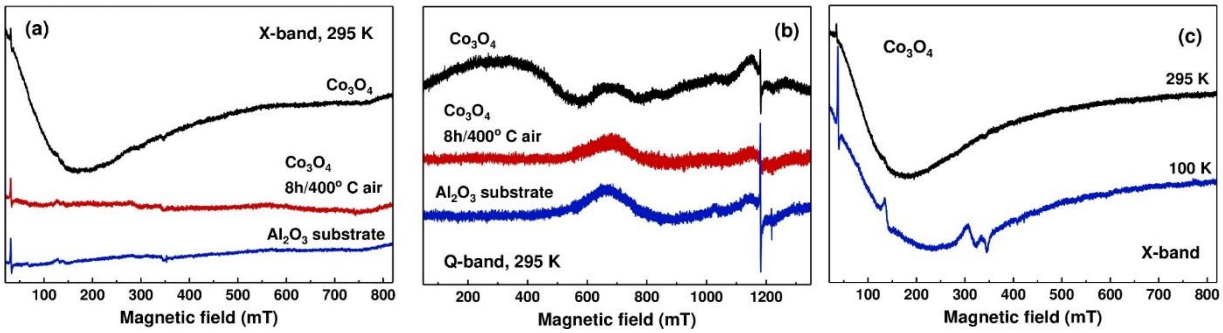

Figure 4.30. EPR spectra of the Co_3O_4 nanowires, before and after annealing at 400 °C for 8 h, measured at room temperature in the (a) X- and (b) Q-band. (c) Room temperature X-band EPR spectrum of the Co_3O_4 nanowires compared to the spectrum measured at 100 K. The sharp lines in the 100 K spectrum are from paramagnetic centers in the alumina substrate.

4.3.2 Gas sensing analysis

Figure 4.31 (a) depicts the temperature-dependent conductance of Co_3O_4 nanowires in dry and humid air (40% RH). Both sensors show low conductance that rises with temperature in dry air, typical of metal oxide (MOXs) semiconductors. Conductance is lower in humid air due to water molecules absorbed onto MOXs surfaces, either as molecules (physisorption) at low temperatures or as chemical bonds (chemisorption) at high temperatures, hindering baseline conductance [16]. It has been observed that there is a significant decrease in conductance when sensors are operating at 500 °C in wet air. The performance of Co_3O_4 in detecting hydrogen at 300-500 °C was evaluated (Figure 4.31 (b)). Sensors were stabilized in a testing chamber with synthetic dry air for 4 hours before taking readings at each operating temperature. Hydrogen sensing was measured at 100, 250, and 500 ppm with each cycle lasting 90 minutes, including 30 minutes of exposure to gas and 60 minutes of exposure to synthetic air for recovery. The testing chamber (1L) takes 15 minutes to change the environment with a flow rate of 200 sccm.

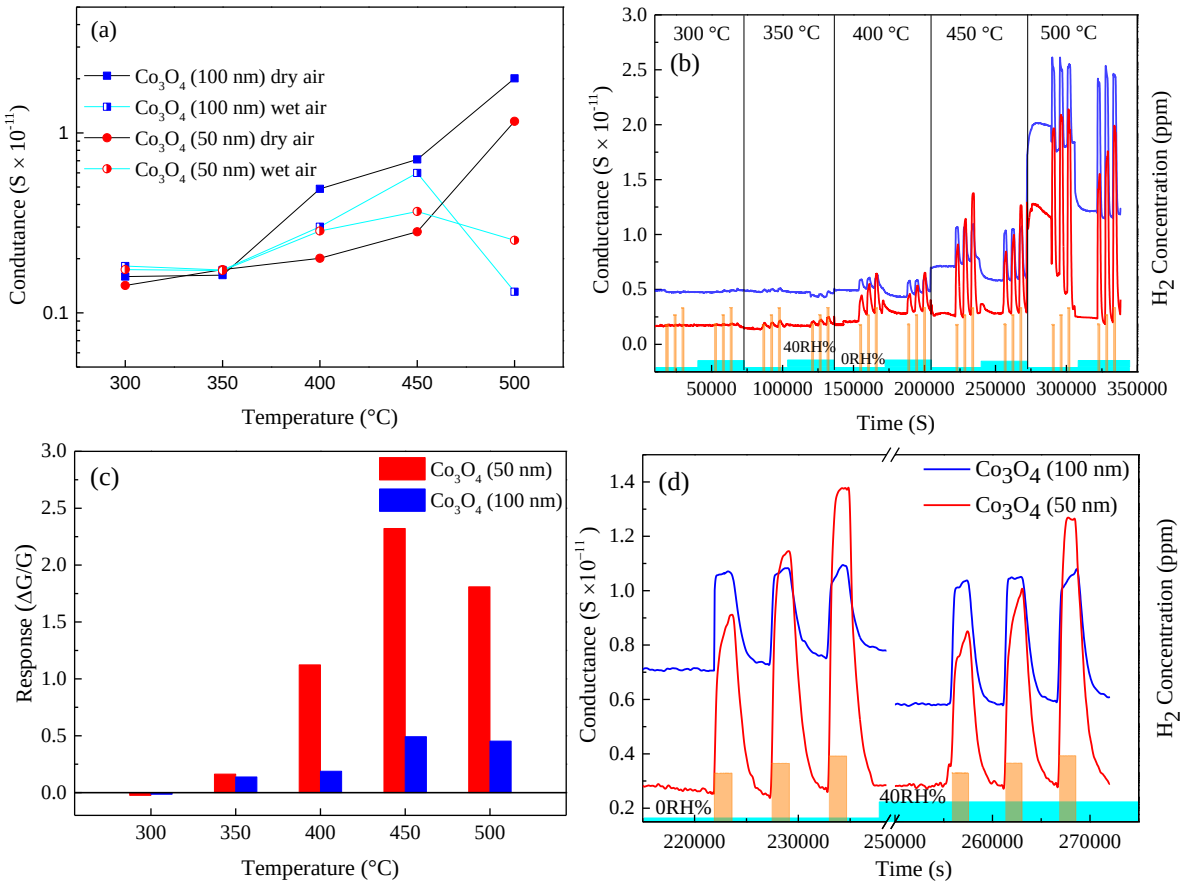

Figure 4.31. The gas sensing functionality of the Co_3O_4 nanowire sensors (a) variation of the conductance of the sensors, (b) dynamic response of the sensors at the tested temperature range (300-500 °C), (c) response of the sensors for 100 ppm H_2 at dry air, (c) dynamic response of the sensors at the optimum operating temperature (450 °C) in dry air and 40 RH%.

The sensors showed not much response at temperatures below 300 °C (Figure 4.31 (c)). Above 300 °C, they demonstrated an inversion of signal (Figure 4.31 (c)). Vladimirova et al. reported inversion of the conductance type of Co_3O_4 from p-n to n-p when operating at a temperature higher than 250 °C in dry air due to the breaking apart of Co^T-O_2^{2-}-Co^O surface adducts [49]. Also, Lin et. al. has reported the participation of lattice oxygen of the Co_3O_4 in the oxidation process which helps to invert the conductance [50]. Accordingly, in this context, the inversion of the conductance is thermally-driven. Furthermore, an exceptional

drop in the conductance at 500 °C at humidity air can be due to the desorption of absorbed oxygen from the Co_3O_4 and percent water molecules [72].

The sensor with a higher density of nanowires (50 nm) showed a higher response than the sensor with a lower density of nanowires (100 nm), with a peak response of 2.32 for 100 ppm at 450 °C (Figure 4.31 (c)). Figure 4.31 (d) displays the dynamic gas sensing nature of both sensors at 450 °C. Both sensors recover to the baseline conductance in 40% RH air, but the Co_3O_4 (50 nm) sensor fully recovers to baseline conductance even in dry air. The estimated response time and recovery time of the Co_3O_4 (50 nm) sensor for 100 ppm H_2 are ≤ 330 s and ≤ 850 s, while the Co_3O_4 (100 nm) sensor has ≤ 300 s and ≤ 900 s response and recovery times, respectively (Table 4.5).

Table 4.5. Various hydrogen sensors are fabricated with different MOXs nanostructures.

Material	Method	Operating temperature (°C)	Concentration (ppm)	Response	Response /recovery time (s)	Reference
Co_3O_4	Thermal oxidation	450	100	2.32[a]	480/1240	This work
ZnO	Spin coating	150	150	0.21[b]	70/204	[73]
NiO	Hydrothermal	250	150	1.91[b]	150	[74]
Co/SnO_2	Electrospinning	330	100	23[c]	2/3	[75]
MoO_3	Hydrothermal	RT	1000	17.3[d]	10.9/30.4	[76]
Co_3O_4/ZnO	Electrospinning	300	10	1.33[b]	70/70	[75]
ZnO	Decomposition	180	80	1.78[b]	1/2	[77]
ZnO	VLS	250	100	72[c]	<50/100	[78]
$WO_{2.72}$	Hydrothermal	RT	100	0.27[c]	56/36	[79]
TiO_2	Hydrothermal	100	150	0.53[b]	85/620	[80]

[a]- ($\Delta G/G$), [b]- ($\Delta R/R$), [c]- R_a/R_g, [d]-I_g/I_a

The sensor response is influenced not only by temperature but also by the type of gas. At 450 °C in dry air, the sensor (50 nm, higher density of nanowire) was tested for selectivity with C_2H_5OH, C_3H_6O, NO_2, CH_4, and CO. The results showed selective H_2 detection (Figure 4.32 (a)). The repeatability of the sensor signals is also a key factor in its performance. The detection limit (LOD, 10% error) of the Co_3O_4 sensor in dry air is 360 ppb. Sensors have higher sensitivity when operating in dry air (Figure 4.32 (b)), which is due to the higher concentration of free electrons in this environment. This leads to more ionosorbed oxygen,

which in turn enhances the sensor's ability to react with hydrogen and detect it at lower concentrations [81]. The H_2 sensing ability of the sensor remains consistent in three consecutive tests of 100 ppm at the optimal operating temperature, as shown in Figure 4.32 (c). Additionally, the sensor exhibits stability for up to 25 days with a decrease in response by 10% at 450 °C, as depicted in Figure 4.32 (d).

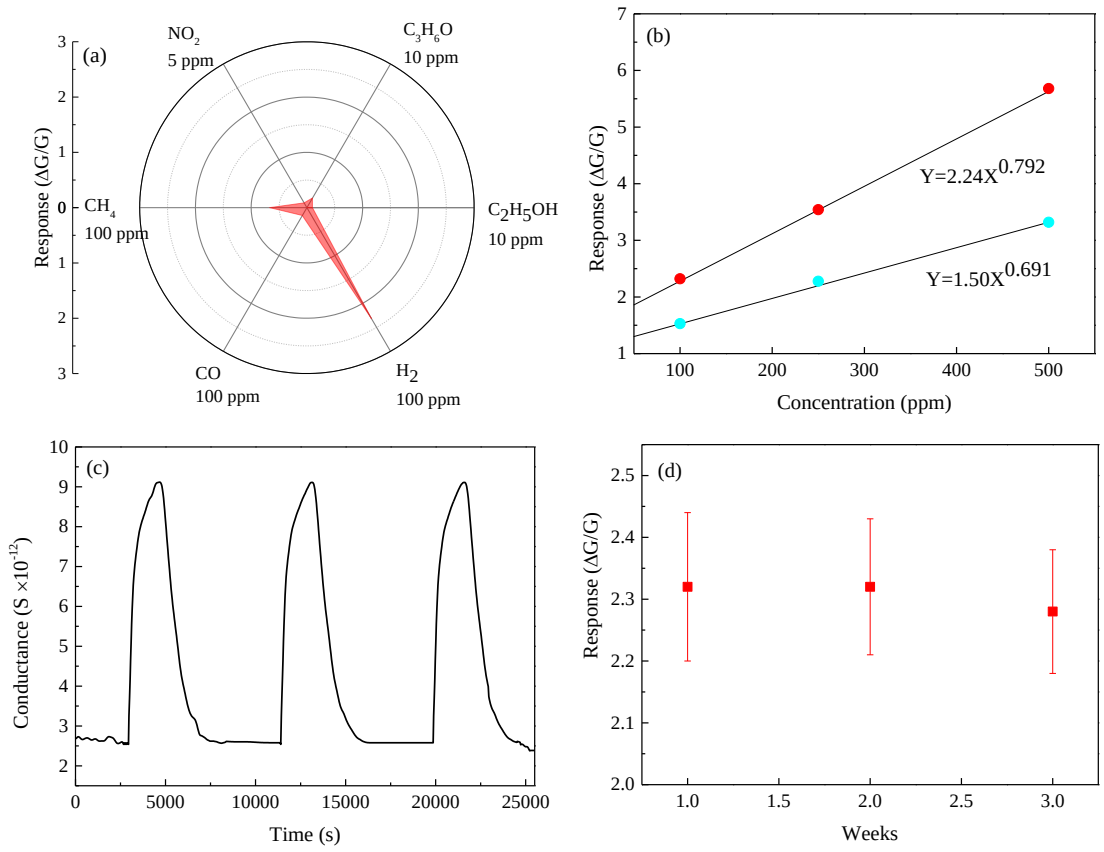

Figure 4.32. (a) Selectivity comparison of the sensors at 450 °C against the ethanol, acetone, carbon monoxide, methane, and nitrogen dioxide in dry air, (b) response vs concentration fitting, (c) repeatability, (d) Stability of the Co_3O_4 nanowires at the 450 °C in dry air.

The study was expanded to evaluate the sensor's performance under varying humidity levels, from dry air to 90% relative humidity. Figure 4.33 (a) displays the dynamic response of the sensor at different humidity levels (10, 20, 40, 60, 80, 90 RH%) after 25 days of initial testing. The baseline conductance remains unchanged with humidity, which is uncommon for MOXs sensors. In general, the baseline resistance is decreased by the hydroxyl ions (OH^-) and protons (H^+) formed by the dissociation and adsorption of water molecules on the MOXs

surface. Typically, OH^- attaches to the metal cation and H^+ attaches to the oxygen in the MOXs [82]. However, this mechanism can change to a hopping mechanism, where H_2O is physiosorbed on the MOX surface by attaching to the H^+ already generated due to chemisorption of H_2O at low humidity conditions [82]. This study found the MOX's baseline conductance remains stable and strong even at high humidity levels. Figure 4.33 (a) shows the MOX's response to different humidity levels (10-90% RH%) after 25 days of testing. Unlike other MOXs sensors, the conductance baseline is not affected by humidity, as seen in Figure 4.33 (a). Figure 4.33 (b) demonstrates the MOX's response to 100 ppm H_2 at various humidity levels (0-90% RH%). The results show no significant difference between the response at dry air (2.32) and 90% RH% (2.26) at the optimal operating temperature.

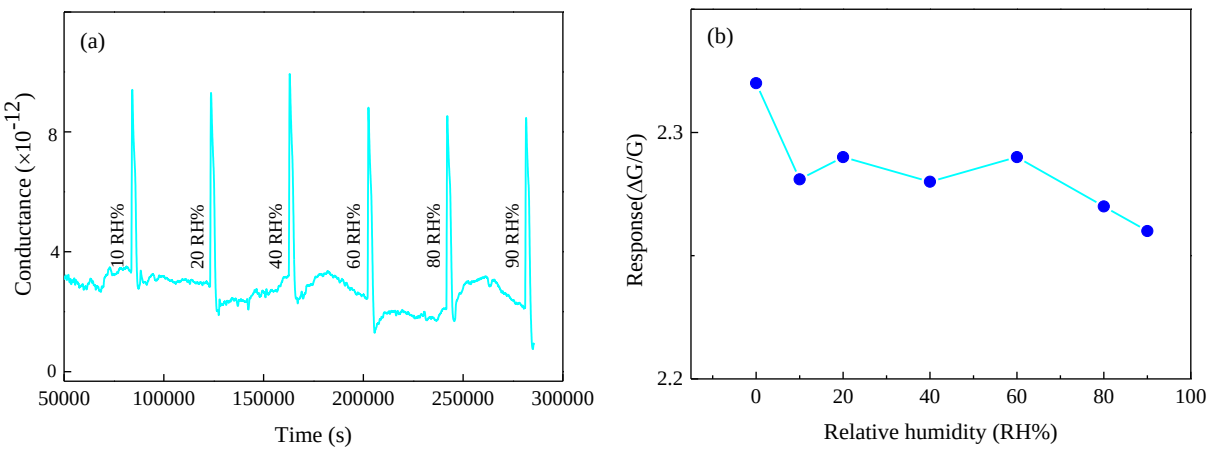

Figure 4.33. The Co_3O_4 nanowire sensor functionality to 100 ppm H_2 at humidity environment (a) dynamic response at 10, 20, 40, 60, 80, and 90 RH%, (b) response of the sensor at the 0, 10, 20, 40, 60, 80, and 90 RH% when operating at 450 °C.

4.3.3 Working mechanism

Formation of the hole-accumulating region is inn the Co3O4 when exposed to air illustrated in Figure 4.34 (a, b) and is comprehensively explained in section 4.2.3. This leads to an increase in conductance when exposed to air (Figure 4.34 (d, e)). Additionally, when exposed to reducing gas, such as H_2, is reacts with adsorbed oxygen species and releases electrons (Figure 4.34 (c)), it reacts with the adsorbed oxygen species and releases the electrons back as shown in Equations (4.13, 4.14) [83,84]. So, the decreased width of the hole accumulation layer leads to a decrease in conductance (Figure 4.34 (f)).

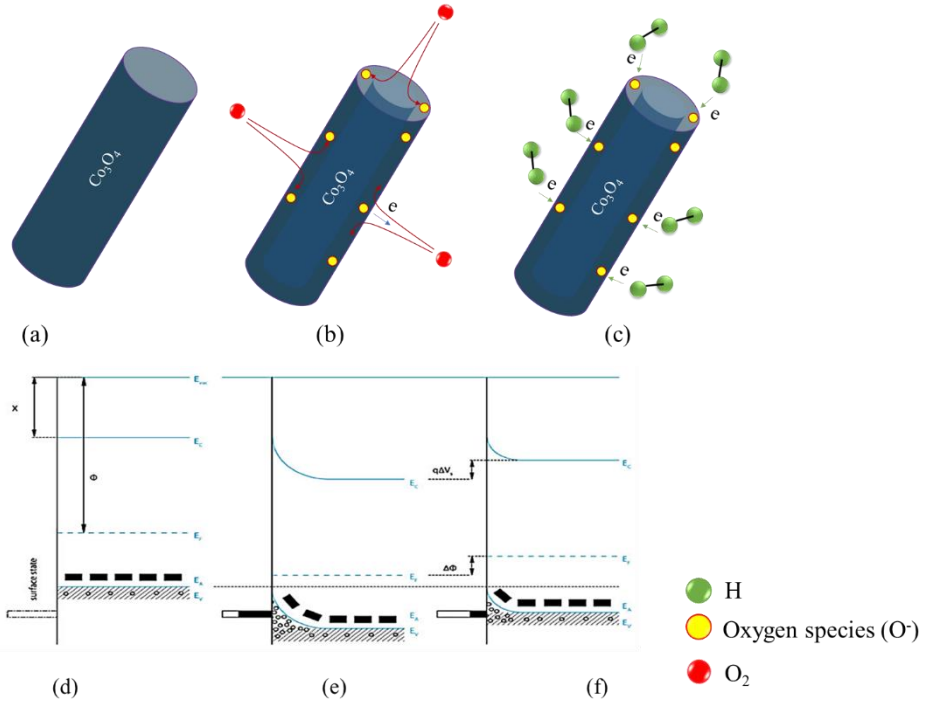

Figure 4.34. Schematic of the formation of the hole accumulation layer:(a) before exposure to air, (b) after exposure to air, (c) interaction with H_2, and the band bending: :(c) before exposure to air, (d) after exposure to air, (e) interaction with H_2 of typical p-type Co_3O_4 nanowire.

The gas sensing mechanism in this study is distinct from conventional explanations. It is based on the inversion of conductivity from p-type to n-type, caused by thermal energy and lattice oxygen's involvement in H_2 oxidation, resulting in the formation of oxygen vacancies (equation 4.15).

$$2H_2(g) + O_2^-(g) \rightarrow 2H_2O(g) + e^- \quad (4.13)$$

$$H_2(g) + O^-(ad) \rightarrow H_2O(g) + e^- \quad (4.14)$$

$$O_O^x \rightarrow \frac{1}{2}O_2 + V_{\ddot{O}} + 2e' \quad (4.15)$$

The inversion of the sensor signal from p-type to n-type conductivity occurs when the electron concentration surpasses the hole concentration on the surface of Co_3O_4, making electrons the main charge carriers [49]. When the surface layer of Co_3O_4 has more electrons [n] than holes [p], electrons become the main charge carriers, leading to a change in conductivity type from p-type to n-type and an inverted sensor signal, making the sensor act as an n-type material. The interaction of H_2 with oxygen species increases the number of electrons and conductance. It is also being investigated if the transformation of CoO to Co_3O_4 at the intermediate layer between Co and Co_3O_4 affects the electron concentration on the surface.

4.4 TiO_2 nanobelts for acetone sensing

4.4.1 Material analysis

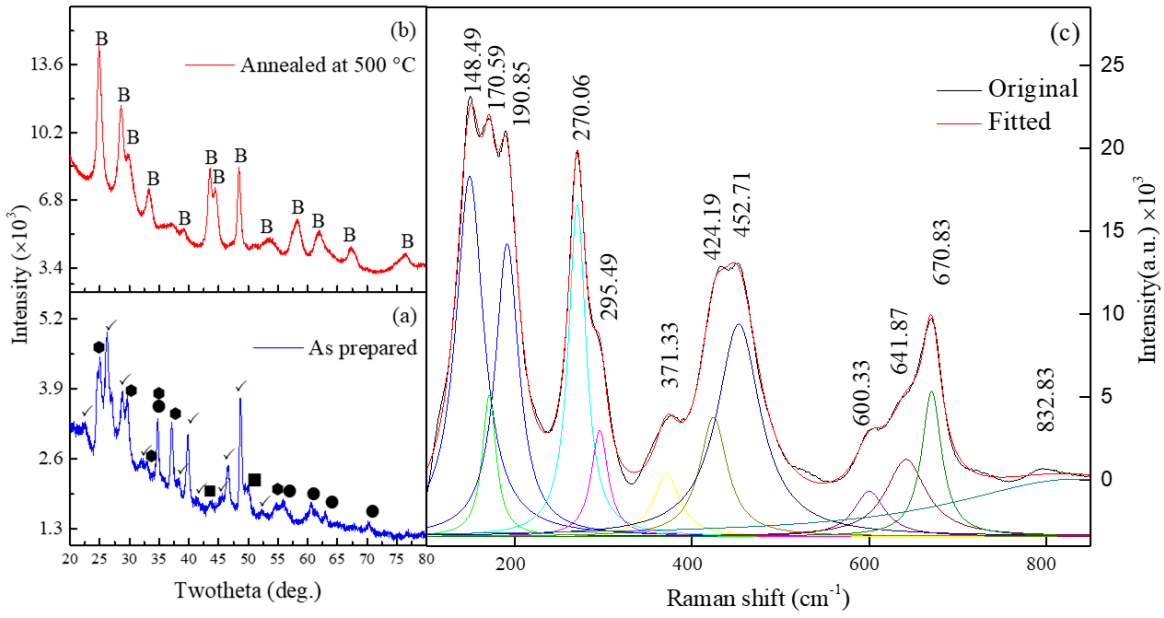

Figure 4.35. XRD patterns of samples: (a) intermediate $H_2Ti_3O_7$, (b) TiO_2-(B), and (c) Raman spectra of the prepared $H_2Ti_3O_7$ at 200 °C before the calcination. B-TiO_2-(B); ✓-$H_2Ti_3O_7$; ●-$Na_2Ti_3O_7$; ■-$Na_2Ti_4O_9$; ⬢-$Na_2Ti_9O_{19}$.

The formation and crystal structure of TiO_2 were studied using X-ray diffraction (XRD) analysis. Figure 4.35 (a) shows the presence of intermediate $H_2Ti_3O_7$ and residual sodium titanate. However, these were eliminated after washing and annealing (Figure 4.35 (b)). $H_2Ti_3O_7$ plays a crucial role in the final product's nanobelt-like morphology through the Dissolution-Recrystallization process. The diffusion of OH^- ions into anatase TiO_2 leads to Ti–O–Ti bond dissolution and exfoliation of single-layered TiO_6 octahedra sheets (nanosheets). This is the cause of characteristic vibrational peaks in the Raman spectrum at 280 cm^{-1} (Ti–O–Na), 372 cm^{-1} (Ti–O–Ti), and 670.8 cm^{-1} (TiO_6) as shown in Figure 4.35 (c). The diffraction peaks in Figure 4.35 (b) at two theta value of 24.98°, 28.59°, 29.79°, 33.41°, 39.47°, 43.48°, 44.61°, 48.66°, 52.89°, 58.47°, 62.38°, 67.27°, and 76.69° are, respectively, assigned to the reflections of the (110), (002), (40-1), (31-1), (31-2), (003), (60-2), (020),

(113), (71-1), (31-4), (02-3) and (712) of Monoclinic (JCPDs: 98-004-7691, space group C12/m1) TiO_2 -B

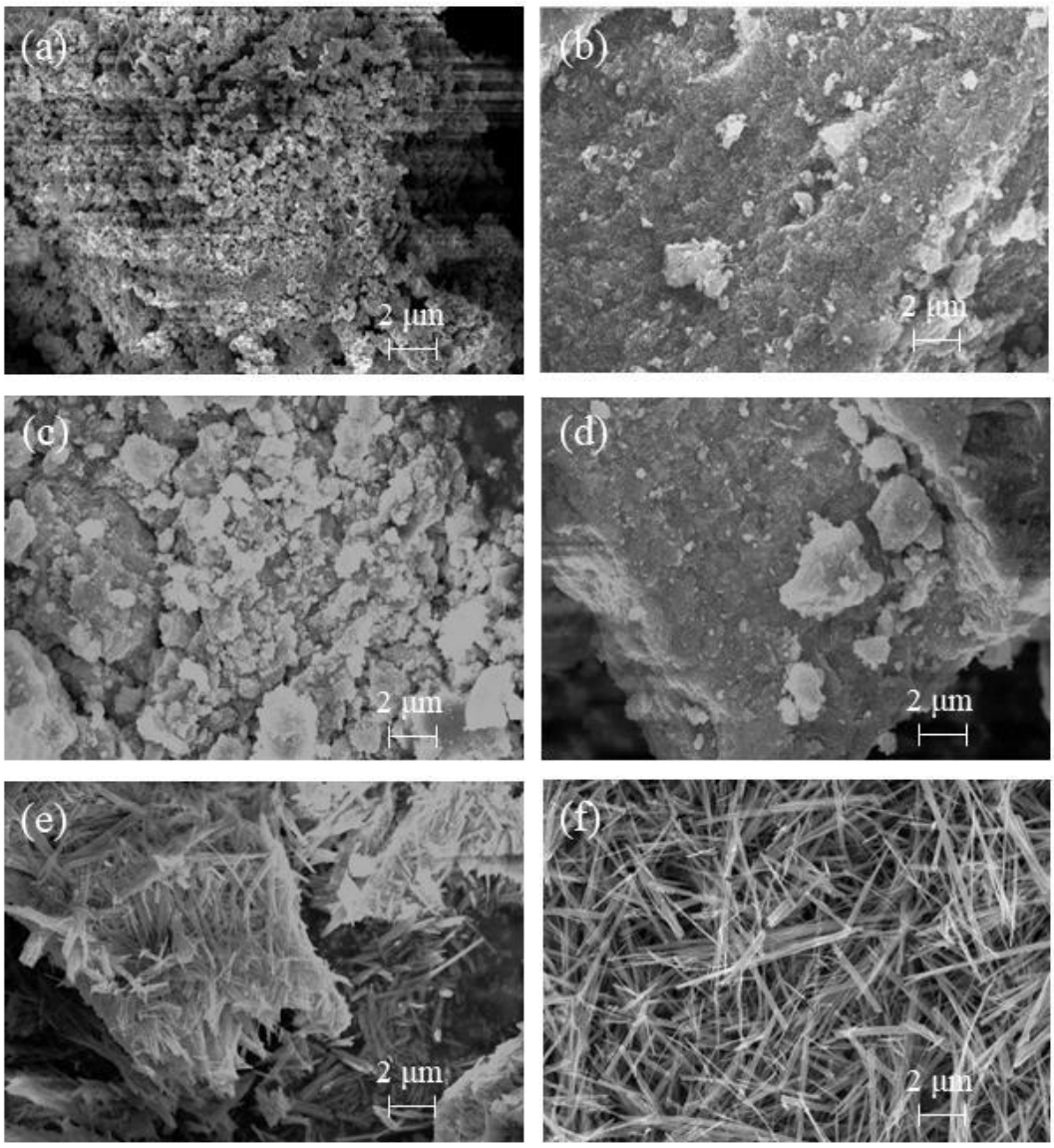

Figure 4.36. FE-SEM images of the obtained morphology at (a) starting anatase TiO_2 powder, (b) hydrothermal treatment at 120 °C, (c) hydrothermal treatment at 135°C, (d) hydrothermal treatment at 125 °C, (e) hydrothermal treatment at 175 °C, (f) hydrothermal treatment at 200 °C.

FE-SEM images in Figure 4.36 (a-f) show intermediate $H_2Ti_3O_7$ structures synthesized through anatase TiO_2 (20-25 nm particle diameter) dissolution in NaOH solution and ion-exchange with acetic acid. Hydrothermal treatment at 120 °C results in compact thick flake-like anatase particles (Figure 4.36 (b)), which become large aggregated particles at 135 °C

(Figure S1(c)), and a compact film-like morphology at 150 °C (Figure 4.36 (d)). Further hydrothermal treatment at 175 °C and 200 °C transforms the anatase into belt-like shapes (Figure 4.36 (e-f)). The 200 °C treatment results in compact and low aspect ratio nanobelts, which were studied further. Figure 4.37 (a,b) shows the FE-SEM of the grown TiO_2 nanobelts at 200 °C and annealed at 500 °C.

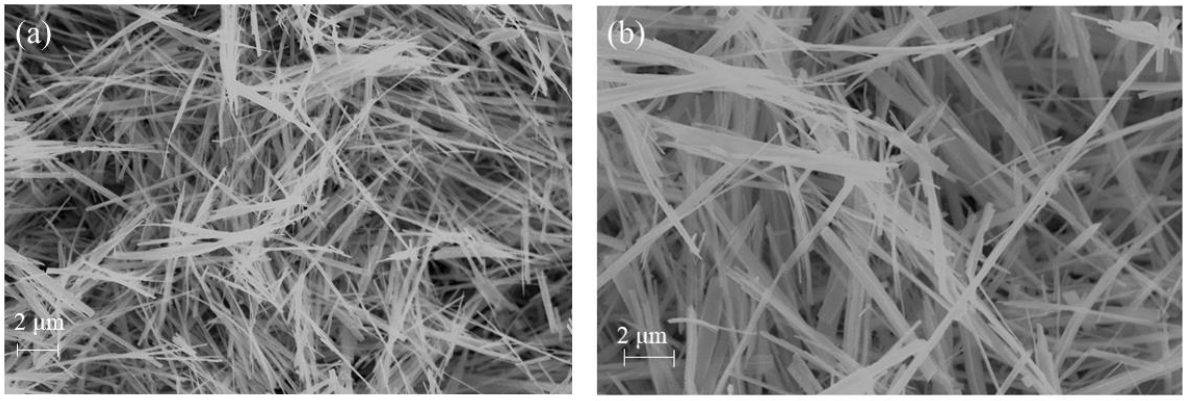

Figure 4.37. FE-SEM of the (a) $H_2Ti_3O_7$ was prepared in the autoclave at 200 °C, and (b) TiO_2-(B) was annealed at 500 °C.

Figure 4.38 (a) displays a one-dimensional nanobelt structure in intermediate $H_2Ti_3O_7$ using a conventional TEM (CTEM), which is ten micrometers in length. Figure 4.38 (b) shows the TiO_2 nanobelts after annealing at 500 °C using CTEM. The HRTEM image in Figure 4.38 (c) with its insert confirms the well-crystallized nanobelts, displaying the (101) planes typical of anatase. The Selected Area Electron Diffraction (SAED) in Figure 4.38 (d) confirms the presence of crystallographic planes (101), (200), (105) of TiO_2-(B) with lattice parameters a=b=3.785 Å, c=9.514 Å, $\alpha=\beta=\gamma=90°$ and formation of nanobelts in the c-axis direction (CIF number 9009086). Figures 4.38 (e, f) reveal a "porous-like" morphology in certain regions of TiO_2-(B) due to structural defects in specific areas along the nanobelts.

EDS spectra were taken on the TEM grid to analyze the elemental distribution on the surface of TiO_2-(B) nanobelts. The EDS maps in Figure 4.39 (a-c) display the presence of Ti and O elements on the nanobelt surface. Notably, Figure 4.39 (a-d) shows some nanobelts overlapping, which significantly improves the sensor's response in gas sensing [85].

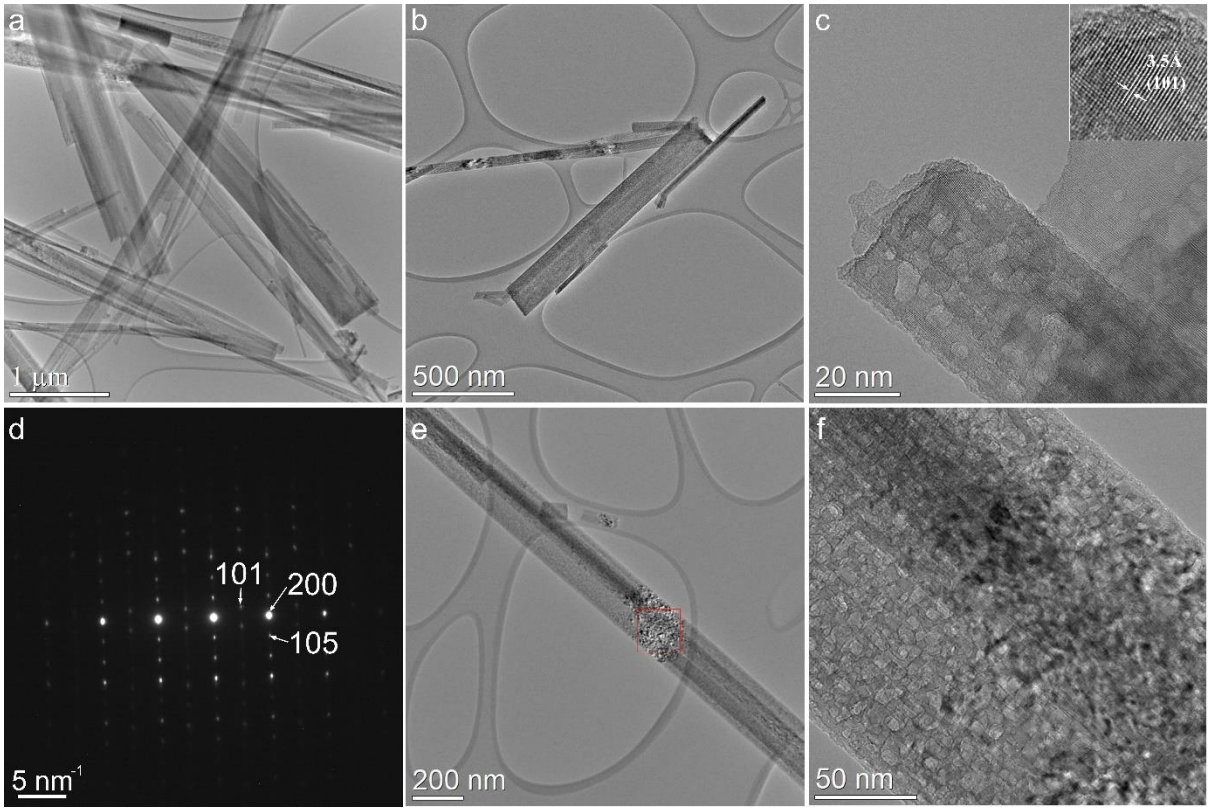

Figure 4.38. CTEM images: (a) $H_2Ti_3O_7$, (b) TiO_2-(B) and (e) formation of pores-like structure in TiO_2-(B); (c) HRTEM image of TiO_2-(B) with insert showing (101) planes; (d) SAED of TiO_2-(B).

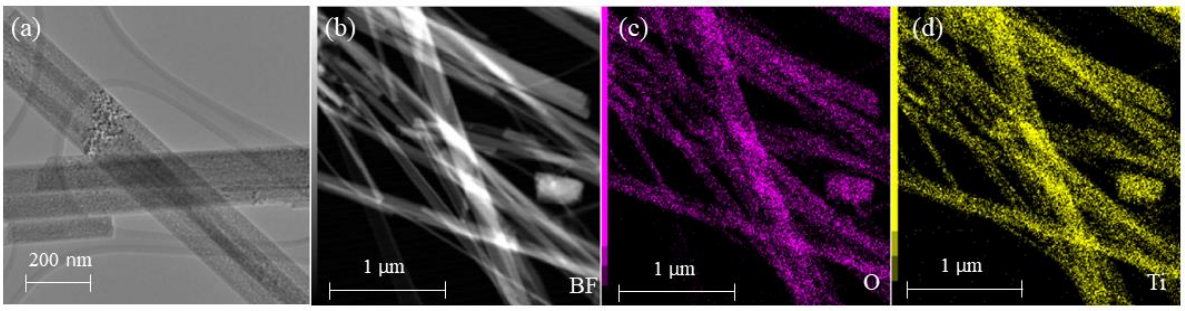

Figure 4.39. (a) CTEM of several overlapping TiO_2-(B) nanobelts; EDS analysis of TiO_2-(B) nanobelts. The maps show the (c) O and (d) Ti distribution on the nanobelts corresponding to the HAADF image of (b).

4.4.2 Gas sensing analysis

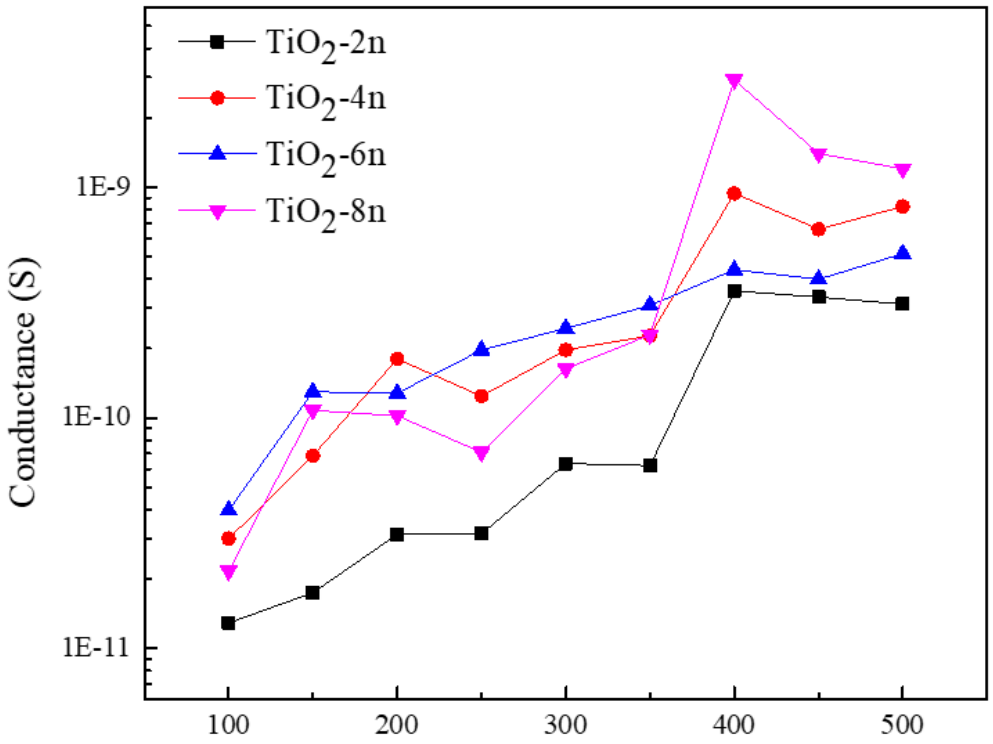

Figure 4.40. Electrical conductance variation of the fabricated TiO_2 nanobelts sensors at different working temperatures at 40 RH% conditions.

Figure 4.40 shows the temperature effect on the conductance of the TiO_2-(B) sensors. The conductance increases with temperature due to the semiconducting nature of the TiO_2-(B) material. Among the sensors, TiO_2-8n showed the highest conductivity at 400 °C [86]. In gas sensing tests, the highest response was recorded at 400 °C with the TiO_2-8n sensor exhibiting the highest sensitivity to acetone compared to other sensors. Further analysis was focused on the TiO_2-8n sensor. Further analysis was conducted on the TiO_2-8n sensor due to its highest response towards acetone in the gas sensing studies performed at various operating temperatures, where the highest conductivity was observed at 400 °C.

The gas sensing performance of TiO_2-8n devices towards H_2, CH_4, NO_2, C_2H_5OH, and C_3H_6O at temperatures from 100 to 500 °C (incremented by 50 °C) was investigated. The sensors showed typical n-type semiconducting behavior with increased electrical conductance upon exposure to reducing gases and returning to initial values when the gas flow was cut off. The literature shows that the working temperature affects gas interaction with the sensor until a certain catalytic temperature, then influences the response value. Thus, the optimum

working temperature plays a critical role in the performance of metal oxide gas sensors [87,88]. Usually, working temperature affects the gas interaction with the sensor up to a certain catalytic temperature and then hinders the interaction modulating the response value. Therefore, metal oxide gas sensors have different response values depending on their working temperature. Thus, investigating the optimum working temperature is significantly important when concerning the performance of the sensors.

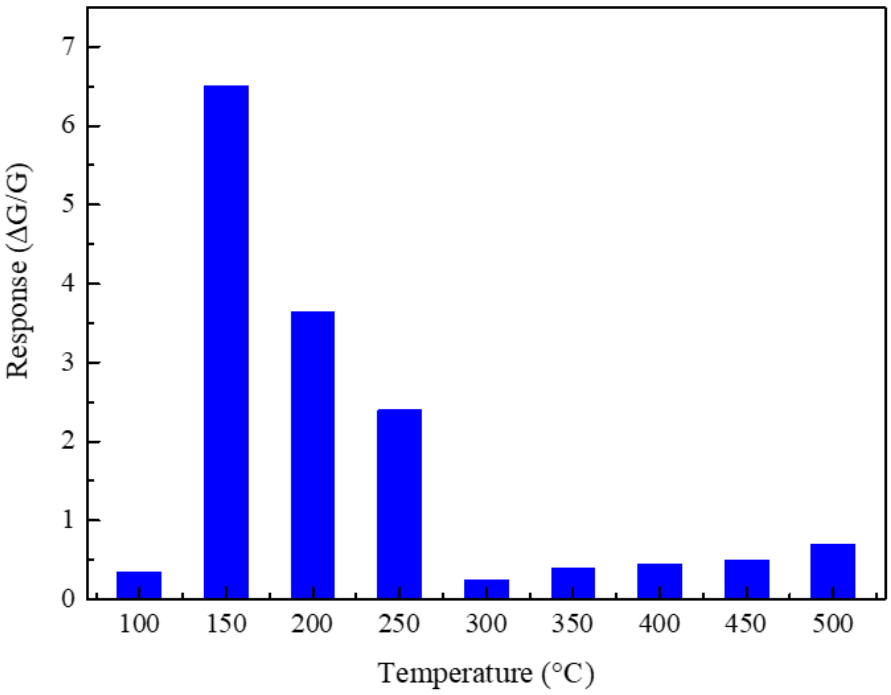

Figure 4.41. Response of the TiO_2 nanobelts (TiO_2-8n) to 10 ppm C_3H_6O at different working temperatures in 40% RH conditions.

The response of the TiO_2-8n sensor to 10 ppm of acetone (C_3H_6O) at various operating temperatures is displayed in Figure 4.41. The sensor displayed the strongest response at 150 °C. Figure 4.42 illustrates the dynamic response of the TiO_2-8n sensor to various concentrations of acetone at 150 °C. Usually, TiO_2-based gas sensors operate at high temperatures (>200°C). However, the low operating temperature of the fabricated sensors could be due to the high catalytic property of the TiO_2-(B), as seen in the conductance variation of the sensors [89]. Also, porous regions in the nanobelts encourage the oxygen adsorption/desorption mechanism. Accordingly, the porous-like region of the prepared nanobelts can potentially be one of the reasons for high response in low working temperatures [90,91].

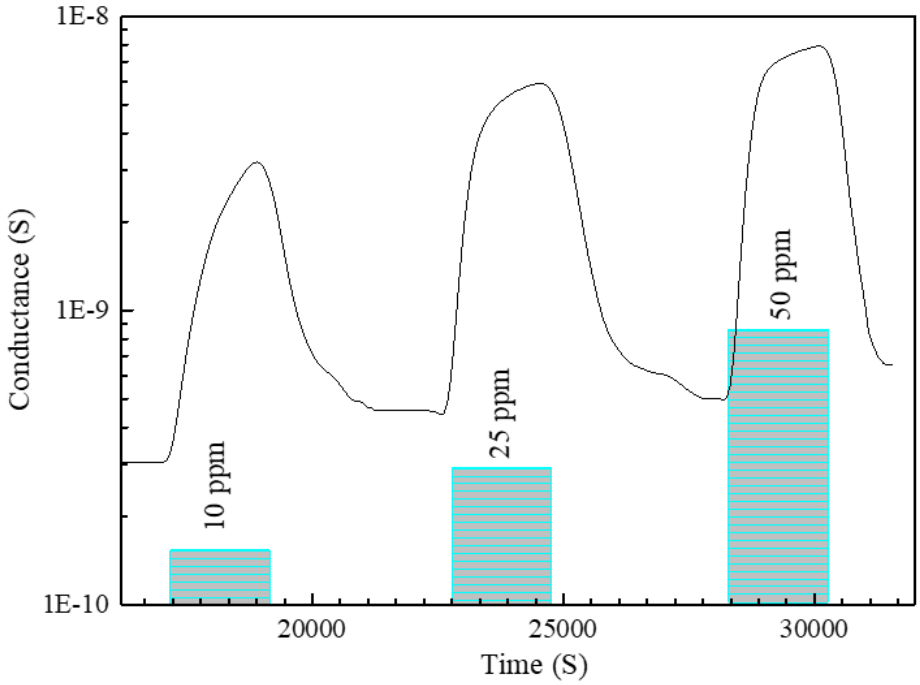

Figure 4.42. Dynamic response-recovery plot of the TiO_2-8 sensor toward 10, 25 and 50 ppm of C_3H_6O at the working temperature of 150 °C.

The response of the structures improves as the concentration of C_3H_6O increases (Figure 4.43). A higher gas concentration leads to more interactions with the surface, leading to a stronger response [92]. The porosity of the nanostructures may contribute to quick gas adsorption and diffusion within the sensor, resulting in a response and recovery time of 348 s and 600 s at 40% relative humidity for 10 ppm C_3H_6O. These results are presented in Table 4.6.

The detection limit of the gas sensing material plays a crucial role in responding to small quantities of targeted gas and avoiding potential hazards in a polluted environment. The power fitting relationship (y=6.4492x0.6046) between response and concentration (Figure 4.44 (a)) is crucial, where the slope indicates sensitivity and the intercept shows the detection limit. The fabricated sensors (Figure 4.44 (b)) have a favorable response with a detection limit of around 0.05 ppm ($\Delta G/G = 1$ in power fitting). In practical use, the sensor's reproducibility and stability of response are also critical factors to consider.

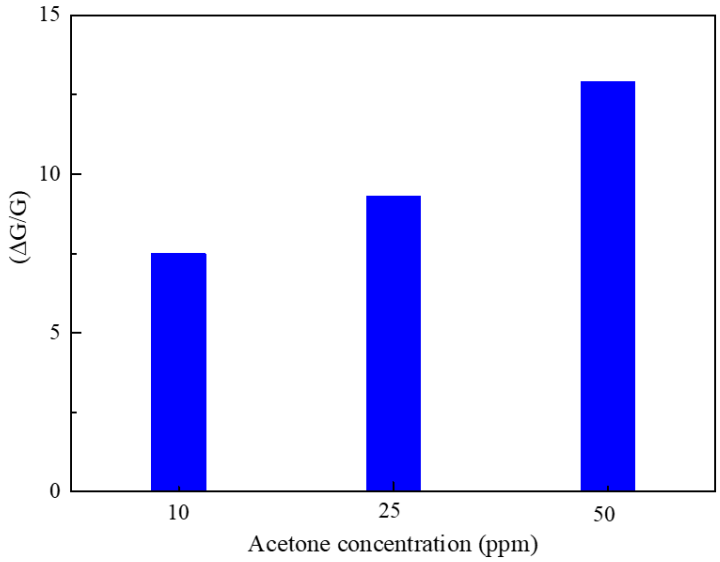

Figure 4.43. Variation of the TiO_2 sensor's response toward different concentrations of C_3H_6O at the working temperature of 150 °C.

Table 4.6. Sensors' performance to different concentrations of C_3H_6O.

C_3H_6O (ppm)	40 RH%			
	Response	Response	Response time (S)	Recovery time (S)
10	1.3	6.5	378	600
25	2.1	9.6	348	960
50	4.4	12.7	324	1320

Thus, the reproducibility and stability of the TiO_2-(B) nanobelts were evaluated towards acetone (C_3H_6O). Figure 4.45 shows the response of the sensor for three consecutive cycles of 50 ppm C_3H_6O at 150 °C and 40% RH. The results indicate consistent response values. The stability of the sensor is shown in Figure 4.46, where it holds its response well for two weeks towards 50 ppm C_3H_6O at 150 °C and 40% RH. Figure 4.47 displays the response of the TiO_2-8n sensor to various gases and working temperatures. Moreover, Figure 4.44 (b) demonstrates the selectivity of the TiO_2-8 sensors to 10 ppm C_3H_6O, 10 ppm ethanol (C_2H_5OH), 100 ppm hydrogen (H_2), 100 ppm methane (CH_4), and 1 ppm nitrogen dioxide (NO_2) at a working temperature of 150 °C.

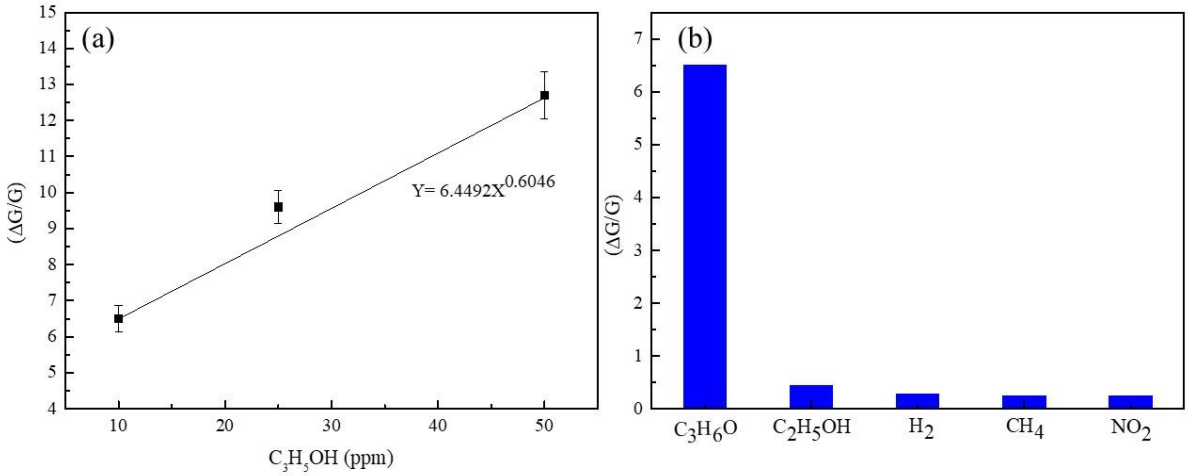

Figure 4.44. (a) The plot of response vs concentration value of the sensor (TiO_2-8n) toward the C_3H_6O at 150 °C, (b) Selectivity of the TiO_2-8n sensor toward tested gases (10 ppm C_3H_6O, 10 ppm C_2H_5OH, 100 ppm H_2, 100 ppm CH_4 and 1ppm NO_2) in 40 RH% humidity air at the operating temperature of 150 °C.

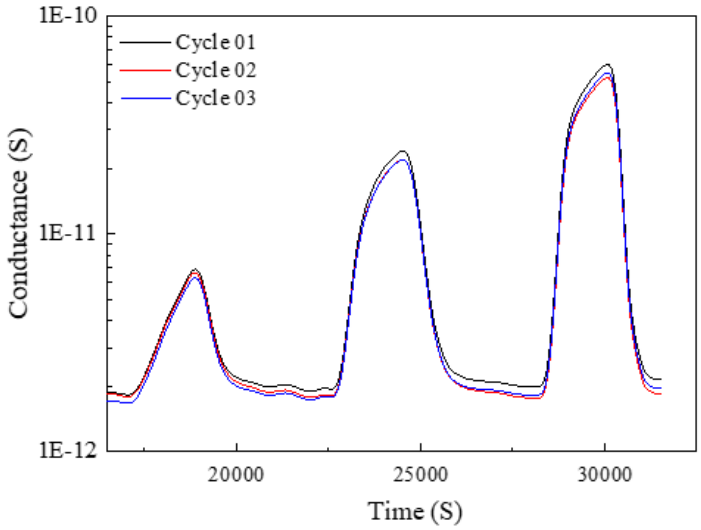

Figure 4.45. Reproducibility study of TiO_2-B nanobelts sensor toward 50 ppm C_3H_6O at 150 °C at 40 RH%.

Therefore, the C_3H_6O sensing abilities of TiO_2-B nanobelts, such as response, selectivity, response/recovery times, reproducibility, and stability, make it a viable option for selective C_3H_6O sensing in various applications based on the literature survey shown in Table 4.7.

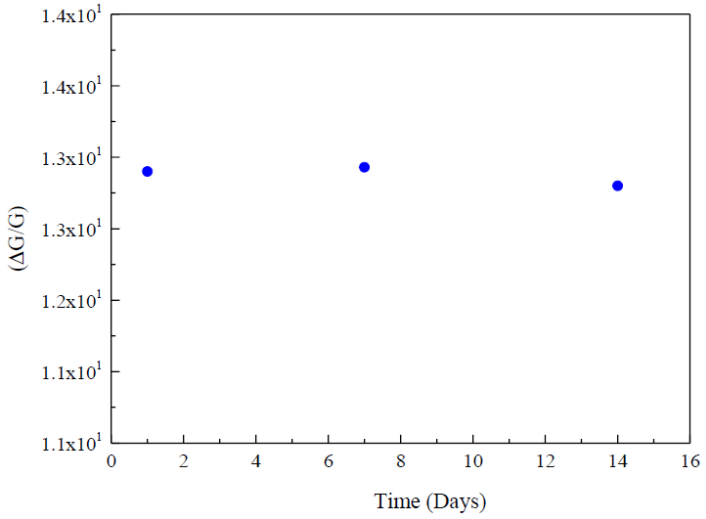

Figure 4.46. Stability study of TiO_2-B nanobelts sensor toward 50 ppm C_3H_6O at 150 °C in both dry and 40 RH%.

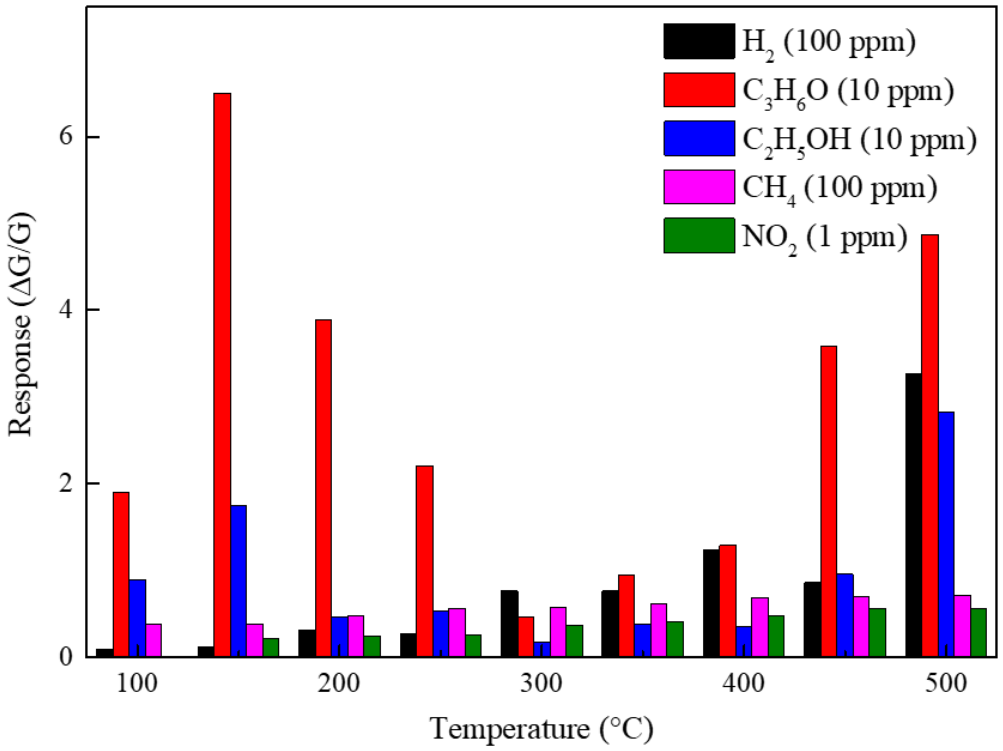

Figure 4.47. Response values of the sensor towards 500, 100, 10, 10, and 10 ppm of CH_4, H_2, NO_2, C_2H_5OH, and C_3H_5OH.

Table 4.7. Comparison of gas sensing parameters of TiO_2-B nanobelts sensor with other reported TiO_2-based C_3H_6O sensors.

Material	Synthesis route	Working tempt. (^oC)	Response (R_a/R_g)	C_3H_6O (ppm)	Res. Time (T_{res}) (s)	Rec. Time (T_{rec}) (s)	The lowest detection limit (ppm)	Reference
TiO_2 porous NPs	Hydrothermal	275	13.9	100	11	14	-	[93]
TiO_2 NPs	Matrix-assisted pulsed laser deposition	400	6	100	240	-	20	[94]
Nanoporous TiO_2	Hydrothermal	370	25.97	500	13	8	20	[95]
Ag-TiO_2 nanobelts	Hydrothermal	260	28.25	500	6	8	0.8	[96]
TiO_2 nanorods	Electrospun	500	13	300	12	6	-	[97]
TiO_2-B nanorods	Hydrothermal	320	2.3	100	3	180	-	[98]
TiO_2-B nanobelts	Hydrothermal	150	12.7	50	324	1320	0.7	This work

4.4.3 Working mechanism

Typically, the gas sensing mechanism of TiO_2-(B) nanobelts is enhanced by surface reactions and charge transfer from analyte gas adsorption. It relies on two key interactions: oxygen adsorption and interaction between the surface of TiO_2 nanobelts and C_3H_6O. The mechanism involves adsorption of oxygen onto the exposed surface of TiO_2-(B) nanobelts [99]. Accordingly, the resistance increases as shown in Figure 4.48 (a) [100].

When the sensor is exposed to acetone, it interacts with adsorbed oxygen molecules. The interaction with O_2^- is particularly significant at the optimum working temperature of 150 °C. This interaction results in the decomposition of C_3H_6O into CO_2 and H_2O is given in Equations 4.16-4.17 [99]. This releases electrons (e^-), reducing the depletion layer and lowering the sensor's resistance (Figure 4.48(b)).

$$CH_3COCH_{3(gas)} \leftrightarrow CH_3COCH_{3(ads)} \tag{4.16}$$

$$CH_3COCH_{3(ads)} + 8O^-_{(ads)} \rightarrow 3CO_{2(gas)} + 3H_2O_{(gas)} + 8e^- \tag{4.17}$$

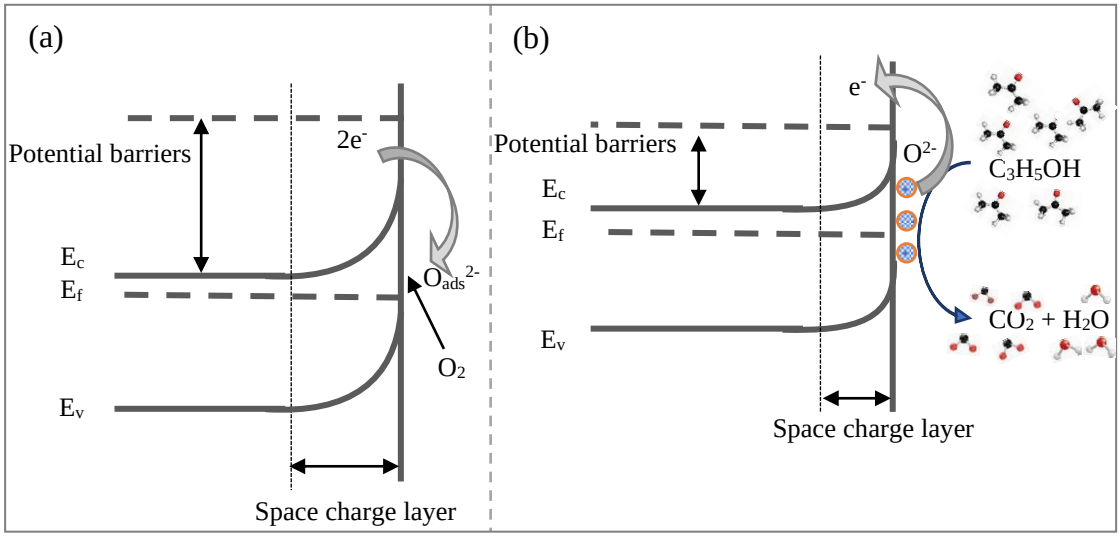

Figure 4.48. (a) electrical band bending due to the adsorption of oxygen species to the TiO_2 nanobelt surface ($O_2^-{}_{ads}$, $O^-{}_{ads}$, $O^{2-}{}_{ads}$), (b) reduction of the space charge region resulting in a decrement in the electrical resistance due to the interaction between the acetone molecules and TiO_2 surface. Where E_c is the conduction band, E_v is the valence band, and E_f is the Fermi level.

4.5 Nb_2O_5 Microcolumns

4.5.1 Material analysis

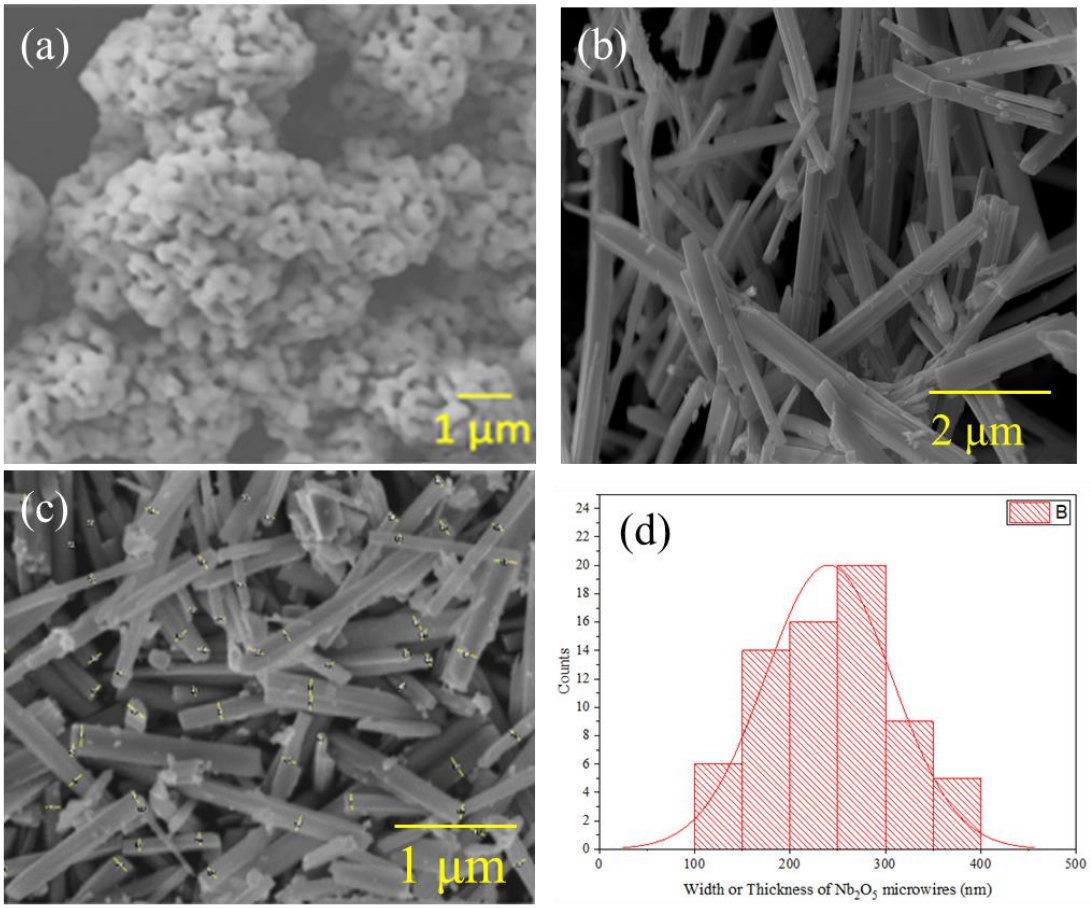

Figure 4.49. FE- EM images of (a) commercial Nb_2O_5 powder, (b) Nb_2O_5 microcolumns, (c), (d) measurement of with and length of the prepared Nb_2O_5 microcolumns.

The FE-SEM images in Figure 4.49 (a,b) display the morphological change of Nb_2O_5 powder during a hydrothermal reaction at 180 °C for 30 minutes. The Nb_2O_5, with a particle size under 45 µm, reacts rapidly with 10 $mol.dm^{-3}$ NaOH in a hydrothermal environment and after 30 minutes, high-purity niobate microcolumns are produced. Figure 4.49 (c,d) confirms that the resulting Nb2O5 has a length in the tens of micrometers, width and height in the hundreds of nanometers.

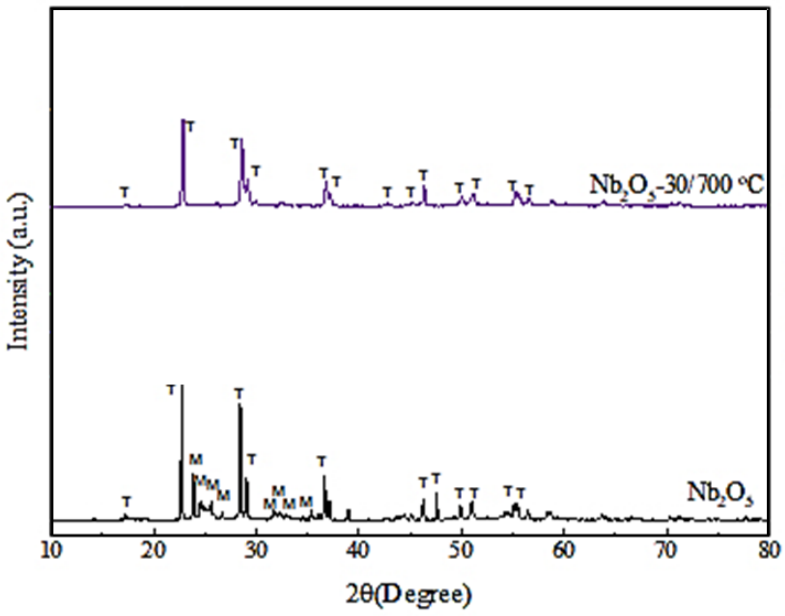

Figure 4.50. XRD diffractogram of the row Nb_2O_5 and prepared Nb_2O_5 microcolumns.

The reported XRD of pure Nb_2O_5 (Figure 4.50) consists of both orthorhombic (JCPDS card no: 00-27-1313) and monoclinic (JCPDS card no. 01-072-1121) phases. However, when the prepared material was calcinated, around 700 °C, the crystal structure has been transformed to orthorhombic phase (JCPDS No. 00-030-0873).

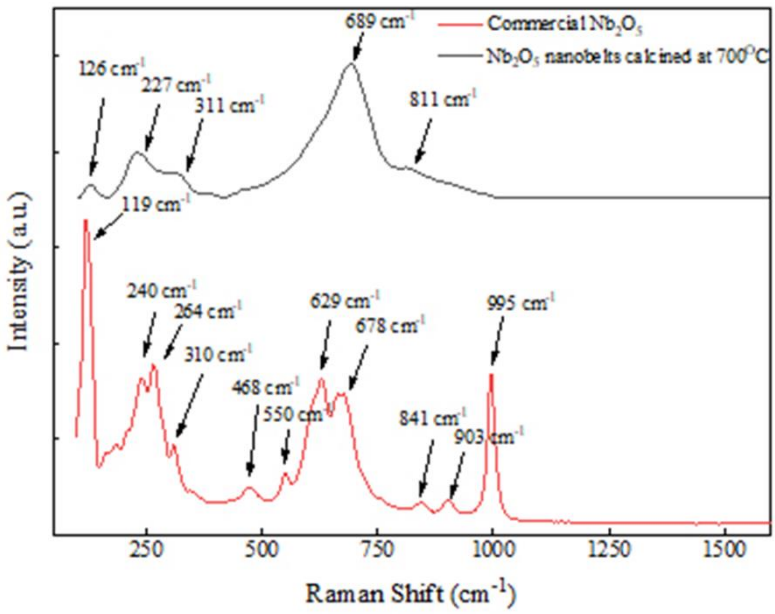

Figure 4.51. Raman spectra of commercial Nb_2O_5 and synthesized Nb_2O_5 microcolumns.

Figure 4.51 (in red) presents the Raman spectra of commercial niobium oxide powder. The monoclinic phase of the commercial Nb_2O_5 is identified by its unique 995 cm^{-1} Raman band [101,102]. Other peaks at 227 and 311 cm^{-1} represent Nb-O-Nb bonds, and the 678 cm^{-1} peak represents Nb-O bond stretching modes, confirming an orthorhombic phase [103,104]. Raman bands at 264 and 306 cm^{-1} are from Nb-O-Nb bending modes in the orthorhombic phase [103]. The absence of the 995 cm^{-1} Raman band confirms that the niobium oxide microwires are solely in the orthorhombic phase.

4.5.2 Gas sensing analysis

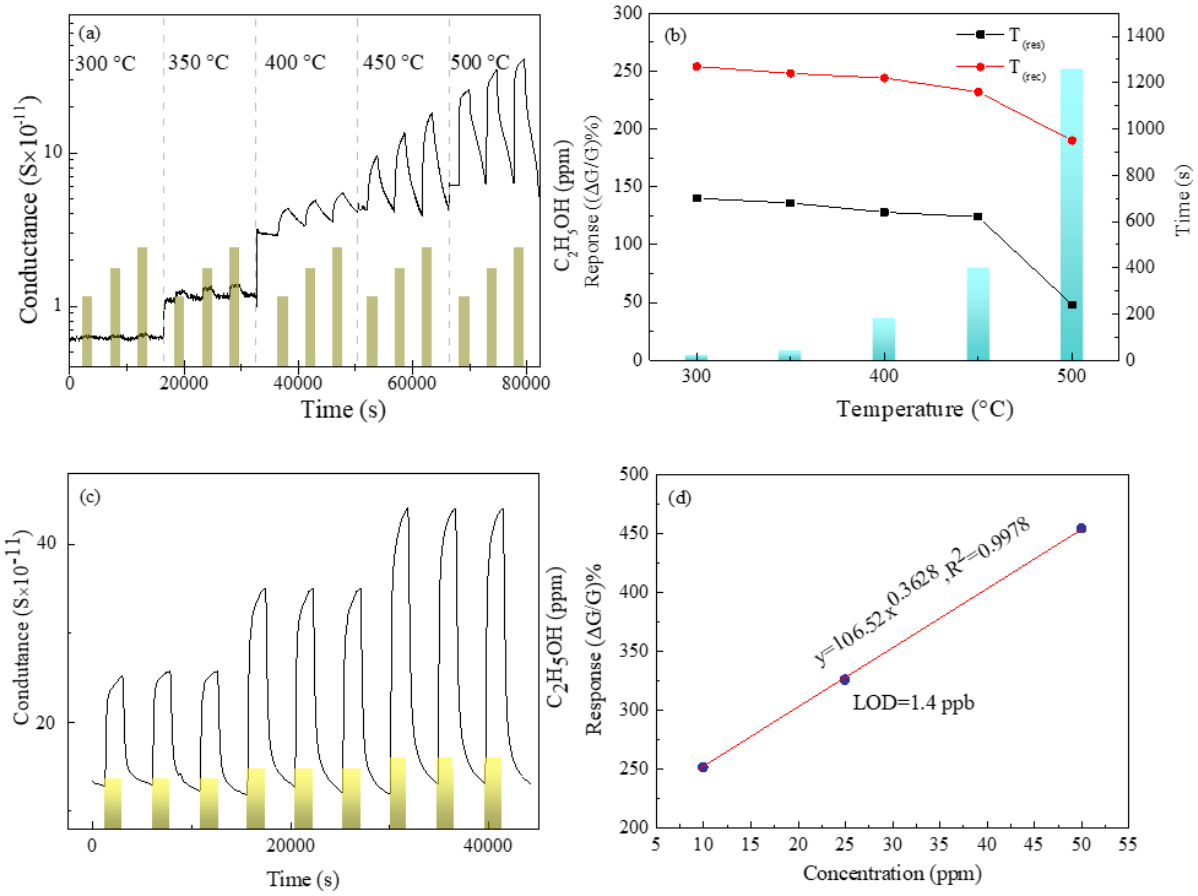

Figure 4.52. Gas sensing functionality of the Nb_2O_5 microcolumns (a) dynamic response to ethanol at 300-500 °C, (b) response value, response/recovery times, (c) repeatability of the sensors signal at 500 °C, (d) modified power fitting.

Figure 4.52 (a) displays the dynamic response of the chemiresistor ethanol sensors to 10, 25, and 50 ppm ethanol in air. The conductance of all the sensors increases when exposed to ethanol. However, the response is not significant below 350 °C because of the adsorption or reduction reaction of ethanol on the Nb_2O_5. The increase in conductance confirms that the Nb_2O_5 microcolumns are n-type with electrons as the dominant charge carrier. The sensors show clear recovery after ethanol is cleared from the test chamber. Response ((ΔG/G)%) and response/recovery times (time to reach 90% change in response during full response and recovery) are used to evaluate sensor performance. Figure 4.52 (b) shows that higher sensor response and faster response and recovery times are achieved when the sensors operate at 500 °C in dry air. The study showed that a higher concentration of adsorbed ethanol molecules and oxygen species with rising temperatures can impact the temperature-dependent sensing response. The highest response recorded was 251.23% with a response time of 240 seconds and a recovery time of 950 seconds when detecting 10 ppm ethanol. Note, the system requires 5 minutes to exchange its 1L environment with a flow rate of 200 sccm. Furthermore, the response and recovery times were found to decrease with an increase in operating temperature. At optimal temperature, the system demonstrated complete recovery and excellent repeatability, making it suitable for practical use and eliminating baseline drift problems (Figure 4.52(c)). A comparison of ethanol sensors is summarized in Table 4.8.

Table 4.8. The comparison of ethanol sensing performances of MOXs.

Materials	Methods	Temp. (°C)	Ethanol (ppm)	Resp.	Ref.
Au/SnO_2	Hydrothermal	340	100	18	[105]
ZnO Nanowires	Oxidation	240	100	5	[106]
NiO/ZnO	VLS	400	50	6.7	[107]
Nb_2O_5-TiO_2 nanofibers	Electrospinning	250	500	21.64	[108]
CuO-Fe_2O_3 hollow spheres	Template method	380	500	17.5	[109]
Nb_2O_5 microcolumns	Hydrothermal	500	10	2.51	This work

The performance of the sensor was further examined, considering factors such as selectivity, long-term stability, detection limit (LOD), and stability in humidity. The sensor response

exhibited a linear relationship with ethanol concentration (Figure 4.52 (d)), with a correlation coefficient (R^2) of over 0.99 for the power-fitting ($y=a.x^b$) model, indicating a strong fit between the experimental data and the linear model. The LOD was calculated using the 10% method, demonstrating the sensor's ability to detect ethanol at 1.4 ppb when operating at 500 °C. Additionally, the sensors demonstrated good selectivity in ethanol sensing (251.53) compared to CO (9.04), CO_2 (49.65), NO_2 (34.01), H_2 (113.55), H_2S (159.79), and C_3H_6O (89.8), as shown in Figure 2 (a).

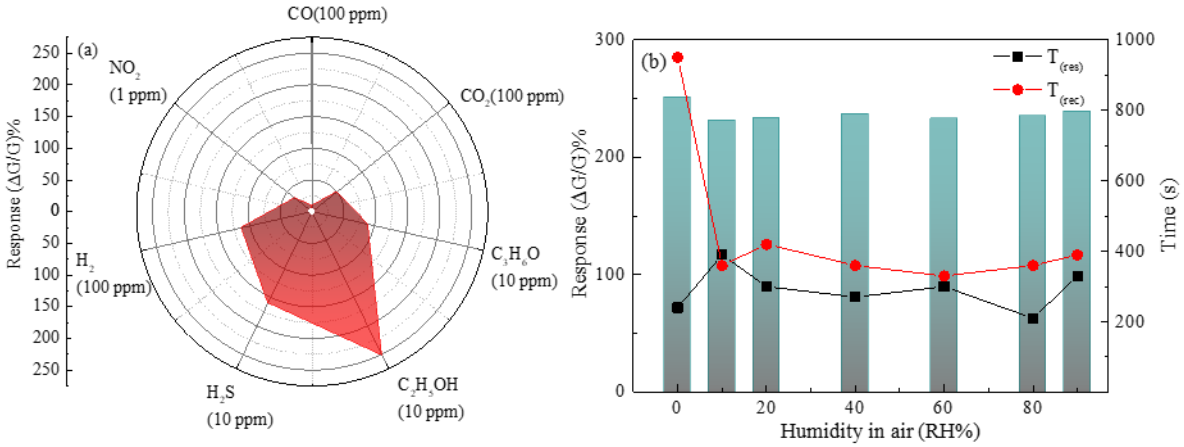

Figure 4.53. Selectivity of the Nb_2O_5 sensors towards C_2H_5OH (10 ppm) compared to CO (100 ppm), CO_2 (100 ppm), NO_2 (1 ppm), H_2 (100 ppm), H_2S (10 ppm), and C_2H_5OH (10 ppm) at 500 °C in dry air, (b) humidity dependent response, response/recovery time towards 10 ppm C_2H_5OH.

The study also evaluated the effect of relative humidity on the sensor's ability to detect ethanol at different humidity levels (0-90%). Results showed no major change in response to 10 ppm ethanol at 500 °C, but a 41% decrease in baseline conductance with 10% RH. The baseline conductance remained unchanged even with 90% RH. These findings are displayed in Figure 2(b). Water molecules can absorb onto the MOXs through physisorption (at high RH%) or chemisorption (at low RH%), hindering gas sensing and baseline conductance [3]. In this context, resistance changes occur due to hydroxyl ions and mobile protons generated from water molecule adsorption on the MOX surface (active sites). Hydroxyl ions bond with metal cations while mobile protons (hydrogen ions) attach to oxygen on the MOXss surface, creating more hydroxyl ions. This affects the electrical conductance baseline depending on

hydroxyl ion and oxygen molecule levels. High humidity results in water molecule absorption through proton transfer, forming H_3O^+ at the MOX surface and causing fluctuating electrical conductance. The study found no significant decrease in baseline conductance at high humidity compared to low humidity, likely due to high operating temperature. Although humidity changes, response time remained constant, but recovery time decreased by 59% compared to dry conditions. This quick recovery may be due to the formation of $C_2H_5OH_2^+.(H_2O)$ with low ionic diffusion coefficient [108,110].

4.5.3 working mechanism

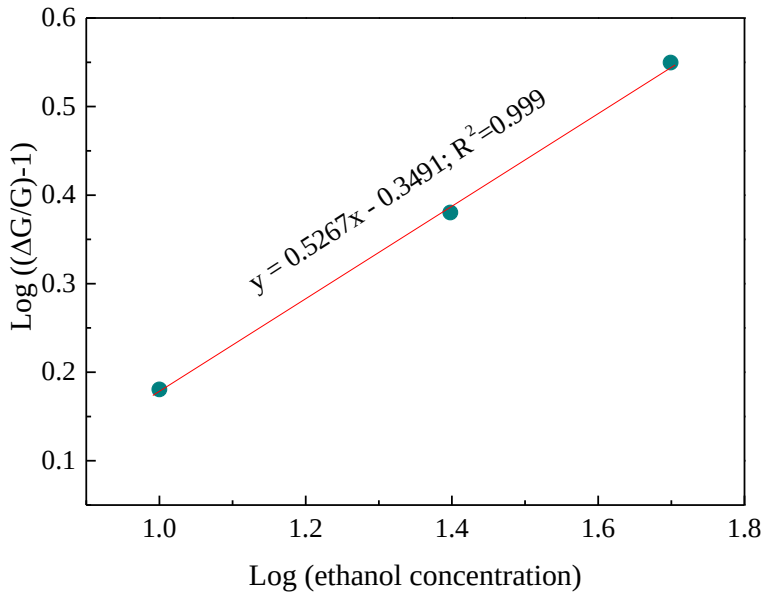

Figure 4.54. The plot of log(S_g-1) vs log(C_g).

The Nb_2O_5 surface contains an electron depletion layer (EDL) due to oxygen species that trap electrons in the Nb_2O_5 conduction band during the reduction of O_2- O^-. Understanding the specific oxygen species absorbed on the Nb_2O_5 surface is important.

The relationship between gas concentration (C_g) and response (S_g) is a well-known concept.

$$S_g = 1 + a.C_g^a \qquad (4.22)$$

Where, the perfector and surface species charge parameters are represented by a and b, respectively. The value of b equals 0.5 or 1, indicating the absorbed oxygen ions on the

surface to be either O^{2-} or O^{-} [111]. By taking the logarithm on either side of Eq. (1) we can gain another equation that can be written as,

$$\log (S_g\text{-}1) = \log(a) + b.\log(C_g) \quad (4.23)$$

Figure 4.54 displays a $\log(S_g\text{-}1)$ vs $\log(C_g)$ plot. The fit is linear with a correlation coefficient exceeding 0.999. Thus, our study concludes the dominant oxygen species to be O^{2-}. This leads to a redox reaction on the Nb_2O_5 surface between O^{2-} and C_2H_5OH upon exposure to C_2H_5OH, resulting in oxidation as follows

$$C_2H_5OH\ (ads) + 6O^{2-}\ (ads) \rightarrow 3H_2O\ (g) + 2CO_2\ (g) + 12e^{-} \quad (4.24)$$

As a result, when C_2H_5OH interacts with the oxygen species, the release of trapped electrons back to the conduction band of Nb_2O_5 causes an increase in conductance.

References

[1] Zhang, Liang, Xiaoyan Jing, Jingyuan Liu, Jun Wang, and Yanbo Sun. “Facile Synthesis of Mesoporous Zno/Co_3O_4 Microspheres with Enhanced Gas-Sensing for Ethanol.” Sensors and Actuators B: Chemical 221 (2015): 1492–98. https://doi.org/10.1016/j.snb.2015.07.113.

[2] Ghamgosar, Pedram, Federica Rigoni, Mojtaba Gilzad Kohan, Shujie You, Edgar Abarca Morales, Raffaello Mazzaro, Vittorio Morandi, Nils Almqvist, Isabella Concina, and Alberto Vomiero. “Self-Powered Photodetectors Based on Core–Shell Zno–Co_3O_4 Nanowire Heterojunctions.” ACS Applied Materials & Interfaces 11, no. 26 (2019): 23454–62. https://doi.org/10.1021/acsami.9b04838.

[3] Moumen, Abderrahim, Dario Zappa, Nicola Poli, and Elisabetta Comini. “Catalyst – Assisted Vapor Liquid Solid Growth of α-Bi_2O_3 Nanowires for Acetone and Ethanol Detection.” Sensors and Actuators B: Chemical 346 (2021): 130432. https://doi.org/10.1016/j.snb.2021.130432.

[4] Steinhauer, S., E. Brunet, T. Maier, G.C. Mutinati, and A. Köck. “Suspended Cuo Nanowires for Ppb Level H^2S Sensing in Dry and Humid Atmosphere.” Sensors and Actuators B: Chemical 186 (2013): 550–56. https://doi.org/10.1016/j.snb.2013.06.044.

[5] Moumen, Abderrahim, Navpreet Kaur, Nicola Poli, Dario Zappa, and Elisabetta Comini. “One Dimensional Zno Nanostructures: Growth and Chemical Sensing Performances.” Nanomaterials 10, no. 10 (2020): 1940. https://doi.org/10.3390/nano10101940.

[6] Jiang, Pengjie, Haonan Zhang, Changmiao Chen, Jiaojiao Liang, Yazi Luo, Ming Zhang, and Mengqiu Cai. “Co_3O_4–SnO_2 Nanobox Sensor with a PN Junction and Semiconductor–Conductor Transformation for High Selectivity and Sensitivity Detection of H_2S.” CrystEngComm 19, no. 38 (2017): 5742–48. https://doi.org/10.1039/c7ce01240c.

[7] Bonyani, Maryam, Gun-Joo Sun, Jae Kyung Lee, Seungbok Choi, Chongmu Lee, and Sangmin Lee. “Enhanced Sensitivity and Selectivity of Co_3O_4 Nanoparticle-Decorated SnO_2 Nanowire Sensors to Ethanol Gas.” Journal of Nanoscience and Nanotechnology 17, no. 11 (2017): 8285–90. https://doi.org/10.1166/jnn.2017.15131.

[8] Xiang, Kun, Zhongxin Song, Dan Wu, Xiaohui Deng, Xuewan Wang, Wen You, Zhikun Peng, Lei Wang, Jing-Li Luo, and Xian-Zhu Fu. “Bifunctional Pt–Co_3O_4 Electrocatalysts for Simultaneous Generation of Hydrogen and Formate via Energy-Saving Alkaline Seawater/Methanol Co-Electrolysis.” Journal of Materials Chemistry A 9, no. 10 (2021): 6316–24. https://doi.org/10.1039/d0ta10501e.

[9] Li, Luyao, Haiqing Liu, Chao Qin, Zhixiu Liang, Alexis Scida, Shiyu Yue, Xiao Tong, Radoslav R. Adzic, and Stanislaus S. Wong. “Ultrathin Pt_xSn_{1-x} Nanowires for Methanol and Ethanol Oxidation Reactions: Tuning Performance by Varying Chemical Composition.” ACS Applied Nano Materials 1, no. 3 (2018): 1104–15. https://doi.org/10.1021/acsanm.7b00289.

[10] Abokifa, Ahmed A., Kelsey Haddad, John Fortner, Cynthia S. Lo, and Pratim Biswas. “Sensing Mechanism of Ethanol and Acetone at Room Temperature by SnO_2 Nano-Columns Synthesized by Aerosol Routes: Theoretical Calculations Compared to Experimental Results.” Journal of Materials Chemistry A 6, no. 5 (2018): 2053–66. https://doi.org/10.1039/c7ta09535j.

[11] Al-Hashem, Mohamad, Sheikh Akbar, and Patricia Morris. “Role of Oxygen Vacancies in Nanostructured Metal-Oxide Gas Sensors: A Review.” Sensors and

Actuators B: Chemical 301 (2019): 126845. https://doi.org/10.1016/j.snb.2019.126845.

[12] Guan, Yanan, Yangtao Zhou, Chunhai Jiang, Xingxiang Xu, Zhenming Yang, Jinsong Zhang, Xiaolei Fan, and Yilai Jiao. "Catalytic Combustion of Volatile Organic Compounds (Vocs) over Structured Co_3O_4 Nano-Flowers on Silicalite-1/Sic Foam Catalysts." Microporous and Mesoporous Materials 323 (2021): 111173. https://doi.org/10.1016/j.micromeso.2021.111173.

[13] Choe, Yong-Sahm. "New Gas Sensing Mechanism for SnO_2 Thin-Film Gas Sensors Fabricated by Using Dual Ion Beam Sputtering." Sensors and Actuators B: Chemical 77, no. 1-2 (2001): 200–208. https://doi.org/10.1016/s0925-4005(01)00731-6.

[14] Luo, Yifan, Ahmadou Ly, Driss Lahem, Justin D.M. Martin, Anne-Claude Romain, Chao Zhang, and Marc Debliquy. "Role of Cobalt in Co-Zno Nanoflower Gas Sensors for the Detection of Low Concentration of Vocs." Sensors and Actuators B: Chemical 360 (2022): 131674. https://doi.org/10.1016/j.snb.2022.131674.

[15] Saruhan, Bilge, Roussin Lontio Fomekong, and Svitlana Nahirniak. "Review: Influences of Semiconductor Metal Oxide Properties on Gas Sensing Characteristics." Frontiers in Sensors 2 (2021). https://doi.org/10.3389/fsens.2021.657931.

[16] Li, Yi-Xiang, Zheng Guo, Yao Su, Xiao-Bo Jin, Xiang-Hu Tang, Jia-Rui Huang, Xing-Jiu Huang, Min-Qiang Li, and Jin-Huai Liu. "Hierarchical Morphology-Dependent Gas-Sensing Performances of Three-Dimensional SnO_2 Nanostructures." ACS Sensors 2, no. 1 (2016): 102–10. https://doi.org/10.1021/acssensors.6b00597.

[17] Park, Sunghoon, Soohyun Kim, Hyejoon Kheel, and Chongmu Lee. "Oxidizing Gas Sensing Properties of the N-Zno/P-CO_3O_4 Composite Nanoparticle Network Sensor." Sensors and Actuators B: Chemical 222 (2016): 1193–1200. https://doi.org/10.1016/j.snb.2015.08.006.

[18] Li, Wenhui, Xiaofeng Wu, Ning Han, Jiayuan Chen, Wenxiang Tang, and Yunfa Chen. "Core-Shell Au@Zno Nanoparticles Derived from Au@Mof and Their Sub-Ppm Level Acetone Gas-Sensing Performance." Powder Technology 304 (2016): 241–47. https://doi.org/10.1016/j.powtec.2016.08.028.

[19] Min, Sung-Ki, Hongseok Kim, Yonghyun Noh, Kyo-Sang Choi, and Sung-Pil Chang. "Fabrication of Highly Sensitive and Selective Acetone Sensor Using (p)- Co_3O_4 Nanoparticle-Decorated (n)-Zno Nanowires." Thin Solid Films 714 (2020): 138249. https://doi.org/10.1016/j.tsf.2020.138249.

[20] Na, Chan Woong, Hyung-Sik Woo, Il-Doo Kim, and Jong-Heun Lee. "Selective Detection of NO_2 and C_2H_5OHHUsing a CO_3O_4-Decorated Zno Nanowire Network Sensor." Chemical Communications 47, no. 18 (2011): 5148. https://doi.org/10.1039/c0cc05256f.

[21] Punginsang, Matawee, Dario Zappa, Elisabetta Comini, Anurat Wisitsoraat, Giorgio Sberveglieri, Andrea Ponzoni, and Chaikarn Liewhiran. "Selective H_2S Gas Sensors Based on Ohmic Hetero-Interface of Au-Functionalized WO_3 Nanowires." Applied Surface Science 571 (2022): 151262. https://doi.org/10.1016/j.apsusc.2021.151262.

[22] Li, Kun, Xiaofang Li, Xiao Chang, Xurong Qiao, Ya Xiong, Fujun Xia, and Qingzhong Xue. "Metal-Organic Frameworks Derived Hierarchical Flower-like Zno/ Co_3O_4 Heterojunctions for Ppb-Level Acetone Detection." Sensors and Actuators B: Chemical 325 (2020): 128814. https://doi.org/10.1016/j.snb.2020.128814.

[23] Chu, Xiangfeng, Shiming Liang, Wenqi Sun, Wangbing Zhang, Tongyun Chen, and Qianfeng Zhang. "Trimethylamine Sensing Properties of Sensors Based on moo3 Microrods." Sensors and Actuators B: Chemical 148, no. 2 (2010): 399–403. https://doi.org/10.1016/j.snb.2010.05.049.

[24] Geng, Wangchang, Shaobing Ge, Xiaowei He, Shan Zhang, Junwei Gu, Xiaoyong Lai, Hong Wang, and Qiuyu Zhang. “Volatile Organic Compound Gas-Sensing Properties of Bimodal Porous α-Fe_2O_3 with Ultrahigh Sensitivity and Fast Response.” ACS Applied Materials & Interfaces 10, no. 16 (2018): 13702–11. https://doi.org/10.1021/acsami.8b02435.

[25] Liu, Yuanjun, Guoxing Zhu, Junzhi Chen, Huan Xu, Xiaoping Shen, and Aihua Yuan. “Co_3O_4/Zno Nanocomposites for Gas-Sensing Applications.” Applied Surface Science 265 (2013): 379–84. https://doi.org/10.1016/j.apsusc.2012.11.016.

[26] Zhang, Haiming, Cheng Xu, Peike Sheng, Yuejiao Chen, Ling Yu, and Qiuhong Li. “Synthesis of Zno Hollow Spheres through a Bacterial Template Method and Their Gas Sensing Properties.” Sensors and Actuators B: Chemical 181 (2013): 99–103. https://doi.org/10.1016/j.snb.2013.01.002.

[27] Nath, S.S., M. Choudhury, D. Chakdar, G. Gope, and R.K. Nath. “Acetone Sensing Property of Zno Quantum Dots Embedded on PVP.” Sensors and Actuators B: Chemical 148, no. 2 (2010): 353–57. https://doi.org/10.1016/j.snb.2010.06.001.

[28] Xiao, Junwu, Qin Kuang, Shihe Yang, Fei Xiao, Shuai Wang, and Lin Guo. “Surface Structure Dependent Electrocatalytic Activity of Co_3O_4 Anchored on Graphene Sheets toward Oxygen Reduction Reaction.” Scientific Reports 3, no. 1 (2013). https://doi.org/10.1038/srep02300.

[29] Lin, Yanli, Huiming Ji, Zhurui Shen, Qianqian Jia, and Dahao Wang. “Enhanced Acetone Sensing Properties of Co_3O_4 Nanosheets with Highly Exposed (111) Planes.” Journal of Materials Science: Materials in Electronics 27, no. 2 (2015): 2086–95. https://doi.org/10.1007/s10854-015-3995-y.

[30] Monter-Guzmán, Jessica Yazmín, Xiangfeng Chu, Elisabetta Comini, Mauro Epifani, and Rodolfo Zanella. “How Chemoresistive Sensors Can Learn from Heterogeneous Catalysis. Hints, Issues, and Perspectives.” Chemosensors 9, no. 8 (2021): 193. https://doi.org/10.3390/chemosensors9080193.

[31] Bekermann, D., A. Gasparotto, D. Barreca, C. Maccato, E. Comini, C. Sada, G. Sberveglieri, A. Devi, and R. A. Fischer. “Co_3O_4/Zno Nanocomposites: From Plasma Synthesis to Gas Sensing Applications.” ACS Applied Materials & Interfaces 4, no. 2 (2012): 928–34. https://doi.org/10.1021/am201591w.

[32] Qiao, Xurong, Chao Ma, Xiao Chang, Xiaofang Li, Kun Li, Lei Zhu, Fujun Xia, and Qingzhong Xue. “3D Radial Co_3O_4 Nanorod Cluster Derived from Cobalt-Based Layered Hydroxide Metal Salt for Enhanced Trace Acetone Detection.” Sensors and Actuators B: Chemical 327 (2021): 128926. https://doi.org/10.1016/j.snb.2020.128926.

[33] Choi, Pil Gyu, Teruaki Fuchigami, Ken-ichi Kakimoto, and Yoshitake Masuda. “Effect of Crystal Defect on Gas Sensing Properties of Co_3O_4 Nanoparticles.” ACS Sensors 5, no. 6 (2020): 1665–73. https://doi.org/10.1021/acssensors.0c00290.

[34] Zhu, Lian Feng, Jun Cong She, Jian Yi Luo, Shao Zhi Deng, Jun Chen, Xue Wen Ji, and Ning Sheng Xu. “Self-Heated Hydrogen Gas Sensors Based on PT-Coated W18O49 Nanowire Networks with High Sensitivity, Good Selectivity and Low Power Consumption.” Sensors and Actuators B: Chemical 153, no. 2 (2011): 354–60. https://doi.org/10.1016/j.snb.2010.10.047.

[35] Kim, Jae-Hun, Jae-Hyoung Lee, Yujung Park, Jin-Young Kim, Ali Mirzaei, Hyoun Woo Kim, and Sang Sub Kim. “Toluene- and Benzene-Selective Gas Sensors Based on PT- and Pd-Functionalized Zno Nanowires in Self-Heating Mode.” Sensors and Actuators B: Chemical 294 (2019): 78–88. https://doi.org/10.1016/j.snb.2019.05.032.

[36] Das, Sagnik, Subhajit Mojumder, Debdulal Saha, and Mrinal Pal. “Influence of Major Parameters on the Sensing Mechanism of Semiconductor Metal Oxide Based

Chemiresistive Gas Sensors: A Review Focused on Personalized Healthcare." Sensors and Actuators B: Chemical 352 (2022): 131066. https://doi.org/10.1016/j.snb.2021.131066.

[37] Ma, Ahyeon, So Yeon Baek, Jong Hyeok Seo, Syed Asad Abbas, Ji-Hwan Kwon, Sang Jung Ahn, and Ki Min Nam. "Photodeposition of Pt Nanoparticles on Co_3O_4 Nanocubes for Detection of Acetone at Part-per-Billion Levels." ACS Applied Nano Materials 4, no. 3 (2021): 2752–59. https://doi.org/10.1021/acsanm.0c03393.

[38] Jiang, Jing, and Liangchao Li. "Synthesis of Sphere-like Co_3O_4 Nanocrystals via a Simple Polyol Route." Materials Letters 61, no. 27 (2007): 4894–96. https://doi.org/10.1016/j.matlet.2007.03.067.

[39] Hadjiev, V G, M N Iliev, and I V Vergilov. "The Raman Spectra of Co_3O_4." Journal of Physics C: Solid State Physics 21, no. 7 (1988). https://doi.org/10.1088/0022-3719/21/7/007.

[40] Casas-Cabanas, M., G. Binotto, D. Larcher, A. Lecup, V. Giordani, and J.-M. Tarascon. "Defect Chemistry and Catalytic Activity of Nanosized Co_3O_4." Chemistry of Materials 21, no. 9 (2009): 1939–47. https://doi.org/10.1021/cm900328g.

[41] Lou, Yang, Jian Ma, Xiaoming Cao, Li Wang, Qiguang Dai, Zhenyang Zhao, Yafeng Cai, et al. "Promoting Effects of In_2O_3 on Co_3O_4 for CO Oxidation: Tuning O2 Activation and Co Adsorption Strength Simultaneously." ACS Catalysis 4, no. 11 (2014): 4143–52. https://doi.org/10.1021/cs501049r.

[42] Yang, Guijin, Daqiang Gao, Zhenhua Shi, Zhaohui Zhang, Jing Zhang, Jinlin Zhang, and Desheng Xue. "Room Temperature Ferromagnetism in Vacuum-Annealed CoO Nanospheres." The Journal of Physical Chemistry C 114, no. 50 (2010): 21989–93. https://doi.org/10.1021/jp106818p.

[43] Dai, Qilin, and Jinke Tang. "The Optical and Magnetic Properties of CoO and Co Nanocrystals Prepared by a Facile Technique." Nanoscale 5, no. 16 (2013): 7512. https://doi.org/10.1039/c3nr01971c.

[44] Chen, Xiaodan, Heleen van Gog, and Marijn A. van Huis. "Transformation of Co_3O_4 Nanoparticles to COO Monitored by in Situ Tem and Predicted Ferromagnetism at the Co_3O_4/CoO Interface from First Principles." Journal of Materials Chemistry C 9, no. 17 (2021): 5662–75. https://doi.org/10.1039/d0tc05727d.

[45] Donarelli, M., R. Milan, F. Rigoni, G. Drera, L. Sangaletti, A. Ponzoni, C. Baratto, G. Sberveglieri, and E. Comini. "Anomalous Gas Sensing Behaviors to Reducing Agents of Hydrothermally Grown α-Fe_2O_3 Nanorods." Sensors and Actuators B: Chemical 273 (2018): 1237–45. https://doi.org/10.1016/j.snb.2018.07.042.

[46] Brabers, V.A.M., and A.D.D. Broemme. "Low-Spin-High-Spin Transition in the Co_3O_4 Spinel." Journal of Magnetism and Magnetic Materials 104-107 (1992): 405–6. https://doi.org/10.1016/0304-8853(92)90853-g.

[47] Hao, Quanyi, Limiao Li, Xiaoming Yin, Shuang Liu, Qiuhong Li, and Taihong Wang. "Anomalous Conductivity-Type Transition Sensing Behaviors of N-Type Porous α-fe2o3 Nanostructures toward H_2S." Materials Science and Engineering: B 176, no. 7 (2011): 600–605. https://doi.org/10.1016/j.mseb.2011.02.002.

[48] Vladimirova, Svetlana, Valeriy Krivetskiy, Marina Rumyantseva, Alexander Gaskov, Natalia Mordvinova, Oleg Lebedev, Mikhail Martyshov, and Pavel Forsh. "Co_3O_4 As P-Type Material for CO Sensing in Humid Air." Sensors 17, no. 10 (2017): 2216. https://doi.org/10.3390/s17102216.

[49] Lin, Hung-Kuan. Catalysis Letters 88, no. 3/4 (2003): 169–74. https://doi.org/10.1023/a:1024013822986.

[50] Fan, Xiangxiang, Yajuan Xu, Chenyan Ma, and Wuming He. "In-Situ Growth of co3o4 Nanoparticles Based on Electrospray for an Acetone Gas Sensor." Journal of

Alloys and Compounds 854 (2021): 157234. https://doi.org/10.1016/j.jallcom.2020.157234.

[51] Cao, Jing, Shuangming Wang, Haiming Zhang, and Tong Zhang. “Constructing One Dimensional co3o4 Hierarchical Nanofibers as Efficient Sensing Materials for Rapid Acetone

[52] Gas Detection.” Journal of Alloys and Compounds 799 (2019): 513–20. https://doi.org/10.1016/j.jallcom.2019.05.356.

[53] Choi, Seon-Jin, Won-Hee Ryu, Sang-Joon Kim, Hee-Jin Cho, and Il-Doo Kim. “Bi-Functional Co-Sensitization of Graphene Oxide Sheets and Ir Nanoparticles on P-Type Co_3O_4 Nanofibers for Selective Acetone Detection.” J. Mater. Chem. B 2, no. 41 (2014): 7160–67. https://doi.org/10.1039/c4tb00767k.

[54] Yoo, Ran, Yunji Park, Hwaebong Jung, Hyun Jun Rim, Sungmee Cho, Hyun-Sook Lee, and Wooyoung Lee. “Acetone-Sensing Properties of Doped Zno Nanoparticles for Breath-Analyzer Applications.” Journal of Alloys and Compounds 803 (2019): 135–44. https://doi.org/10.1016/j.jallcom.2019.06.254.

[55] Koo, Won-Tae, Sunmoon Yu, Seon-Jin Choi, Ji-Soo Jang, Jun Young Cheong, and Il-Doo Kim. “Nanoscale PDO Catalyst Functionalized Co_3O_4 Hollow Nanocages Using MOF Templates for Selective Detection of Acetone Molecules in Exhaled Breath.” ACS Applied Materials & Interfaces 9, no. 9 (2017): 8201–10. https://doi.org/10.1021/acsami.7b01284.

[56] Zhang, Ziyue, Zhen Wen, Zhizhen Ye, and Liping Zhu. “Gas Sensors Based on Ultrathin Porous Co_3O_4 Nanosheets to Detect Acetone at Low Temperature.” RSC Advances 5, no. 74 (2015): 59976–82. https://doi.org/10.1039/c5ra08536e.

[57] Xu, J.M., J. Zhang, B.B. Wang, and F. Liu. “Shape-Regulated Synthesis of Cobalt Oxide and Its Gas-Sensing Property.” Journal of Alloys and Compounds 619 (2015): 361–67. https://doi.org/10.1016/j.jallcom.2014.09.020.

[58] Zhou, Tingting, Tong Zhang, Jianan Deng, Rui Zhang, Zheng Lou, and Lili Wang. “P-Type Co_3O_4 Nanomaterials-Based Gas Sensor: Preparation and Acetone Sensing Performance.” Sensors and Actuators B: Chemical 242 (2017): 369–77. https://doi.org/10.1016/j.snb.2016.11.067.

[59] Wang, Shuangming, Jing Cao, Wen Cui, Longlong Fan, Xifei Li, Dejun Li, and Tong Zhang. “One-Dimensional Porous Co_3O_4 Rectangular Rods for Enhanced Acetone Gas Sensing Properties.” Sensors and Actuators B: Chemical 297 (2019): 126746. https://doi.org/10.1016/j.snb.2019.126746.

[60] Hübner, M., C.E. Simion, A. Tomescu-Stănoiu, S. Pokhrel, N. Bârsan, and U. Weimar. “Influence of Humidity on Co Sensing with p-Type Cuo Thick Film Gas Sensors.” Sensors and Actuators B: Chemical 153, no. 2 (2011): 347–53. https://doi.org/10.1016/j.snb.2010.10.046.

[61] Liu, Huiling, Hailiu He, Liqiang Chen, Qingjiang Pan, and Guo Zhang. “Flower-like Co_3O_4 Sensor with Rich Oxygen Vacancy Defects for Enhancing Room Temperature NOx Sensing Performances.” Journal of Alloys and Compounds 868 (2021): 159180. https://doi.org/10.1016/j.jallcom.2021.159180.

[62] Vetter, S., S. Haffer, T. Wagner, and M. Tiemann. “Nanostructured Co_3O_4 as a CO Gas Sensor: Temperature-Dependent Behavior.” Sensors and Actuators B: Chemical 206 (2015): 133–38. https://doi.org/10.1016/j.snb.2014.09.025.

[63] Degler, David, Udo Weimar, and Nicolae Barsan. “Current Understanding of the Fundamental Mechanisms of Doped and Loaded Semiconducting Metal-Oxide-Based Gas Sensing Materials.” ACS Sensors 4, no. 9 (2019): 2228–49. https://doi.org/10.1021/acssensors.9b00975.

[64] Yao, Junxuan, Hui Shi, Dekui Sun, Huaiqian Lu, Bo Hou, Litao Jia, Yong Xiao, and Debao Li. “Facet-Dependent Activity of Co_3O_4 Catalyst for C_3H_8 Combustion.” ChemCatChem 11, no. 22 (2019): 5570–79. https://doi.org/10.1002/cctc.201901382.

[65] Fujimoto, K. Catalyst Design Based on Spillover Theory. In New Aspects of Spillover Effects in Catalysis for Development of Highly Active Catalysts; Inui, T., Fujimoto, K., Uchijima, T., Masai, M., Eds.; Elsevier Ltd: Kyoto, 1993; pp 9– 16

[66] Ge, Yunli, Kaixuan Fu, Qian Zhao, Na Ji, Chunfeng Song, Degang Ma, and Qingling Liu. “Performance Study of Modified PT Catalysts for the Complete Oxidation of Acetone.” Chemical Engineering Science 206 (2019): 499–506. https://doi.org/10.1016/j.ces.2019.05.051.

[67] Varghese, B., C. H. Teo, Y. Zhu, M. V. Reddy, B. V. R. Chowdari, A. T. S. Wee, V. B. C. Tan, C. T. Lim, and C.-H. Sow. “Co_3O_4 Nanostructures with Different Morphologies and Their Field-Emission Properties.” Advanced Functional Materials 17, no. 12 (2007): 1932–39. https://doi.org/10.1002/adfm.200700038.

[68] Hanh, Nguyen Hong, Lai Van Duy, Chu Manh Hung, Chu Thi Xuan, Nguyen Van Duy, and Nguyen Duc Hoa. “High-Performance Acetone Gas Sensor Based on Pt–Zn_2SnO_4 Hollow Octahedra for Diabetic Diagnosis.” Journal of Alloys and Compounds 886 (2021): 161284. https://doi.org/10.1016/j.jallcom.2021.161284.

[69] Li, Yuan, Kassandra Keith, and Nitin Chopra. “Structural and Morphological Evolution of Free-Standing Co_3O_4 Nanowires via Water Vapor-Assisted Thermal Oxidation of CO Foil.” Journal of Alloys and Compounds 703 (2017): 414–23. https://doi.org/10.1016/j.jallcom.2017.02.004.

[70] Santos, Renata V., Gabriel A. Cabrera-Pasca, Cleidilane S. Costa, Brianna Bosch-Santos, Larissa Otubo, Luciano F. Pereira, Bruno S. Correa, et al. “Crystalline and Magnetic Properties of CoO Nanoparticles Locally Investigated by Using Radioactive Indium Tracer.” Scientific Reports 11, no. 1 (2021). https://doi.org/10.1038/s41598-021-99810-y.

[71] Seidov, Z., M. Açıkgöz, S. Kazan, and F. Mikailzade. “Magnetic Properties of Co_3O_4 Polycrystal Powder.” Ceramics International 42, no. 11 (2016): 12928–31. https://doi.org/10.1016/j.ceramint.2016.05.063.

[72] Takita, Y. “The Effects of Water Coadsorption on the Adsorption of Oxygen over Metal Oxides I. Temperature-Programmed Desorption Study of Co_3O_4.” Journal of Catalysis 97, no. 1 (1986): 25–35. https://doi.org/10.1016/0021-9517(86)90033-3.

[73] Prakash, Chandra, Rajneesh Chaurasiya, Abhijeet J. Kale, and Ambesh Dixit. “Low-Temperature Highly Robust Hydrogen Sensor Using Pristine Zno Nanorods with Enhanced Response and Selectivity.” ACS Omega 7, no. 32 (2022): 28206–16. https://doi.org/10.1021/acsomega.2c02510.

[74] Nakate, Umesh T., Rafiq Ahmad, Pramila Patil, Y.T. Yu, and Yoon-Bong Hahn. “Ultra Thin NiO Nanosheets for High Performance Hydrogen Gas Sensor Device.” Applied Surface Science 506 (2020): 144971. https://doi.org/10.1016/j.apsusc.2019.144971.

[75] Lee, Jae-Hyoung, Jin-Young Kim, Jae-Hun Kim, and Sang Kim. “Enhanced Hydrogen Detection in Ppb-Level by Electrospun sno2-Loaded Zno Nanofibers.” Sensors 19, no. 3 (2019): 726. https://doi.org/10.3390/s19030726.

[76] Yang, Shulin, Gui Lei, Zhigao Lan, Wei Xie, Baoping Yang, Huoxi Xu, Zhao Wang, and Haoshuang Gu. “Enhancement of the Room-Temperature Hydrogen Sensing Performance of MoO_3 Nanoribbons Annealed in a Reducing Gas.” International Journal of Hydrogen Energy 44, no. 14 (2019): 7725–33. https://doi.org/10.1016/j.ijhydene.2019.01.205.

[77] Kumar, Manjeet, Vishwa Bhatt, Akshay Kumar, and Ju-Hyung Yun. “Nano Lily-Buds Garden like Zno Nanostructures Based Gas Sensor for H_2 Detection.” Materials Letters 240 (2019): 13–16. https://doi.org/10.1016/j.matlet.2018.12.113.

[78] Min, Sung-Ki, Hongseok Kim, Yunsu Kim, and Sung-Pil Chang. “Aupt Bimetal-Codecorated Zno Nanowire-Based Hydrogen Sensors for Detecting Low Concentration Hydrogen Gas with High Response and Selectivity.” Bulletin of the Korean Chemical Society 43, no. 8 (2022): 1057–68. https://doi.org/10.1002/bkcs.12581.

[79] Shrisha, Chang-Mou Wu, Kebena Gebeyehu Motora, Guan-Ying Chen, Dong-Hau Kuo, and Noto Susanto Gultom. “Highly Efficient Reduced Tungsten Oxide-Based Hydrogen Gas Sensor at Room Temperature.” Materials Science and Engineering: B 289 (2023): 116285. https://doi.org/10.1016/j.mseb.2023.116285.

[80] Prakash, Chandra, and Ambesh Dixit. “Catalyst Free Rutile Phase TiO_2 Nanorods as Efficient Hydrogen Sensor with Enhanced Sensitivity and Selectivity.” Current Applied Physics 41 (2022): 183–90. https://doi.org/10.1016/j.cap.2022.07.007.

[81] Koga, Kenji. “Electronic and Catalytic Effects of Single-Atom PD Additives on the Hydrogen Sensing Properties of Co_3O_4 Nanoparticle Films.” ACS Applied Materials & Interfaces 12, no. 18 (2020): 20806–23. https://doi.org/10.1021/acsami.9b23290.

[82] Kumarage, Gayan W.C., and Elisabetta Comini. “Conductometric Gas Sensors.” Reference Module in Materials Science and Materials Engineering, 2023. https://doi.org/10.1016/b978-0-12-819728-8.00060-7.

[83] Jeon, Jun-Young, Sang-Joon Park, and Tae-Jun Ha. “Functionalization of Zinc Oxide Nanoflowers with Palladium Nanoparticles via Microwave Absorption for Room Temperature-Operating Hydrogen Gas Sensors in the PPB Level.” ACS Applied Materials & Interfaces 13, no. 21 (2021): 25082–91. https://doi.org/10.1021/acsami.1c03283.

[84] Hu, Kelin, Feipeng Wang, Zijia Shen, Yuyang Yan, and Hongcheng Liu. “Enhancement Methods of Hydrogen Sensing for One-Dimensional Nanomaterials: A Review.” International Journal of Hydrogen Energy 46, no. 38 (2021): 20119–38. https://doi.org/10.1016/j.ijhydene.2021.03.117.

[85] Li, Meng-Jung, Zuo-Yun Chi, and Yu-Chun Wu. “Morphology, Chemical Composition and Phase Transformation of Hydrothermal Derived Sodium Titanate.” Journal of the American Ceramic Society 95, no. 10 (2012): 3297–3304. https://doi.org/10.1111/j.1551-2916.2012.05330.x.

[86] Tian, Xu, Xiuxiu Cui, Tingrun Lai, Jie Ren, Zhichao Yang, Mingjing Xiao, Bingsen Wang, Xuechun Xiao, and Yude Wang. “Gas Sensors Based on TIO2 Nanostructured Materials for the Detection of Hazardous Gases: A Review.” Nano Materials Science 3, no. 4 (2021): 390–403. https://doi.org/10.1016/j.nanoms.2021.05.011.

[87] Choi, Kyoung Jin, and Ho Won Jang. “One-Dimensional Oxide Nanostructures as Gas-Sensing Materials: Review and Issues.” Sensors 10, no. 4 (2010): 4083–99. https://doi.org/10.3390/s100404083.

[88] Prathan, Aschariya, Jongrak Sanglao, Tao Wang, Chawalit Bhoomanee, Pipat Ruankham, Atcharawon Gardchareon, and Duangmanee Wongratanaphisan. “Controlled Structure and Growth Mechanism behind Hydrothermal Growth of TiO_2 Nanorods.” Scientific Reports 10, no. 1 (2020). https://doi.org/10.1038/s41598-020-64510-6.

[89] Galstyan, Vardan, Elisabetta Comini, Guido Faglia, Alberto Vomiero, Laura Borgese, Elza Bontempi, and Giorgio Sberveglieri. “Fabrication and Investigation of Gas Sensing Properties of Nb-Doped TiO_2Nanotubular Arrays.” Nanotechnology 23, no. 23 (2012): 235706. https://doi.org/10.1088/0957-4484/23/23/235706.

[90] Walker, Janine, Priyanka Karnati, Sheikh A. Akbar, and Patricia A. Morris. “Selectivity Mechanisms in Resistive-Type Metal Oxide Heterostructural Gas Sensors.” Sensors and Actuators B: Chemical 355 (2022): 131242. https://doi.org/10.1016/j.snb.2021.131242.

[91] Rajendran, Suriyaprabha, Gajendra Kumar Inwati, Virendra Kumar Yadav, Nisha Choudhary, Mitesh B. Solanki, Magda H. Abdellattif, Krishna Kumar Yadav, Neha Gupta, Saiful Islam, and Byong-Hun Jeon. “Enriched Catalytic Activity of TiO_2 Nanoparticles Supported by Activated Carbon for Noxious Pollutant Elimination.” Nanomaterials 11, no. 11 (2021): 2808. https://doi.org/10.3390/nano11112808.

[92] Lee, Jinho, Youngmo Jung, Seung-Hyun Sung, Gilho Lee, Jungmo Kim, Jin Seong, Young-Seok Shim, Seong Chan Jun, and Seokwoo Jeon. “High-Performance Gas Sensor Array for Indoor Air Quality Monitoring: The Role of Au Nanoparticles on WO_3, SnO_2, and NIO-Based Gas Sensors.” Journal of Materials Chemistry A 9, no. 2 (2021): 1159–67. https://doi.org/10.1039/d0ta08743b.

[93] Amiri, Vahid, Hossein Roshan, Ali Mirzaei, Giovanni Neri, and Ahmad I. Ayesh. “Nanostructured Metal Oxide-Based Acetone Gas Sensors: A Review.” Sensors 20, no. 11 (2020): 3096. https://doi.org/10.3390/s20113096.

[94] Navale, S.T., Z.B. Yang, Chenshitao Liu, P.J. Cao, V.B. Patil, N.S. Ramgir, R.S. Mane, and F.J. Stadler. “Enhanced Acetone Sensing Properties of Titanium Dioxide Nanoparticles with a Sub-Ppm Detection Limit.” Sensors and Actuators B: Chemical 255 (2018): 1701–10. https://doi.org/10.1016/j.snb.2017.08.186.

[95] Wang, Zhe, Azhar Ali Haidry, Lijuan Xie, Ali Zavabeti, Zhong Li, Wenqiang Yin, Roussin Lontio Fomekong, and Bilge Saruhan. “Acetone Sensing Applications of AG Modified TiO_2 Porous Nanoparticles Synthesized via Facile Hydrothermal Method.” Applied Surface Science 533 (2020): 147383. https://doi.org/10.1016/j.apsusc.2020.147383.

[96] Rella, R., J. Spadavecchia, M.G. Manera, S. Capone, A. Taurino, M. Martino, A.P. Caricato, and T. Tunno. “Acetone and Ethanol Solid-State Gas Sensors Based on Tio2 Nanoparticles Thin Film Deposited by Matrix Assisted Pulsed Laser Evaporation.” Sensors and Actuators B: Chemical 127, no. 2 (2007): 426–31. https://doi.org/10.1016/j.snb.2007.04.048.

[97] Chen, Nan, Yuxiu Li, Dongyang Deng, Xu Liu, Xinxin Xing, Xuechun Xiao, and Yude Wang. “Acetone Sensing Performances Based on Nanoporous TiO_2 Synthesized by a Facile Hydrothermal Method.” Sensors and Actuators B: Chemical 238 (2017): 491–500. https://doi.org/10.1016/j.snb.2016.07.094.

[98] Zhu, Hao, Azhar Ali Haidry, Zhe Wang, and Yinwen Ji. “Improved Acetone Sensing Characteristics of TiO_2 Nanobelts with Ag Modification.” Journal of Alloys and Compounds 887 (2021): 161312. https://doi.org/10.1016/j.jallcom.2021.161312.

[99] Zhou, Xinyuan, Anqi Wang, Ying Wang, Luozhen Bian, Zaixing Yang, Yuzhi Bian, Yan Gong, Xiaofeng Wu, Ning Han, and Yunfa Chen. “Crystal-Defect-Dependent Gas-Sensing Mechanism of the Single ZnO Nanowire Sensors.” ACS Sensors 3, no. 11 (2018): 2385–93. https://doi.org/10.1021/acssensors.8b00792.

[100] Sugimoto, Wataru, Osamu Terabayashi, Yasushi Murakami, and Yoshio Takasu. “Electrophoretic Deposition of Negatively Charged Tetratitanate Nanosheets and Transformation into Preferentially Oriented TiO_2 (B) Film.” Journal of Materials Chemistry 12, no. 12 (2002): 3814–18. https://doi.org/10.1039/b204185e.

[101] Chan, Xiaojun, Tiancheng Pu, Xianyin Chen, Alwin James, Jaeha Lee, John B. Parise, Do Heui Kim, and Taejin Kim. “Effect of Niobium Oxide Phase on the Furfuryl Alcohol Dehydration.” Catalysis Communications 97 (2017): 65–69. https://doi.org/10.1016/j.catcom.2017.04.019.

[102] Huang, Bill X., Kang Wang, Jeffrey S. Church, and Ying-Sing Li. “Characterization of Oxides on Niobium by Raman and Infrared Spectroscopy.” Electrochimica Acta 44, no. 15 (1999): 2571–77. https://doi.org/10.1016/s0013-4686(98)00385-5.

[103] Kong, Lingping, Chuanfang Zhang, Jitong Wang, Wenming Qiao, Licheng Ling, and Donghui Long. “Nanoarchitectured Nb_2O_5 Hollow, nb2o5@Carbon and NbO2@Carbon Core-Shell Microspheres for Ultrahigh-Rate Intercalation Pseudocapacitors.” Scientific Reports 6, no. 1 (2016). https://doi.org/10.1038/srep21177.

[104] Sun, Hongtao, Lin Mei, Junfei Liang, Zipeng Zhao, Chain Lee, Huilong Fei, Mengning Ding, et al. “Three-Dimensional Holey-Graphene/NIOBIA Composite Architectures for Ultrahigh-Rate Energy Storage.” Science 356, no. 6338 (2017): 599–604. https://doi.org/10.1126/science.aam5852.

[105] Guo, Jing, Jun Zhang, Haibo Gong, Dianxing Ju, and Bingqiang Cao. “Au Nanoparticle-Functionalized 3D SnO_2 Microstructures for High Performance Gas Sensor.” Sensors and Actuators B: Chemical 226 (2016): 266–72. https://doi.org/10.1016/j.snb.2015.11.140.

[106] Hongsith, N., C. Viriyaworasakul, P. Mangkorntong, N. Mangkorntong, and S. Choopun. “Ethanol Sensor Based on Zno and Au-Doped Zno Nanowires.” Ceramics International 34, no. 4 (2008): 823–26. https://doi.org/10.1016/j.ceramint.2007.09.099.

[107] Kaur, Navpreet, Dario Zappa, Matteo Ferroni, Nicola Poli, Marco Campanini, Raluca Negrea, and Elisabetta Comini. “Branch-like NiO/ZnO Heterostructures for VOC Sensing.” Sensors and Actuators B: Chemical 262 (2018): 477–85. https://doi.org/10.1016/j.snb.2018.02.042.

[108] Li, Gang, Xin Zhang, Huan Lu, Chao Yan, Kaixin Chen, Hongbing Lu, Jianzhi Gao, et al. “Ethanol Sensing Properties and Reduced Sensor Resistance Using Porous Nb_2O_5- TiO_2 n-n Junction Nanofibers.” Sensors and Actuators B: Chemical 283 (2019): 602–12. https://doi.org/10.1016/j.snb.2018.12.074.

[109] Kang, Yanfei, Liwei Wang, Yanshuang Wang, Hongxin Zhang, Yao Wang, Danting Hong, Yaqing Qv, and Shurong Wang. “Construction and Enhanced Gas Sensing Performances of Cuo-Modified α-Fe_2O_3 Hybrid Hollow Spheres.” Sensors and Actuators B: Chemical 177 (2013): 570–76. https://doi.org/10.1016/j.snb.2012.11.048.

[110] Liu, Chang, Hongbing Lu, Jinniu Zhang, Zhibo Yang, Gangqiang Zhu, Feng Yin, Jianzhi Gao, Chujun Chen, and Xia Xin. “Abnormal P-Type Sensing Response of TiO_2 Nanosheets with Exposed {001} Facets.” Journal of Alloys and Compounds 705 (2017): 112–17. https://doi.org/10.1016/j.jallcom.2017.02.118.

[111] Liao, Jianjun, Fan Yang, Cai-Zhuang Wang, and Shiwei Lin. “The Crystal Facet-Dependent Electrochemical Performance of TiO_2 Nanocrystals for Heavy Metal Detection: Theoretical Prediction and Experimental Proof.” Sensors and Actuators B: Chemical 271 (2018): 195–202. https://doi.org/10.1016/j.snb.2018.05.067.

CHAPTER 5

Conclusions

The thesis discusses the preparation and characterization of various MOXs including Co_3O_4/ZnO composite nanowires, Pt-functionalized Co_3O_4 nanowalls, Co_3O_4 nanowires, TiO_2 nanobelts, and Nb_2O_5 microcolumns, and thoroughly examine their gas sensing properties.

A new Co_3O_4/ZnO composite nanowire design was created using thermal evaporation and thermal oxidation. The nanowires feature a Pt tip, Co_3O_4 layer, and Co_3O_4/ZnO base with Co_3O_4 root, resulting from Co_3O_4 diffusion into ZnO. The nanowires display n-type semiconducting behavior with high sensitivity to reducing gases and air. The sensors made from these nanowires show a high response of 5530 to acetone (50 ppm at 40% humidity) at 250 °C. They exhibit good repeatability and stability, with potential to detect acetone at sub-ppb levels, making them suitable for breath analysis. The design improves metal oxide sensor selectivity with potential applications in catalysis, energy harvesting, and spintronics.

A low-cost green synthesis method was developed to produce Co_3O_4 nano petals with large nanowalls in a spinal structure. Conductometric measurements showed n-type behavior at temperatures above 350 °C, due to interior oxygen diffusion to the surface. Pt functionalization (Pt-Co_3O_4) improved gas sensing performance compared to pristine Co_3O_4, thanks to spillover enhancement and inverse spillover of oxygen and analyte gas. The Pt-Co_3O_4 sensors showed a higher response of 25.2 to 10 ppm acetone at 500 °C in dry air and maintained performance under high humidity, making them a potential candidate for wearable acetone sensors and biomarker sensing with the low-cost green synthesis method.

Also, the study focuses on synthesizing and evaluating the gas sensing properties of Co_3O_4 nanowires and nanowalls. The nanowires were produced using a 50 nm cobalt layer through thermal oxidation (300 °C, 3h, 2.2 mbar, 100 sccm Ar), resulting in a higher density. TEM images showed nanowires with diameters of 6-50 nm and lengths of 1-5 μm, while HR-TEM showed preferential growth of (311). Raman spectroscopy revealed typical Co_3O_4 phonon modes, and EPR showed ferromagnetic behavior before aging but changing to antiferromagnetic/paramagnetic after aging at 400 °C. Gas sensing tests revealed an excellent response to hydrogen with higher nanowire density and an unusual signal reversal above 300 °C due to lattice oxygen involvement. The sensors maintained stable conductance at 90% humidity for 25 days, thanks to catalytic activity of Co^{2+} and higher operating temperature. The sensors demonstrated exceptional selectivity for hydrogen over acetone, ethanol, carbon

monoxide, methane, and nitrogen dioxide, with a response of 2.32 for 100 ppm hydrogen and a detection limit of 360 ppb.

During this research I also employed hydrothermal methods to synthesize successful monoclinic TiO_2 nanobelts. Acetic acid was effective in protonating TiO_2-(B) and produced TiO_2 gas sensors with good performance, such as the highest response of 6.5 to 10 ppm acetone at 150 °C. The sensors showed good selectivity for acetone over ethanol, hydrogen, methane, and nitrogen dioxide, making the monoclinic TiO_2-B nanobelts suitable for low-power gas sensing devices. The low detection limit and high acetone selectivity make them valuable for chemiresistive gas sensor applications.

The growth of Nb_2O_5 microcolumns has been achieved using hydrothermal methods in addition to TiO_2 nanobelts. After being prepared at 180 °C and calcined at 700 °C, the microcolumns formed an orthorhombic crystal structure. The sensors made from these microcolumns showed selectivity in detecting ethanol, with a detection limit of 1.4 ppb at an optimal operating temperature of 500 °C in dry air. The sensors also performed well at 90% humidity, with a 4% degradation in response compared to dry conditions (2.51, 10 ppm) and a 41% drift in baseline conductance. The sensors demonstrated excellent repeatability after three cycles and an unchanged response time at different humidity levels (10, 20,40,60,80 and 90 RH%), but a faster recovery time due to the formation of $C_2H_5OH_2^+.(H_2O)$ with a low ionic diffusion coefficient.

In this PhD activity, various chemical sensors with different materials (Co_3O_4, TiO_2, Nb_2O_5) were prepared, with a special focus on the novel Co_3O_4/ZnO nanowires structures. These fabricated devices exhibited excellent sensing capabilities toward various chemicals.

Additionally, the study aimed to investigate the impact of noble metal functionalization, humidity, and composite materials on the gas sensing properties of the prepared sensors. Long-term stability and repeatability were also evaluated to ensure the practicality of the sensors.

As a result of the promising findings, the study introduced a new flash lamp annealing technique for synthesizing Co_3O_4 nanostructures. The researchers are now working towards fabricating low-cost, flexible, and wearable acetone sensors in collaboration with EMPA in Switzerland.

MODULO DI EMBARGO DELLA TESI
(da compilare solo se si richiede un periodo di segretazione della tesi)

Il/La sottoscritto/a W.G.C. Kumarage Nato/a il 13/08/1985
a (indicare anche l'eventuale paese estero) Galle, Sri Lanka
provincia di (ovvero sigla del paese estero) GALLE
Dottorato di Ricerca in Scienze fisiche per l'ingegneria

DICHIARA

- che il contenuto della tesi **non può essere immediatamente consultabile per il seguente motivo**

La tesi include dati di ricerca non pubblicati, pertanto non dovrebbe essere resa pubblica

La motivazione deve essere dettagliata e controfirmata obbligatoriamente dal Tutor e/o Relatore
(Brevetto, segreto industriale, motivi di priorità nella ricerca, motivi editoriali, altro)

- che il testo completo della tesi potrà essere reso consultabile dopo:

□ 6 mesi dalla data di conseguimento titolo
□ 12 mesi dalla data di conseguimento titolo
☒ 24 mesi dalla data di conseguimento titolo
□ altro periodo _____

- che sarà comunque consultabile immediatamente l'abstract della tesi, che viene caricato in Esse3, profilo studente.

Luogo e Data
26/05/2023

Firma del Dichiarante

Controfirma del Tutor e/o Relatore del Dottorato
per la motivazione di embargo e il periodo.